

# PRIMORDIAL BINARIES AND STAR CLUSTER FORMATION



DYNAMICAL MODIFICATION OF A PRIMORDIAL POPULATION OF  
BINARIES IN SIMULATIONS OF STAR CLUSTER FORMATION

By Claude COURNOYER-CLOUTIER, B.Sc.

*A Thesis Submitted to the School of Graduate Studies  
in the Partial Fulfillment of the Requirements  
for the Degree Master of Science*

McMaster University

© Copyright by Claude COURNOYER-CLOUTIER August 31, 2021

McMaster University

Master of Science (2021)

Hamilton, Ontario (Physics & Astronomy)

TITLE: Dynamical Modification of a Primordial Population of Binaries in Simulations  
of Star Cluster Formation

AUTHOR: Claude COURNOYER-CLOUTIER , B.Sc. (McMaster University)

SUPERVISORS: Dr. Alison SILLS & Dr. William E. HARRIS

NUMBER OF PAGES: xxiii, 116

# Abstract

Most star formation in galaxies takes place in embedded clusters, within Giant Molecular Clouds (GMCs). Stars also generally form as part of binary star systems, with almost all massive stars having at least one close companion. Binaries shape the physical properties of older star clusters by setting their central density and ejecting low-mass stars, but also play a role during cluster formation by modifying the mechanical and radiative feedback from massive stars and shedding enriched material in the cluster’s gas reservoir. Conversely, dynamical interactions between stars in dense stellar environments are known to form, modify, and destroy binary systems. In consequence, the populations of binaries observed in the Galactic field and in old stellar clusters are understood to be shaped by a combination of the physics of star formation and subsequent dynamical interactions in embedded clusters, although the relative importance of these processes remains unknown. In this thesis, we implement a prescription for an initial population of binaries in the coupled N-body and radiation hydrodynamics star cluster formation code TORCH, and investigate how this initial population is modified in the earliest stages of cluster formation, while gas and stars coexist. As an ansatz for the initial population of binaries, we use the properties of main-sequence binaries in the Galactic field. We first perform a suite of simulations initialized from a  $10^4 M_{\odot}$  cloud, in which the simulations only differ by their stellar content (i.e. presence or absence of an initial population of binaries, and stochasticity of star formation). We compare the populations of binaries identified 1.2–2 Myr after the onset of star formation and find that an initial population of binaries is needed at all masses to reproduce the multiplicity fraction observed in main-sequence stars. We also show that this initial population is modified in a systematic manner before the effects of feedback from massive stars shape the gas. We further find evidence of both preferential formation and preferential destruction of binaries via dynamical interactions. The net effect of these interactions shifts the distributions of primary masses and semi-major axes to lower values, and the distributions of mass ratios

and eccentricities to larger values. In a second time, we perform simulations with different virial parameters and initial turbulent velocity patterns, and find that the trends previously identified are robust to those changes in our initial conditions. We however find that both the virial parameter and the initial turbulent velocity pattern have a strong influence on the star formation rate, and therefore on the rapidity with which the distributions are modified. We conclude that dynamical interactions in embedded clusters are important for shaping the populations of binaries observed in the Milky Way, thus opening the floor to future investigations of the impact of binaries on star cluster formation.

# Declaration of Authorship

I, Claude COURNOYER-CLOUTIER, declare that this thesis titled, “Dynamical Modification of a Primordial Population of Binaries in Simulations of Star Cluster Formation” and the work presented in it are my own. Chapters 1 and 2 are an overview of the current state of the field. Chapters 3 and 4 are original work written by myself. Chapter 3 is a published article which appeared in the peer-reviewed journal Monthly Notices of the Royal Astronomical Society (MNRAS), with the following reference:

*Cournoyer-Cloutier, C., Tran, A., Lewis, S., Wall, J. E., Harris, W. E., Mac Low, M-M., McMillan, S. L. W., Portegies Zwart, S., Sills, A. 2021, MNRAS, Volume 501, Issue 3, pp.4464-4478.*

It is reproduced here in full. I conducted the simulations, analyzed the data, prepared the figures and tables, and wrote the text of the paper. The code used for the simulations was originally written by J. E. Wall and refactored by A. Tran; A. Tran and S. Lewis provided valuable technical help in installing the code. The last five authors appear in alphabetical order; my supervisors, Dr. William E. Harris and Dr. Alison Sills, are respectively 5th and 9th authors. Dr. Mac Low, Dr. McMillan and Dr. Portegies Zwart participated in the editing process of the paper. Chapter 4 contains material in preparation for submission to MNRAS. I hereby grant an irrevocable, non-exclusive license to McMaster University and the National Library of Canada to reproduce this material as part of this thesis.



## *Acknowledgements*

First and foremost, I would like to extend my warmest gratitude to my supervisors, Dr. Alison Sills and Dr. Bill Harris, for their unwavering support over the past two years. Your insights and guidance in all aspects of my path as a graduate student are invaluable. I feel incredibly fortunate I have the opportunity to work with you and receive your support. Thank you for sharing your knowledge and experience with me, and encouraging me both in my academic endeavours and in my involvement within the department. Working with you is a real pleasure, and I already look forward to the next few years.

Many thanks are also owed to my collaborators. I am very grateful to Dr. Mordecai-Mark Mac Low and Aaron Tran for many, many useful conversations about hydrodynamics and coding, and precious help with FLASH. I would also like to thank Dr. Steve McMillan and Dr. Simon Portegies Zwart for very relevant discussions about stellar dynamics. You were all very welcoming from the start, and it made a tremendous difference in getting started with my Master's.

I would also like to thank Jeremy, Kate and Veronika for many interesting conversations about star clusters, cats and baking, as well as for being the best coffee break friends. This wouldn't be the same without you. I would like to also extend my thanks to Marta, Sean and Brooke: our regular virtual chats have been (and continue to be) a great support. My warmest thanks also go to Jacqueline, Carmen and Blake, for making me feel at home at McMaster right from the start.

Last but not least, I would like to thank my parents, Claire and Pierre, for their constant support. Thank you for nurturing my curiosity, and having the patience to read me the same astronomy books over and over again as a little girl. Du fond du coeur, merci.



---

---

CONTENTS

<b>Abstract</b>	<b>iii</b>
<b>Declaration of Authorship</b>	<b>v</b>
<b>Acknowledgements</b>	<b>vii</b>
<b>List of Figures</b>	<b>xi</b>
<b>List of Tables</b>	<b>xxi</b>
<b>1 Introduction</b>	<b>1</b>
1.1 Star cluster formation . . . . .	4
1.2 Stellar feedback in embedded clusters . . . . .	8
1.3 Stellar multiplicity in different environments . . . . .	15
1.4 Thesis outline . . . . .	19
<b>2 Numerical Methods for Star Cluster Formation</b>	<b>21</b>
2.1 Numerical hydrodynamics . . . . .	21

2.2	Sink particles . . . . .	25
2.3	Numerical stellar dynamics . . . . .	27
2.4	Early stellar feedback: winds & radiation . . . . .	30
2.5	Multi-physics simulations and their challenges . . . . .	35
<b>3</b>	<b>Implementing Primordial Binaries in Simulations of Star Cluster For-</b>	
	<b>mation with a Hybrid MHD and Direct N-Body Method</b>	<b>39</b>
3.1	Introduction . . . . .	40
3.2	Methods . . . . .	43
	3.2.1 Simulating cluster formation with Torch . . . . .	43
	3.2.2 Binary generation algorithm . . . . .	45
	3.2.3 Implementing primordial binaries in Torch . . . . .	52
3.3	Simulations . . . . .	56
3.4	Binary properties . . . . .	62
	3.4.1 Binary fractions . . . . .	64
	3.4.2 Final binary properties . . . . .	65
	3.4.3 Modification of primordial binaries . . . . .	71
	3.4.4 Dynamical binary formation . . . . .	73
3.5	Summary and discussion . . . . .	77
	3.5.1 Summary . . . . .	77
	3.5.2 Discussion . . . . .	78
<b>4</b>	<b>Discussion &amp; Future Work</b>	<b>81</b>
4.1	Key results and their implications . . . . .	82
4.2	Current state of our simulations . . . . .	85
4.3	The influence of initial conditions . . . . .	92
4.4	Directions for future work . . . . .	103
	<b>Bibliography</b>	<b>107</b>

---

---

## LIST OF FIGURES

- 1.1 Importance of different feedback mechanisms as a function of cluster mass and size. The horizontal axis is the stellar mass and the vertical axis is the half-mass radius. Observed Galactic and extragalactic clusters are shown as shaded hexagons and data points. The green line denotes protostellar outflows and jets, the black line denotes supernovae, the blue line denotes direct radiation pressure and the red line denotes photoionizing radiation. The feedback mechanisms are effective in the associated shaded regions; the combination of winds (not shown) and photoionization is most effective for escape velocities  $v_{esc} \lesssim 5$  km/s (Dale et al. 2014). *Credit: Krumholz, McKee & Bland-Hawthorn, 2019, ARA&A, 57, 227, Figure 12. Reproduced with permission, ©Annual Review.* . . . . . 10

1.2	Hubble Space Telescope view of the Trapezium cluster, processed by Robert Gendler. The Trapezium cluster lies within the Orion Nebula (M42), a star-forming region with a total mass in gas of at least 10,000 times the mass of the Sun and 3,500 stars. The four bright stars in the middle of the image are massive O-stars that are likely responsible for removing the gas from within the cluster via radiative and momentum feedback. At least two of these massive stars are in binaries. <i>Credit: R. Gendler and NASA/ESA/Hubble.</i> . . . . .	11
2.1	Density slices of the time evolution of the wind bubbles for two $25 M_{\odot}$ stars formed at the same time, 5 kyr (left) and 15 kyr (right) after their formation, with overlaid velocity vectors. The black circles denote the wind injection radii. A shock forms at the interface between the two wind bubbles and the structure is symmetric about the shock front. . . . .	33
2.2	Density slices of the time evolution of the wind bubbles for a $25 M_{\odot}$ and a $70 M_{\odot}$ star formed with a time delay of 10 kyr before the formation of the most massive star, at the time of formation of the most massive star (left) and 10 kyr after (right). Velocity vectors are overlaid and the wind injection radii are denoted by black circles. After its formation, the most massive star dominates the evolution of the system. The presence of the other star results in a non-symmetric structure for the wind bubble. . . .	34
3.1	Mass dependent binary fraction, for main sequence stars in the solar neighbourhood (Moe & Di Stefano 2017; Winters et al. 2019) and for our binary generation algorithm. The errors in $x$ correspond to the bin widths; the errors in $y$ in the observations are from the observational uncertainties while the errors in $y$ on the algorithm data are from the Poisson statistical error. . . . .	52

3.2	Distribution of stellar masses, for the single stars and primaries drawn from the Kroupa initial mass function (red) and the companions obtained from the mass ratio probability distribution (grey). The Kroupa initial mass function normalized to $10,000 M_{\odot}$ (solid line) and to the total stellar mass (dotted line) is provided as a guide for the eye. . . . .	53
3.3	Distribution of mass ratios against primary masses. Our algorithm restricts mass ratios to be higher than 0.1, as observations are highly incomplete below this value. The red line denotes the companion mass corresponding to the hydrogen-burning limit; note that no substellar companions are generated. . . . .	54
3.4	Star formation rates for <b>M4r5b-4</b> (top) and <b>M4r6s</b> (bottom). The solid black line shows the rate smoothed over 1 kyr (left axis) and the blue points shows the masses of the individual stars formed in the simulation (right axis). The total stellar masses are respectively $2.14 \times 10^3 M_{\odot}$ and $7.60 \times 10^2 M_{\odot}$ for <b>M4r5b-4</b> and <b>M4r6s</b> . Peaks in star formation rate coincide with the formation of massive stars, and there is an overall increase of the star formation rate as the simulation progresses. . . . .	59
3.5	Final projected density distribution in the simulations (from top left to bottom right) <b>M4r5b-1</b> , <b>M4r5b-3</b> , <b>M4r5b-4</b> , <b>M4r5s-2</b> , <b>M4r5s-3</b> , <b>M4r5s-4</b> , <b>M4r6b-2</b> , <b>M4r6b-4</b> and <b>M4r6s</b> . The white circles are the full sample of stars in the simulations; the radius of the circle is proportional to the stellar mass. All simulations use the same initial conditions, which is reflected by the very similar gas configurations. We note however differences in the locations and masses of the stars, and expect to see these differences reflected in the gas configuration once feedback becomes more important. The total stellar mass and number of stars for each simulation can be found in Table 3.4. . . . .	60

- 3.6 Binary fraction as a function of primary mass in **M4r5**, for the full binary population (top) and for observable systems (bottom). The primordial binaries formed in **M4r5b**, the binaries present at the end of **M4r5b** and those present at the end of **M4r5s** are denoted respectively by the black, red and blue thin crosses. The primordial and final binary fractions are exactly equal for the highest mass bin in the bottom panel. Observations from main sequence stars in the solar neighbourhood (Moe & Di Stefano 2017; Winters et al. 2019), with mass ratios  $\geq 0.1$ , are provided for comparison as the solid grey crosses. Binaries from the simulations of Wall et al. (2019), which do not include primordial binaries, are denoted by the thick black crosses. All the errors in  $x$  correspond to the bin widths and the errors in  $y$  in the observations are from the observational uncertainties. The  $y$  errors on the simulation data from Wall et al. are  $1/\sqrt{N}$  (see Wall et al. 2019). The  $y$  errors on our simulation data are from the Poisson statistical errors:  $1/\sqrt{N}$  for  $N > 100$  and the tabulated  $1 \sigma$  confidence interval for  $N \leq 100$  (Gehrels 1986; Hughes & Hase 2010). . . . . 63
- 3.7 Cumulative distribution of primary masses in **M4r5**, for the full binary population (top) and observable systems (bottom). The solid black line denotes the primordial primary mass distribution in **M4r5b**, the solid red line denotes the final distribution in **M4r5b** and the solid blue line denotes the final distribution in **M4r5s**. The fainter lines denote the corresponding primary mass distribution in individual simulations. Pure dynamical formation results in systems with higher primary masses, while the dynamical evolution of the cluster with primordial binaries favours lower-mass primaries. . . . . 66

3.8	<p>Cumulative distribution of mass ratios in <b>M4r5</b>, for the full binary population (top) and observable systems (bottom). The solid black line denotes the primordial mass ratio distribution in <b>M4r5b</b>, the solid red line denotes the final distribution in <b>M4r5b</b> and the solid blue line denotes the final distribution in <b>M4r5s</b>. The fainter lines denote the corresponding mass ratio distribution in individual simulations. Dynamical formation in both <b>M4r5b</b> and <b>M4r5s</b> favours systems with smaller mass ratios: up to 50% of the systems formed in <b>M4r5s</b> have mass ratios below the detection limit. . . . .</p>	67
3.9	<p>Cumulative distribution of semi-major axes in <b>M4r5</b>, for the full binary population (top) and observable systems (bottom). The solid black line denotes the primordial semi-major axis distribution in <b>M4r5b</b>, the solid red line denotes the final distribution in <b>M4r5b</b> and the solid blue line denotes the final distribution in <b>M4r5s</b>. The fainter lines denote the corresponding semi-major axis distribution in individual simulations. Pure dynamical formation results in systems with much larger semi-major axes; conversely, dynamical evolution during cluster formation results in smaller semi-major axes. . . . .</p>	68
3.10	<p>Cumulative distribution of eccentricities in <b>M4r5</b>, for the full binary population (top) and observable systems (bottom). The solid black line denotes the primordial eccentricity distribution in <b>M4r5b</b>, the solid red line denotes the final distribution in <b>M4r5b</b> and the solid blue line denotes the final distribution in <b>M4r5s</b>. The fainter lines denote the corresponding eccentricity distribution in individual simulations. Pure dynamical formation results in systems with much larger eccentricities. . . . .</p>	69

- 3.11 Cumulative distributions of semi-major axes (top) and eccentricities (bottom) for the primordial systems in **M4r5b** surviving to the end of our simulations. The solid grey lines represent the initial properties of the surviving systems, while the solid cyan lines represent their final properties. The fainter lines denote the corresponding distributions in individual simulations. Out of the 1274 binary systems we detect in **M4r5b**, 1077 systems are surviving systems. The distribution of the semi-major axes of the surviving systems at the end of the simulations is consistent with their distribution at the time of star formation (96.2% confidence). The final values of eccentricity are systematically larger (83.1% confidence). By definition, the primary masses and mass ratios of these systems are unchanged. . . . . 72
- 3.12 Cumulative distributions of primary masses, mass ratios, semi-major axes and eccentricities for the primordial systems in **M4r5b**. The black solid lines represent all the primordial systems formed in our simulations and the solid cyan lines represent the primordial systems that survive until the end of simulations. The fainter lines denote the corresponding distributions in individual simulations. Out of 1789 primordial systems, 260 were fully destroyed and 66 changed companions; 1463 systems survived to the end of our simulations. The distributions of primary masses, mass ratios and semi-major axes are different for the full primordial population and the subset of surviving systems; it is ambiguous whether the eccentricity distribution changed. . . . . 74

3.13	Cumulative distributions of primary masses, mass ratios, semi-major axes and eccentricities for binary systems formed dynamically in <b>M4r5</b> , and primordial binaries in <b>M4r5b</b> . The solid blue lines represent the 281 systems detected in <b>M4r5s</b> , the solid orange lines represent the 66 systems where the primary changed companions and the 341 systems formed dynamically with new primaries in <b>M4r5b</b> , and the solid black lines represent the primordial binaries in <b>M4r5b</b> . The fainter lines denote the corresponding distributions in individual simulations. The distributions are different for all four parameters; we note that the cumulative distributions for dynamical binaries in <b>M4r5b</b> always lie between the cumulative distributions for primordial binaries and <b>M4r5s</b> . . . . .	75
3.14	Cumulative distributions of primary masses, mass ratios, semi-major axes and eccentricities for surviving, modified and new binary systems in <b>M4r5b</b> . The solid green lines represent the 341 systems formed dynamically with new primaries in <b>M4r5b</b> , the solid magenta and orange lines represent the 66 systems where the primary changed companions respectively when they are formed and at the end of <b>M4r5b</b> , and the solid cyan lines represent the surviving systems in <b>M4r5b</b> . The fainter lines denote the corresponding distributions in individual simulations. The distributions are all different except for the primary mass distribution, which is by definition the same for the modified systems when they are formed and at the end of the simulation. . . . .	76
4.1	Projected gas densities for <b>M4b4</b> (left) and <b>M4s4</b> (right), respectively 3.26 Myr and 3.11 Myr after the beginning of the simulation. The massive $78.8 M_{\odot}$ star in <b>M4s4</b> , formed 0.2 Myr ago, has blown away a cavity from its wind and radiation (see middle right panel). . . . .	87

4.2	Star formation rate as a function of time after the onset of star formation. A Gaussian filter is applied to smooth the SFR over 50 kyr. The simulations with primordial binaries are shown in black; the simulations without primordial binaries are shown in blue. At equal times, SFRs vary by about half an order of magnitude. . . . .	89
4.3	Cumulative distributions of mass ratios (top left), primary masses (top right), semi-major axes (bottom left) and eccentricities (bottom right) for our fiducial simulations with primordial binaries, 1.6 Myr after the onset of star formation. The thick grey line represents the cumulative distribution for the five simulations, while the colored lines represent the individual simulations. . . . .	90
4.4	Cumulative distributions of mass ratios (top left), primary masses (top right), semi-major axes (bottom left) and eccentricities (bottom right), for M4b4, 2.14 Myr after the onset of star formation. The black lines represent the primordial binaries formed in the simulation and the red lines represent the binaries detected at the current time. All four distributions undergo statistically significant changes. . . . .	91
4.5	Projected gas density for V1-s (left) and V2-b (right). Some elements of the gas structure – e.g.the horizontal trend in the $y$ projection, the inverted Y in the $z$ projection – are similar (also see Figure 4.1 for $\alpha = 0.4$ ) but become more diffuse with increasing $\alpha$ . . . . .	94
4.6	Projected gas density for M4S3 (left) and M3S7 (right). Due to the different random velocity pattern of the initial turbulent spheres, the gas structures in the two simulations are very different, and are also different from the gas structure in the fiducial simulations. Nonetheless, they display similar filamentary structures, within which star formation takes place. . . . .	95

4.7	Star formation rate as a function of time after the onset of star formation, for the three different virial parameters. A Gaussian filter is applied to smooth the SFR over 50 kyr. The simulations with $\alpha = 0.4$ (M4b4 and M4s4 are chosen as examples) are shown in black, those with $\alpha = 1.0$ are show in cyan and those with $\alpha = 2.0$ are shown in magenta; the solid lines denotes the simulations with primordial binaries and the shaded lines the ones without primordial binaries. The SFR is systematically lower in simulations with higher $\alpha$ . . . . .	97
4.8	Cumulative distributions of mass ratios (top left), primary masses (top right), semi-major axes (bottom left) and eccentricities (top right) when the stellar mass in the simulation is $\sim 550 M_{\odot}$ . The solid black lines denote the combined distributions for $\alpha = 0.4$ , the grey lines denote the individual distributions for $\alpha = 0.4$ and the cyan line denotes the distributions for $\alpha = 1.0$ . . . . .	99
4.9	Star formation rate as a function of time since the onset of star formation, for three different sets of turbulent initial conditions. The grey lines are the fiducial simulations, the orange line is M4S3 and the violet line is M4S7. The black line represents a test of the fiducial initial conditions conducted with our most recent refinement criteria, also used for M4S3 and M4S7. . . . .	100
4.10	Cumulative distributions of mass ratios (top left), primary masses (top right), semi-major axes (bottom left) and eccentricities (bottom right) when the stellar mass in the simulation is $\sim 880 M_{\odot}$ . The solid black lines denote the combined distributions with the fiducial initial conditions, the grey lines denote the individual distributions for the fiducial initial conditions, the orange lines denote the distributions for M4S3 and the violet lines denote the distributions for M4S7. . . . .	102



---



---

LIST OF TABLES

3.1 Multiplicity properties from Winters et al. (2019).  $M_1$  is the primary mass,  $\mathcal{F}$  is the binary fraction,  $\mu_a$  is the mean projected separation around which the lognormal probability distribution is centered,  $\mu_P$  (days) is the corresponding period in days (assuming a circular orbit) and  $\log \sigma_P$  is the standard deviation of the lognormal distribution. With the exception of the binary fraction and the period, all the other properties for systems with  $M_1 \leq 0.60 M_\odot$  are obtained from the same distributions as systems with  $M_1 \sim 1 M_\odot$  (see Table 3.2, top row). . . . . 47

3.2 Multiplicity properties from Moe & Di Stefano (2017).  $M_1$  is the primary mass,  $\mathcal{F}$  is the binary fraction,  $P$  is the period range,  $\mathcal{F}_P$  is the relative probability for a system to have a period in a given range;  $\gamma_{\geq 0.3}$  is the power-law exponent of the mass ratio distribution for  $q \geq 0.3$  and  $\gamma_{< 0.3}$  is the power-law exponent of the mass ratio distribution for  $q < 0.3$ . . . . 47

3.3	Spatial and mass resolution, at maximum refinement level <i>ref</i> . $\Delta x$ denotes the minimum zone size while $\Delta m$ and $\rho_c$ denote respectively the maximum mass and the maximum density in a grid cell to trigger sink formation, assuming a sound speed $c_s = 1.9 \times 10^4 \text{ cm s}^{-1}$ (following Federrath et al. 2010) . . . . .	58
3.4	Simulations. All simulations have a total gas mass $10^4 M_\odot$ and a minimum refinement of 4. The number after <b>r</b> denotes the maximum refinement level and the last letter indicates if the simulation includes primordial binaries ( <b>b</b> ) or single stars only ( <b>s</b> ). $t_*$ denotes the time of the onset of star formation and $t$ denotes the time at which the simulation has ended; $M_m$ denotes the mass of the most massive star, $N_*$ is the number of stars in the simulation, and $M_*$ is the total stellar mass. . . . .	61
4.1	Current properties of our simulations. All simulations are initialized from the same turbulent sphere of gas, with $\alpha = 0.4$ , a cloud mass of $9108 M_\odot$ and a free-fall time of 1.57 Myr. The onset of star formation occurs at 1.12 Myr. The simulations labelled with <b>b</b> include primordial binaries; those labelled with <b>s</b> do not. $t$ denotes the time since the beginning of the simulation; $N_*$ denotes the number of stars on the grid; $M_*$ denotes the formed stellar mass; $M_S$ denotes the mass contained in the sinks; $M_g$ denotes the gas mass on the grid; $\epsilon_{ff}$ denotes the SFE per free-fall time (calculated from the formed stellar mass and the initial cloud mass); $M_m$ denotes the mass of the most massive star and $t_m$ the time at which it formed. . . . .	86
4.2	Difference in binary properties, 1.6 Myr after the onset of star formation. The mass ratios $q$ in <b>M4b3</b> are smaller than in the other simulations; the eccentricities $e$ are larger in <b>M4b4</b> than in the other simulations. . . . .	89

4.3	Confidence at which we detect changes in our distributions of binaries, for our five fiducial simulations with primordial binaries. . . . .	92
4.4	Current properties of our simulations with different initial conditions. All simulations except those labelled with <b>s</b> include primordial binaries. The free-fall times and initial cloud mass of M4S3 and M4S7 are within 1% of those for our fiducial simulations. $t$ denotes the time since the beginning of the simulation; $t_{SF}$ denotes the time since the onset of star formation; $N_*$ denotes the number of stars on the grid; $M_*$ denotes the formed stellar mass; $M_S$ denotes the mass contained in the sinks; $M_g$ denotes the gas mass on the grid; $\epsilon_{ff}$ denotes the SFE per free-fall time; $M_m$ denotes the mass of the most massive star and $t_m$ the time at which it formed. Note that no O-star has formed in V1-b. . . . .	93
4.5	Confidence at which we detect changes in our distributions of binaries, for our simulations with primordial binaries and larger virial parameters, at the current time in the simulations. . . . .	98
4.6	Confidence at which we detect changes in our distributions of binaries, for our simulations with primordial binaries and different turbulent initial conditions, at the current time in the simulations. . . . .	100



# CHAPTER 1

## INTRODUCTION

Stars form within turbulent clouds of molecular hydrogen, from the gravitational fragmentation of clumps of cold, dense gas (e.g. Jeans 1928; Hoyle 1953; Larson 1981). This process often occurs in a clustered fashion, with stars forming alongside tens to hundreds of thousand of others. Most stars form within *embedded clusters* (collections of young stars fully or partially shrouded in their natal gas) although many will not spend most of their lives as parts of gravitationally bound star clusters (Lada & Lada 2003; Portegies Zwart et al. 2010). Most stars also form as part of *multiple stellar systems* (Reipurth et al. 2014, and references therein), which are gravitationally bound systems of a few stars orbiting a common centre of mass. Multiple stellar systems are most commonly made up of two stars; such systems are thus called *binary star systems* or, more succinctly, *binaries*. For massive stars, hierarchical systems with three or four stars – where, for example, an outer component orbits an inner massive binary or a pair of binaries orbit each other – are also frequent (e.g. Sana et al. 2012; Moe & Di Stefano 2017, and references therein). It could be said, in a simple manner, that stars form alongside other

stars, on both small and large scales. The formation of binary systems within embedded clusters is therefore an ubiquitous outcome of star formation.

The interplay between star clusters and binaries is complex. Observations reveal correlations between stellar multiplicity and environment, with multiplicity generally decreasing with increasing stellar density in clusters (e.g. Duchêne et al. 1999; Milone et al. 2016). They also reveal a decrease of multiplicity with stellar age (e.g. Duchêne & Kraus 2013, and references therein). Observations of embedded clusters, as well as star forming regions and young stellar associations, highlight this complexity by revealing a wide variety of behaviours from different surveys: some clusters and associations are observed to have fewer binaries than the Galactic field, while others have similar (e.g. Sana & Evans 2011; Duchêne et al. 2018) or higher multiplicities (e.g. Duchêne et al. 1999; Duchêne et al. 2018). Simulations of star clusters with (e.g. Parker & Meyer 2014) and without (e.g. Wall et al. 2019) an initial population of binaries further reveal both formation and destruction of binaries in clusters via dynamical interactions between the stars. This indicates that the properties – and indeed, the very existence – of binaries in clusters and in the Galactic field are directly impacted by the stars’ birth environment.

Previous numerical studies of the interplay between gravitational dynamics in star clusters and binaries are however insufficient to fully address the question of how dynamical interactions in star clusters act upon a population of binaries arising directly from the physics of star formation (i.e. *primordial binaries*). Indeed, many (if not all) of these studies have been conducted without modelling hydrodynamics, let alone active star formation. Modelling star formation, hydrodynamics and stellar dynamics concurrently on the scale of binary systems is computationally challenging, but is likely to be fundamental to our understanding of the formation and long-term evolution of the most massive, densest clusters, *globular clusters* (GCs). As binaries are more massive than

single stars, mass segregation causes them to sink to the core of GCs, where they undergo numerous gravitational interactions. Dynamically, they set the maximum stellar density in a GC by halting core collapse. Gravitational interactions between binaries and single stars, or between pairs of binaries, also tighten the orbits of binaries and inject kinetic energy into the cluster, thus contributing to its dissolution (e.g. Heggie 1975; Hills 1975). Binaries may further play a role in the rise of the chemical abundance variations (so-called *multiple populations*) observed in globular clusters by enriching the gas before the end of star formation via mass loss from O-star binaries (De Mink et al. 2009; Howard et al. 2019).

An accurate and complete understanding of star formation requires an understanding of physical processes ranging from the sub-astronomical units (AU) scale fragmentation of protostellar disks and cores to the kiloparsec (kpc) scale behaviour of *Giant Molecular Clouds* (GMCs) in their galactic environments. Even without attempting to account for galactic effects or resolve the physics governing the formation of individual stars, numerical work remains challenging due to the highly multi-scale, multi-physics nature of clustered star formation. Gravitational interactions between the stars must be resolved down to a few AUs, to encapsulate the behaviour of short-period binaries. These systems are often interacting, and their evolution is important for the larger-scale evolution of the cluster – for example, a massive star may lose enough mass to delay its explosion as a supernova, which will in turn influence the global star formation efficiency of the natal cloud. Gas flows on the scale of a few parsecs (pc) must also be properly traced to account for the spatial distribution of star formation within the cloud, and to follow the effects of stellar winds and supernovae. A large range of physical scales must thus be captured by numerical work to encapsulate the relevant physical processes of star formation – taking place in embedded clusters, and giving rise to a population of multiple stellar systems. Despite these challenges, simulations are a useful tool to study the interplay between star cluster formation and binaries, by giving direct insights into the evolution

of a system over time.

In this thesis, we introduce an initial populations of binaries in simulations of star cluster formation including radiation hydrodynamics, stellar dynamics, stellar evolution and stellar feedback. We investigate the modifications to this initial population of binaries in the early stages of cluster formation, before the first supernova. This chapter reviews our current understanding of star cluster formation in Section 1.1 by surveying the physical processes governing clustered star formation as well as seminal and recent insights from observations and simulations. A discussion of the effects of early stellar feedback on embedded clusters is presented in Section 1.2. An overview of stellar multiplicity and the properties of multiple stellar systems in different environments then follows in Section 1.3. The structure of this thesis is outlined in Section 1.4.

## **1.1 Star cluster formation**

Stars form within massive clouds of molecular hydrogen, called *Giant Molecular Clouds* (GMCs). Within the Milky Way, most star formation takes place within clouds with masses between  $10^5 M_{\odot}$  and  $5 \times 10^6 M_{\odot}$ , but a larger number of clouds have lower masses (Heyer & Dame 2015). Extragalactic GMCs are observed with masses between  $10^4 M_{\odot}$  and  $10^7 M_{\odot}$  (Fukui & Kawamura 2010). We can thus reasonably consider that star formation generally takes place in clouds of masses  $10^4$ - $10^7 M_{\odot}$ . GMCs are cold – with temperatures on the order of 10 K (Heyer & Dame 2015) – and turbulent, which promotes the formation of high density filaments. The densest regions, often at the intersection of filaments, collapse under their own gravity and form first dense cores, then stars, on timescales of a few million years (Myr). Each dense region may form tens or hundreds of stars, and the larger scale gravitational interactions within a molecular cloud may then bring together these groups of stars as they move along filaments. We understand cluster formation to be a hierarchical process, with the merging of many

small groups of stars building up the stellar mass of a cluster over a few Myr (Vázquez-Semadeni et al. 2017; Grudić et al. 2018; Howard et al. 2018).

The balance between the effects of self-gravity in a cloud and its support by turbulence is described by the virial parameter  $\alpha$ ,

$$\alpha \equiv \frac{2T}{|U|} = \frac{5\sigma^2 R}{GM} \quad (1.1)$$

where  $T$  is the kinetic energy of the cloud and  $U$  its gravitational binding energy,  $\sigma$  is the velocity dispersion,  $R$  is the radius,  $M$  is the mass and  $G$  is the gravitational constant (Bertoldi & McKee 1992, for a spherical cloud). Similarly, the energetic state of a stellar system such as a cluster is described by the virial ratio, defined as the ratio between kinetic and gravitational binding energy (following Portegies Zwart et al. 2010),

$$Q_{vir} \equiv \frac{T}{|U|}. \quad (1.2)$$

We adopt here this second convention for both the virial parameter of GMCs  $\alpha$  and the virial ratio  $Q_{vir}$  of star clusters, for consistency. In later sections of this thesis, the virial parameter will therefore be defined as

$$\alpha \equiv \frac{T}{|U|} = \frac{5\sigma^2 R}{2GM}. \quad (1.3)$$

GMCs with  $\alpha = 0.5$  are thus in virial equilibrium, while GMCs with  $\alpha < 0.5$  are sub-virial and those with  $\alpha > 0.5$  are super-virial; clouds with  $\alpha \lesssim 1$  are gravitationally bound (see e.g. Sun et al. 2018). A wide range of virial parameters is observed for molecular clouds in galaxies, from  $\lesssim 0.4$  to  $\gtrsim 5$  (Lee et al. 2016a; Sun et al. 2018; Schruba et al. 2019). Lower mass clouds tend to have lower virial parameters (e.g. Schruba et al. 2019), as do dense clumps within larger GMCs. This is consistent with the multi-scale, hierarchical structure of GMCs – the densest regions may be collapsing

while the larger scale global structure appears supported by turbulence (see Chevance et al. 2020, and references therein). Nonetheless, most surveys find median values of  $\alpha$  of  $\sim 1 - 2$  in nearby galaxies: for example, Sun et al. (2018) obtain galaxy-averaged values of 0.75-1.50 while Schrubba et al. (2019) obtain values slightly above 2.

Star formation is an inefficient process. Indeed, only a small fraction (often quoted as 1%, see Dobbs et al. 2014; Krumholz et al. 2019; Chevance et al. 2020, and references therein) of the gas in a cloud is turned into stars per free fall time. The *star formation efficiency* (SFE) also depends on the boundedness of the cloud or, implicitly, on whether the full cloud or only the star-forming, densest regions are considered: Schrubba et al. (2019) find a star formation efficiency per free fall time  $\epsilon_{ff} = 1\% - 3\%$  for GMCs with virial parameters  $\alpha = 0.5 - 1.5$  and  $\epsilon_{ff} = 0.1\% - 0.7\%$  for GMCs with  $\alpha = 2.5 - 5.0$ . This low efficiency is driven by the properties of the clouds themselves, as well as the effects of the stars unto their surroundings. Molecular clouds are supported against collapse under their own gravity by supersonic turbulence and magnetic fields (see Padoan et al. 2014, and references therein). Turbulence both prevents and promotes star formation: on global scales, turbulence prevents gravitational collapse while on small scales, turbulence gives rise to regions of high density that are perfectly suited to star formation (Ballesteros-Paredes et al. 2007). The amount of turbulence in a GMC is often measured via its virial parameter, from the velocity dispersion. On cloud scale, supervirial GMCs have lower *star formation rates* (SFR) than virial or subvirial GMCs. Magnetic fields also play a role in supporting molecular clouds against collapse and are likely to slow down star formation or delay its onset (Price & Bate 2008).

Star cluster masses' span a few orders of magnitudes, from stellar clusters and associations (not gravitationally bound, Krause et al. 2020) with masses on the order of  $10^2 M_{\odot}$  to the massive, dense and old *Globular Clusters* (GCs) and their younger counterparts, *Young Massive Clusters* (YMCs) with masses of up to  $10^7 M_{\odot}$  (Krumholz et al.

2019, and references therein). Although star formation in embedded clusters is the most ubiquitous mode of star formation in galaxies, most stars will become unbound from their natal cluster – or were never bound to the stars they formed with – and join the Galactic field over timescales of a few Myr to a few Gyr (e.g. Lada & Lada 2003; Krause et al. 2020, and references therein). The boundedness of young clusters or associations is hard to determine observationally. Indeed, boundedness is often estimated from the stars’ virial ratio and thus from the observed stellar velocity dispersion. A large number of unresolved binaries may however lead to an overestimate of the velocity dispersion, which should be calculated from the motions of bound systems’ centres of mass, and not from the motions of individual stars. Star clusters that are gravitationally bound may thus appear unbound (e.g. Gieles et al. 2010; Hénault-Brunet et al. 2012). The effects of this overestimate of the velocity dispersion are also seen in the context of mass estimates (see e.g. Rastello et al. 2020).

The main driver of cluster dissolution within the first few Myr of evolution (often known as *infant mortality*, Lada & Lada 2003) is the rapid removal of the gravitational potential of the gas from feedback from massive stars. The low *cluster formation efficiency* (CFE, the fraction of the stellar mass found in bound clusters) – around 10% (see e.g. Lada & Lada 2003; Kruijssen 2012) – may also be driven by what Krumholz et al. (2019) refer to as *infant weight loss*: upon gas removal, a large fraction of the stars become unbound from their natal cluster. On longer timescales, clusters may also lose mass via stellar evolution (in the form of winds and supernovae), by tidal shocks with GMCs and by tidal stripping (Krumholz et al. 2019; Krause et al. 2020, and references therein). The position of a cluster within the gravitational potential of its host galaxy – and so the tidal forces it experiences, as well as how often it crosses the disk of the galaxy – will influence how much mass is lost. Cluster survival on Gyr scale will thus be influenced by mass and environment. Note that on timescales comparable to that of star formation, however, Galactic effects are unlikely to have much of an effect; the

dissolution of clusters on Myr timescales is driven by rapid gas expulsion.

Despite the different fates of embedded clusters, it is now understood that a common physical process governs star cluster formation on all scales (Kruijssen 2015; Howard et al. 2018), with the most massive clusters arising from the hierarchical merging of small sub-clusters (Vázquez-Semadeni et al. 2017; Grudić et al. 2018; Howard et al. 2018). Although a significant fraction of stars does not form in bound clusters (e.g. Kruijssen 2012), most stars form in an environment where they are likely to undergo dynamical interactions with other stars. It is thus expected that the populations of binaries in both bound star clusters and the Galactic field will be set by a superposition of primordial binaries – arising directly from the physics of star formation – and the dynamical formation or destruction of binaries by gravitational interactions during clustered star formation or cluster evolution.

## **1.2 Stellar feedback in embedded clusters**

The rate of star formation in GMCs is also regulated by feedback from the stars embedded within the star-forming gas. The effects of feedback are most important during cluster formation itself, while there are still stars forming and the most massive stars have not yet reached the end of their lives. Feedback depletes the reservoir of molecular gas available for star formation by either removing mechanically the gas from the star forming region or by raising its temperature enough to prevent its collapse. Different feedback mechanisms act on different time and spatial scales; the types of feedback that have the strongest influence on an embedded cluster depend on the properties – mass, size, stellar content – of the cluster itself (Krumholz et al. 2019, and references therein). An illustration of the regions of parameter space at which different forms of feedback are most effective is shown in Figure 1.1. Feedback eventually carves away the cold gas

supply and clears out the regions surrounding massive stars. An observational illustration of the effects of feedback can be seen in the Trapezium Cluster, in Figure 1.2, where the bright O-stars in the centre have carved away the gas along our line of sight. We present here an overview of recent and seminal observational, theoretical and computational work on feedback in embedded clusters, with a focus on the effects of stellar winds and photoionizing radiation.

### **Protostellar outflows**

The form of feedback that acts first on an embedded cluster is protostellar outflows and jets. Simulations (e.g. Federrath 2015; Offner & Chaban 2017) indicate that the combination of magnetic fields, turbulence and protostellar outflows is effective at lowering the star formation efficiency per free-fall time, by ejecting approximately 75% of the mass accreted onto an individual protostar (Offner & Chaban 2017). The momentum per unit mass of protostellar outflows is set by the escape velocity at the surface of protostars, and thus depends only weakly on stellar mass: protostellar feedback is provided not only by massive stars, but also by low-mass stars (Matzner & McKee 2000). Observations (e.g. Plunkett et al. 2015) and theoretical models (e.g. Matzner & Jumper 2015) however indicate that outflows are most effective in low-mass star forming regions and that massive stars, when present, dominate the feedback budget of the embedded cluster. Only feedback from massive stars succeeds in disrupting the cloud: outflows lower the star formation rate but have little influence on the time-integrated star formation efficiency as they are unable to eject the outflowing material from the embedded cluster. Protostellar feedback is thus the dominant feedback channel only in the lowest-mass clusters ( $\lesssim 10^2 M_{\odot}$ , see Figure 1.1).

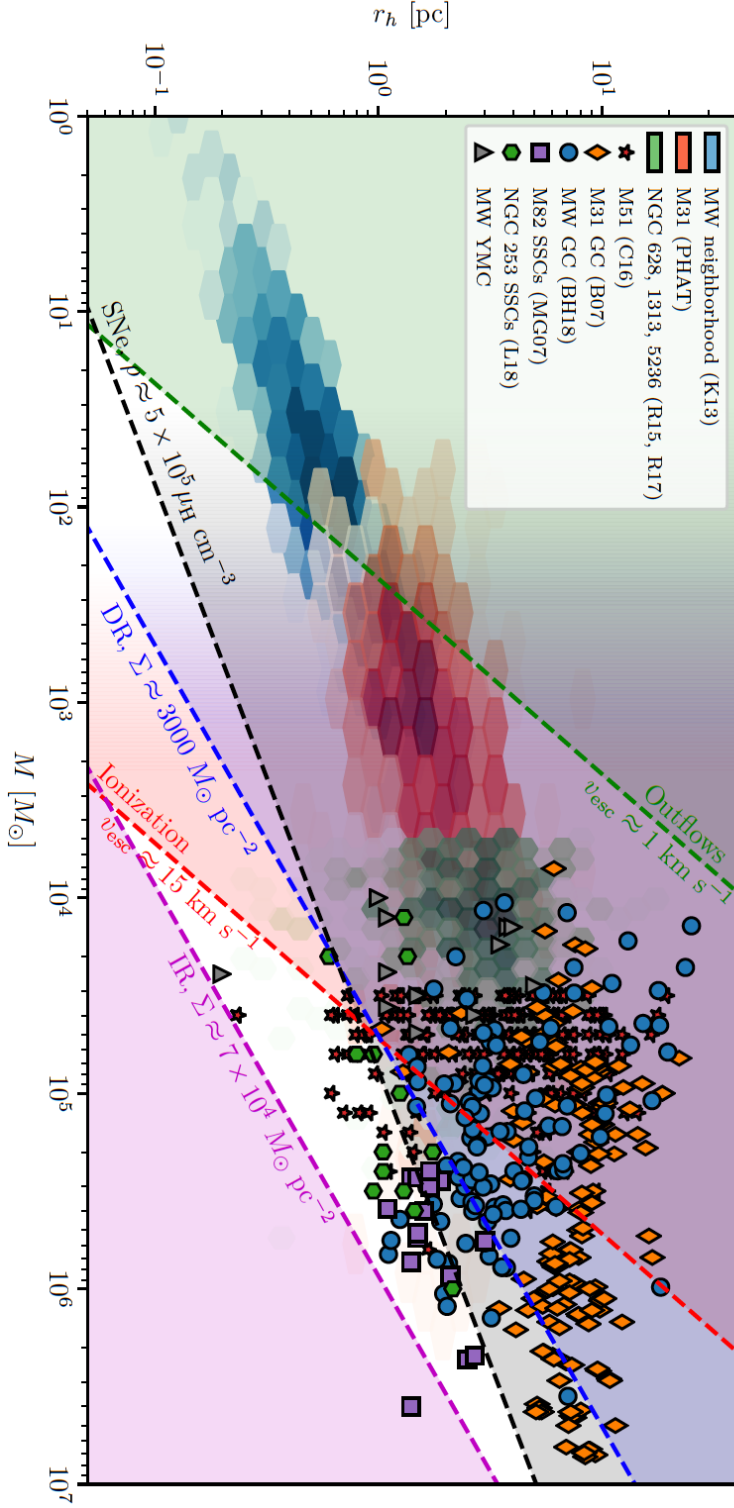


FIGURE 1.1: Importance of different feedback mechanisms as a function of cluster mass and size. The horizontal axis is the stellar mass and the vertical axis is the half-mass radius. Observed Galactic and extragalactic clusters are shown as shaded hexagons and data points. The green line denotes protostellar outflows and jets; the black line denotes supernovae, the blue line denotes direct radiation pressure and the red line denotes ionizing radiation. The feedback mechanisms are effective in the associated shaded regions; the combination of winds (not shown) and photoionization is most effective for escape velocities  $v_{esc} \lesssim 5$  km/s (Dale et al. 2014). Credit: Krumboltz, McKee & Bland-Hawthorn, 2019, *ARA&A*, 57, 227, Figure 12. Reproduced with permission, © Annual Review.



FIGURE 1.2: Hubble Space Telescope view of the Trapezium cluster, processed by Robert Gendler. The Trapezium cluster lies within the Orion Nebula (M42), a star-forming region with a total mass in gas of at least 10,000 times the mass of the Sun and 3,500 stars. The four bright stars in the middle of the image are massive O-stars that are likely responsible for removing the gas from within the cluster via radiative and momentum feedback. At least two of these massive stars are in binaries. *Credit: R. Gendler and NASA/ESA/Hubble.*

## **Supernovae**

Conversely, the form of feedback that likely acts last on an embedded cluster is core-collapse (or type II) *supernovae* (SNe) arising from the violent death of massive stars. Unlike other forms of stellar (or protostellar) feedback, SNe are singular events and are delayed from star formation: the first supernova cannot be expected before  $\sim 3$  Myr, or even longer if the most massive stars are in interacting binaries (e.g. Sana et al. 2012). The importance of SNe compared to stellar winds and radiation is still debated, although the amount of energy injected from SNe and winds is comparable (see Krumholz et al. 2019). Rogers & Pittard (2013) find that stellar winds are more effective than SNe at disrupting molecular clouds: SNe ejecta couple weakly with the surrounding gas, already shaped by the effects of stellar winds, and thus most (99%) of the SN energy is radiated away. Körtgen et al. (2016) conclude that SNe can only remove the gas from  $\sim 10$  pc regions but fail to affect the entire GMC, unless many SNe are clustered in time and space. Similarly, Geen et al. (2016), in simulations including SNe and photoionizing radiation, find that a single SN fails to regulate star formation. A schematized picture of stellar feedback would thus suggest that supernovae are not the dominant feedback mechanism in embedded clusters.

## **Stellar winds**

Stellar winds from main-sequence stars, variable or eruptive stars, and Wolf-Rayet stars influence both the evolution of stars (e.g. by delaying SNe if the star is in an interacting binary) and of the molecular cloud in which it sits. Winds inject momentum and energy into the gas in the form of fast ( $\sim 10^3$  km/s) material escaping the stars, giving rise to hot ( $\sim 10^7$  K) shock fronts (Krumholz et al. 2019, and references therein). Despite recent work showing that classical empirical (De Jager et al. 1988) and theoretical (Vink et al. 2000) estimates of the mass-loss rates are likely overestimated by a factor of  $\sim 3$  (Smith 2014, and references therein), winds are still understood as an important component of

stellar and cluster evolution. The interplay between stellar winds and binaries is also both central to the evolution of embedded clusters, and complex: most massive stars are in binary systems that will interact over their lifetimes (Sana & Evans 2011; Sana et al. 2012), but these stars are also those with the most violent winds. Simulations show that winds have a strong effect on the gas morphology of embedded clusters, and participate in reducing the star formation efficiency. Rogers & Pittard (2013) find that the sparsest regions of GMCs are dispersed by winds but that the densest regions are resistant to wind feedback; 60%-75% of the energy from the winds escapes the cluster. They also note that winds sweep up from the surrounding GMC a few  $10^2$  times the amount of mass that is ejected from the stars – the cluster’s mass loss from winds is thus several orders of magnitude larger than the stars’ mass loss rates. In simulations with momentum-driven winds and radiation, Dale et al. (2014) find that winds are effective at carving out cavities on the scale of 10 pc; for clouds with escape velocities  $\lesssim 5$  km/s, the combination of winds and photoionization is highly destructive. Most of the effective feedback from winds is mechanical, not thermal: winds drive out large amounts of material from the star-forming regions, but shock fronts cool rapidly due to their large surface (arising from their asymmetrical structure) and turbulent mixing (see Lancaster et al. 2021a; Lancaster et al. 2021b).

### **Direct radiation pressure**

Direct radiation pressure – deposition of momentum into the gas by the ultraviolet photons from massive stars – participates in mechanically removing gas from embedded clusters. During the early stages of YMC formation, direct radiation pressure suppresses gas accretion and thus prevents cluster growth. Krumholz & Matzner (2009) compare the effects of direct radiation pressure to those of stellar winds and supernovae, and argue that direct radiation pressure dominates the evolution of HII regions in the most massive clusters. Murray et al. (2010) find that direct radiation pressure dominates over

stellar winds and protostellar jets for clusters with masses  $10^7 - 10^8 M_{\odot}$ . Howard et al. (2018) further compare the effects of direct radiation pressure and photoionization, and conclude that radiation pressure dictates the evolution of clusters forming within GMCs of masses  $\sim 10^7 M_{\odot}$ . It is likely the prevalent form of feedback in YMCs, and is most effective in clusters with large escape velocities ( $v_{esc} \gtrsim 10$  km/s, Krumholz et al. 2019).

### **Photoionizing radiation**

Photoionizing radiation ionizes the hydrogen gas near massive stars and heats it to  $\sim 10^4$  K, corresponding to the energy required for ionization. The hot gas then escapes the embedded clusters via leakage through the sparser regions. Photoionization is most effective in GMCs with masses  $\lesssim 10^4 M_{\odot}$  or the less dense GMCs with masses up to  $10^5 M_{\odot}$ , for which the escape velocities are below the HII region expansion speed of 10 km/s (e.g. Dale et al. 2012). Conversely, photoionization is not sufficient to regulate star formation in higher mass clouds ( $10^6$ - $10^7 M_{\odot}$ , Howard et al. 2018). From magneto-hydrodynamics simulations of  $10^5 M_{\odot}$  GMCs, Geen et al. (2016) conclude that photoionization is sufficient to disperse the cloud if the star formation efficiency is at least 10%. These results are likely lower limits, however, at least in terms of the number of photoionizing photons emitted. A common technique to estimate the number of photoionizing photons is to treat the stars as blackbody emitters, using surface temperatures from stellar evolution models (e.g. Wall et al. 2019), which depends strongly on mass. The ionization budget is therefore dominated by the most massive stars, which are most often part of binary systems that will interact on the main sequence (Sana et al. 2012). Stars that are stripped from their outer layers by binary interactions are very luminous at ionizing luminosities, which is not accounted for by single star evolution models (Götberg et al. 2018). Simulations (e.g. Gritschneider et al. 2009; Dale et al. 2013) and observations (e.g. Glatt et al. 2010) also suggest that photoionization may promote the formation of dense pillars of gas or interacting shells, that in turn trigger

star formation.

For clusters like the Orion Nebula Cluster, shown in Figure 1.2, with a gas mass of  $\gtrsim 10^4 M_{\odot}$  and a stellar mass of  $\sim 10^3 M_{\odot}$  (Hillenbrand & Hartmann 1998), the dominant feedback mechanisms acting on timescales of  $\lesssim 3$  Myr after the onset of star formation are stellar winds and photoionizing radiation. Binary interactions may further amplify these mechanisms, by promoting mass transfer, stripping away the envelopes obscuring the UV-emitting cores of stars and delaying SNe by reducing the mass of the most massive stars.

### 1.3 Stellar multiplicity in different environments

Stellar multiplicity is a common outcome of star formation, with more than 20% of all stars in the Milky Way in multiple stellar systems (Duchêne & Kraus 2013) and almost all massive stars in close binary systems (Sana et al. 2012). Such close binaries play a crucial role in stellar evolution by giving rise to type Ia supernovae, blue stragglers, classical novae and X-ray binaries, among others. Interacting binaries are also a possible explanation for the spread in chemical abundances observed in a large number of globular clusters (De Mink et al. 2009).

Setting the stage for a discussion of stellar multiplicity requires an overview of some commonly-used vocabulary. In each multiple stellar system, the most massive star is called the *primary*, while the other stars are called *companions*. Two numbers are often used to characterize how likely it is for stars to be in multiple stellar systems. The *multiplicity frequency*  $\mathcal{N}$  denotes the average number of companions attached to a star while the *multiplicity fraction*  $\mathcal{F}$  denotes the fraction of stars with at least one companion. The multiplicity frequency can be larger than one for some stellar populations, such as O-stars, which often have two or three companions. Binary systems are generally characterized, both individually and as a population, by four different properties: (1) the

*primary mass*, (2) the *mass ratio* of the two components (defined as the companion mass over the primary mass), (3) the *orbital period* or the *semi-major axis* of the system, and (4) its *eccentricity*. Primary masses cover more than three orders of magnitude in range – from brown dwarfs to massive O-stars – while orbital periods go from a few hours to millions of years (Duchêne & Kraus 2013; Moe & Di Stefano 2017). By definition, mass ratios and eccentricities are between 0 and 1.

Different physical processes may lead to the formation of multiple stellar systems either during or after star formation. We refer to the multiple systems formed during star formation as *primordial* systems and to those formed after star formation via interactions with stars in the embedded cluster as *dynamical* systems. The fragmentation of protostellar disks is responsible for primordial binary formation on the smallest scales – a few tens of AUs. The stability of rotating disks can be measured from their Toomre (1964)  $Q$  parameter,

$$Q = \frac{c_s \Omega_{epi}}{\pi G \Sigma} \quad (1.4)$$

where  $c_s$  denotes the isothermal sound speed,  $\Omega_{epi}$  denotes the epicyclic frequency (or angular velocity for a Keplerian disk),  $G$  is the usual gravitational constant and  $\Sigma$  denotes the surface density of the disk. Recent work by Takahashi et al. (2016) proposes that disks with  $Q < 1$  (the traditional criterion for stability) are susceptible to spiral arm formation, and that fragmentation takes place in disks with  $Q < 0.6$ . There is evidence from observations (e.g. Tobin et al. 2016a) and simulations (e.g. Sigalotti et al. 2018) that disk fragmentation is a viable mechanism for binary formation. Kratter (2011), in an overview of the formation of close binaries, suggests that disk fragmentation is most prevalent at high masses, and is the mechanism responsible for the formation of close, massive binaries. Tokovinin & Moe (2020) also propose disk fragmentation as the formation mechanism for close binary formation, with contributions from migration to

reach small separations, below the  $\sim 10$  AU limit set by the opacity limit to fragmentation. On larger scales ( $\sim 1000$  AU), the turbulent fragmentation of cores (Boss & Bodenheimer 1979) gives rise to multiple stellar systems. Simulations including protostellar feedback (Offner et al. 2010; Guszejnov et al. 2017) and observations of misaligned outflows in protostellar binaries (Lee et al. 2016b; Lee et al. 2017) indicate that core fragmentation is a viable mechanism for the formation of multiple stellar systems. Binaries can also form as a by-product of dynamical interactions during clustered star formation, either from nearby cores than have low relative velocities (Tokovinin 2017), from the dissolution of the cluster into the Galactic field (e.g. Kouwenhoven et al. 2010) or its early evolution (e.g. Parker & Meyer 2014; Wall et al. 2019).

Protostars are understood to have higher multiplicity than main-sequence field stars, at equal masses (Duchêne & Kraus 2013; Reipurth et al. 2014) – it is however worth noting that the large-scale surveys available for main-sequence field stars are currently not available for protostars embedded in gas. Tobin et al. (2016b) report a decrease in multiplicity with increasing age for protostars in the Perseus molecular cloud, associated with an excess of wide binaries for the youngest systems. The effects of age and environment are not easily disentangled: in their review of stellar multiplicity in main-sequence stars, Duchêne & Kraus (2013) find that multiplicity is constant at twice the field fraction over the first  $\lesssim 50$  Myr of evolution of low-density star-forming regions, while it is consistent within uncertainties for young clusters, open clusters, and the Galactic field. The idea that dense environments may disrupt primordial binaries and lead to an overall decrease of the multiplicity fraction is also supported by observations of decreasing binary fraction with increasing cluster mass in GCs (e.g. Milone et al. 2016).

The population of multiple stellar systems observed in the Galactic field likely arises from a combination of primordial multiplicity and subsequent dynamical modifications within different environments. Reviews of stellar multiplicity in the Galactic field by

Duchêne & Kraus (2013) and, more recently, by Moe & Di Stefano (2017), nonetheless reveal trends that are likely robust to changes in environment:

1. Multiplicity increases with primary mass. Massive O-stars have on average more than one companion, and most have at least one companion with which they will interact over their main-sequence lifetime (Sana et al. 2012). Dynamical interactions likely increase this fraction, as a massive O-star is expected to replace the lowest-mass object if it interacts with a binary (Sigurdsson & Phinney 1993).
2. Even at low masses, multiplicity is common (e.g. Winters et al. 2019). Since low-mass stars account for most of the stars in the Galaxy, dynamical interaction mediated by low-mass binaries likely play a role in cluster evolution.
3. The distribution of mass ratios depends on the mass of the primary. At large masses, equal-mass pairs are favoured; in particular, massive stars tend to have at least one close, massive companion (Sana et al. 2012). Observational limits make it likely the number of companions with low mass ratios is underestimated.
4. The distributions of orbital periods (or separations) and eccentricities depend on the mass of the primary. Massive stars span a large range of separations, from very short period systems that will interact over their main-sequence lives to wide systems that are only stable due to large gravitational attraction between their components (Moe & Di Stefano 2017).

The key takeaway from the reviews by Duchêne & Kraus (2013) and Moe & Di Stefano (2017) is that the pairing of stars in binary systems is not random (see Kouwenhoven et al. 2010, for a discussion of pairing functions consistent with observations). Some systems are more likely to form than others, whether primordially or dynamically. The relative importance of primordial and dynamical formation of multiple stellar systems in setting the populations of binaries in the field and in clusters is however currently unknown.

Simulations of young clusters with a field-like initial population of binaries (Parker & Meyer 2014) and the similarities between the binary fraction in the field and in young clusters (Duchêne & Kraus 2013) nonetheless suggest that the field population is a reasonable first-order estimate of the properties of binaries at birth.

## 1.4 Thesis outline

As outlined above, stars form alongside other stars, on both small and large scales, in environments that are shaped by the stars themselves via radiative and mechanical feedback. In the earliest stages of a star’s life, it is likely to interact gravitationally with other stars, which makes it non-trivial to determine the properties of binary systems at birth from the population of binaries in the Galactic field or in older star clusters. In this thesis, we are interested in disentangling how a primordial population of binary systems is modified by gravitational interactions with other stars in embedded clusters and by interactions with the surrounding gas. We probe these questions using numerical simulations conducted using TORCH (Wall et al. 2019).

In particular, we are interested in modelling a system that is not too computationally expensive but that is massive enough to allow massive stars – which are almost always in binaries – to form. We include in Figure 1.2 a picture of the Orion Nebula Cluster, with the bright stars of the Trapezium Cluster in the foreground, as an observational counterpart to what we are modelling. The gas mass associated with the cluster is on the order of  $\sim 10^4 M_{\odot}$ , and the cluster contains  $\sim 3500$  stars (Hillenbrand & Hartmann 1998). Images of the Orion Nebula Cluster are dominated by the massive Trapezium stars, at least two of which are in binary or higher order systems (e.g. Grellmann et al. 2013). To model a similar system, we start from  $10^4 M_{\odot}$  of gas and model active star and binary formation, with implementations of stellar feedback in the form of stellar winds, ionizing radiation and radiation pressure.

In Chapter 2, we present an overview of the general numerical methods used in this work for stellar and gas dynamics, as well as stellar feedback. We also review other recent numerical work on star cluster formation. Chapter 3 is the main chapter of this thesis. It was published in the *Monthly Notices of the Royal Astronomical Society* in March 2021 and is reproduced here in full. In this chapter, we present the implementation of our new binary generation algorithm and sketch a picture of how a primordial population of binaries is modified by dynamical interactions before the evolution of the cluster becomes dominated by feedback. In Chapter 4, we outline the key results from our published suite of simulations and discuss their broader implications. We also present a discussion of our ongoing work and of possible directions for further research.

## CHAPTER 2

# NUMERICAL METHODS FOR STAR CLUSTER FORMATION

We present in this chapter the relevant numerical methods for our work. In Section 2.1, we discuss the equations of hydrodynamics and the numerical tools and techniques we use to solve them. In Section 2.2, we present the subgrid model for star formation in our simulations. The methods specific to binary formation, developed as part of this thesis, are presented in Chapter 3. In Section 2.3, we discuss the numerical methods we use to calculate stellar dynamics on both cluster and binary scales. In Section 2.4, we outline the models for wind and radiation feedback in our simulations, and their numerical implementation. Recent and relevant advances in multi-physics numerical methods for star cluster formation are summarized in Section 2.5.

### 2.1 Numerical hydrodynamics

Numerical hydrodynamics are concerned with providing numerical solutions to the equations governing the dynamics of fluids. Astrophysical applications of numerical hydrodynamics (HD) are focused on compressible (and often supersonic) gas flows. These

methods can be applied to problems ranging from cosmological simulations of galaxy formation (e.g. FIRE, Hopkins et al. 2014; EAGLE, Crain et al. 2015, Schaye et al. 2015; Auriga, Grand et al. 2017) to simulations of the formation of a stellar system (e.g. Boss & Bodenheimer 1979; Bate et al. 1995; Sigalotti et al. 2018). In star and star cluster formation, numerical hydrodynamics focus on describing the behaviour of the turbulent *interstellar medium* (ISM) in the form of molecular clouds, filaments and outflows (recently, Gavagnin et al. 2017; Grudić et al. 2018; Howard et al. 2018; Wall et al. 2019; Guszejnov et al. 2020, and others).

The equations of HD can be written in a conservative form as a set of five equations, often referred to collectively as the Euler equations (Bodenheimer et al. 2006, §1; Toro 2009, §1). The variables conserved by this hyperbolic set of partial differential equations (PDEs) are the mass density  $\rho$ , the momenta  $\rho v_x$ ,  $\rho v_y$  and  $\rho v_z$ , and the total energy per unit mass. These conservation laws thus arise naturally from conservation of mass and energy, and Newton’s second law of motion (see Toro 2009, §1 for an overview). The Euler equations are laid out in Equation 2.1 (c.f. Fryxell et al. 2000),

$$\frac{\partial \rho}{\partial t} + \nabla \cdot \rho \mathbf{v} = 0 \quad (2.1a)$$

$$\frac{\partial}{\partial t} (\rho \mathbf{v}) + (\nabla \cdot \rho \mathbf{v}) \mathbf{v} + \nabla P = \rho \mathbf{g} \quad (2.1b)$$

$$\frac{\partial \rho E}{\partial t} + \nabla \cdot (\rho E + P) \mathbf{v} = \rho \mathbf{v} \cdot \mathbf{g} \quad (2.1c)$$

where  $\rho$  denotes the fluid density,  $\mathbf{v}$  denotes the fluid velocity,  $P$  denotes the pressure,  $E$  denotes the total energy per unit mass and  $\mathbf{g}$  denotes the acceleration due to gravity. The total fluid energy per unit mass  $E$  is the sum of the internal energy  $\epsilon$  and the kinetic energy per unit mass,

$$E = \frac{1}{2} v^2 + \epsilon. \quad (2.2)$$

The variables can be related via a closure relation, in the form of an equation of state.

Under the assumption of an adiabatic gas (if heating and cooling are present, they are not handled by the HD solver), the equation of state is

$$P = (\gamma - 1)\rho\epsilon \quad (2.3)$$

where  $\gamma$  is the adiabatic constant of the fluid. For an ideal gas,

$$\gamma = \frac{N + 2}{N} \quad (2.4)$$

where  $N$  is the number of degrees of freedom of a gas particle (Toro 2009, §1). Ionized and neutral atomic hydrogen have three degrees of freedom; although molecular hydrogen nominally has five degrees of freedom, its vibrational states are hard to excite (Rybicki & Lightman 2004, §11), allowing us to model it with three degrees of freedom for all practical purposes. Setting  $\gamma = 5/3$  is thus a standard choice in simulations of the ISM, as it accounts for molecular and atomic hydrogen, as well as hot ionized gas around massive stars.

We consider the Eulerian formulation of hydrodynamics, in which we solve the Euler equations for fixed volume elements by calculating the flows of mass, momentum and energy in and out of the volume elements (Bodenheimer et al. 2006, §6). In Eulerian numerical HD, the computational domain is separated into finite volume elements, often called *cells*, that cover the entire domain. For each pair of adjacent cells, the Rankine-Hugoniot conditions (Macquorn Rankine 1870; Hugoniot 1885) apply: the fluxes of mass, momentum and energy must be equal on both sides of the shock or contact. Numerically, solving the equations of hydrodynamics amounts to solving the Riemann problem in three dimensions, between each pair of adjacent cells: given the pressure and density on each side of the cell boundary and the Rankine-Hugoniot conditions, we calculate the pressures, densities and velocities after a time interval  $\Delta t$ . Different Riemann solvers use different schemes for advection (i.e. different numerical approximations for the fluxes),

which differ in their accuracy, stability and computational cost. Eulerian codes, or grid codes, can have non-uniform levels of spatial resolution in different regions of the computational domain, to allow for a good resolution in the regions of interest (e.g. dense star-forming filaments) while reducing the computational costs elsewhere in the domain (e.g. sparse and uniform background gas, Bodenheimer et al. 2006, §6). This technique is called *Adaptive Mesh Refinement* (AMR). FLASH (Fryxell et al. 2000), which we use in the thesis, is an AMR code.

Although our current suite of simulations does not include magnetic fields, TORCH is a *magneto-hydrodynamics* (MHD) code, and the methods it was developed with reflect the need for solving the full MHD equations instead of merely the Euler equations. We thus use a three dimensional unsplit staggered mesh MHD solver (Lee 2013), which reduces to the unsplit HD solver in the absence of magnetic fields. It uses a predictor-corrector method (Press et al. 2007, §17). The predictor states are calculated using a third order piecewise parabolic reconstruction method (Colella & Woodward 1984), before they are corrected with a Harten–Lax–van Leer Riemann solver resolving discontinuities (HLLD, Miyoshi & Kusano 2005), which reduces to a Harten–Lax–van Leer contact Riemann solver (HLLC, Toro et al. 1994) in the absence of magnetic fields. The gas self-gravity is handled by solving the Poisson equation with Dirichlet boundary conditions in each cell, with a multigrid solver (Ricker 2008). We also use artificial viscosity (Von Neumann & Richtmyer 1950) to improve numerical stability at shocks, common in astrophysical simulations.

We use simultaneously two types of refinement criteria for the adaptive grid in our simulations. We first refine based on the Truelove et al. (1997) criterion as implemented by Federrath et al. (2010), which states that the Jeans length  $\lambda_J$  (Jeans 1902)

$$\lambda_J = \left( \frac{\pi c_s^2}{G\rho} \right)^{1/2}, \quad (2.5)$$

must be resolved by at least four resolution elements in order to avoid numerical fragmentation. In Equation 2.5,  $c_s$  denotes the sound speed and  $\rho$  denotes the density, while  $G$  is the gravitational constant. The second criterion is based on the second derivative (Lohner 1987; MacNeice et al. 2000): we refine where the magnitude of the second derivative of a variable is of the order of the sum of its gradients. We refine on pressure, temperature, total energy and internal energy, which improves numerical stability compared to refining only based on the Truelove criterion.

The gas is also influenced by the gravitational attraction from the stars, and vice-versa. We account for their effects on one another with a leapfrog-type bridge scheme (Fujii et al. 2007) implemented in TORCH by Wall et al. (2019). The gravitational attraction from the gas on the stars is calculated directly from the potentials obtained with the multigrid Poisson solver (Ricker 2008). The gravitational attraction from the stars on the gas is calculated via a cloud-in-cell mapping of stars' masses on the grid that is then used to calculate the potentials (and thus the accelerations) with the Poisson solver (Wall et al. 2019). This scheme allows for the hydrodynamics and the stellar dynamics (discussed in Section 2.3) to be evolved in parallel.

## **2.2 Sink particles**

Sink particles (Bate et al. 1995; Krumholz et al. 2004, for Eulerian codes) are used in numerical simulations to replace collapsing regions – ranging in size from individual stars or protostars (e.g. Offner et al. 2010; Federrath 2015; Haugbølle et al. 2018; Guszejnov et al. 2020) to entire star clusters (e.g. Dale et al. 2014; Howard et al. 2016; Körtgen et al. 2016) – by a sub-grid representation. This allows the simulations to retain a timestep consistent with the physical timescales involved in the simulations, while avoiding important slow-down due to the smallest collapsing regions. In our simulations, sink particles represent individual dense regions in molecular clouds. Sink particles are implemented

in Torch following Federrath et al. (2010). For each cell where the density exceeds a density threshold

$$\rho_{res} = \frac{\pi c_s^2}{G \lambda_J^2} \quad (2.6)$$

a series of verifications is performed before forming a sink particle with an accretion radius of 2.5 resolution elements. The sink itself is a point particle. In Equation 2.6, the variables are all defined as above and the Jeans length  $\lambda_J$  is set to five resolution elements at the highest refinement level to enforce the Truelove et al. (1997) criterion. In our simulations, this length scale also corresponds to the scale at which turbulence goes from supersonic to subsonic (Federrath et al. 2021). The checks from Federrath et al. (2010), outlined below, are performed on all the cells within a spherical volume defined by the accretion radius:

1. The cells must be at the highest level of refinement.
2. The gas flow must be converging.
3. The cells must have a gravitational potential minimum at the centre of the volume.
4. The gas within the cells must be gravitationally bound.
5. The gas within the cells must be Jeans unstable.
6. The cells must not be located within another sink particle's accretion radius.

The same sink implementation and sink formation checks are used in Howard et al. (2016), to represent full clusters with a sub-grid model. By contrast, sink particles in TORCH are used as factories for star formation: a list of stars is generated upon sink formation, then stars are individually formed and placed in the simulation as enough mass is accreted by the sink. New stars can be formed at each simulation timestep, which is on the order of 10 years in simulations that are actively star forming. Once decoupled

from the sink particle, the individual stars can then be integrated by the N-body solver. For each sink, the number of stars in each region of the *initial mass function* (IMF, using here Kroupa 2001) is drawn by Poisson sampling of 100 bins equally spaced in mass (Sormani et al. 2017; Wall et al. 2019). For each bin, the calculated number of stars is then drawn randomly from the IMF, and the full list of stars is randomized. Each star receives a position and a velocity upon formation (see Chapter 3 for more details). Additionally, sinks must be located in cold gas ( $T \lesssim 100$  K) to be allowed to form stars, although they may accrete warm gas.

## 2.3 Numerical stellar dynamics

As stated in the previous section, we decouple the stars from the sink particle in which they form and follow closely their dynamics. Stellar dynamics is concerned with using the positions of stars in a system to calculate their accelerations from the net gravitational force exerted on them, and from there using the accelerations to calculate the new positions after a given time interval (Bodenheimer et al. 2006, §3). In other words, stellar dynamics is concerned with solving Newton’s second law for a system of  $N$  objects, moving under gravity alone,

$$\frac{d^2 \mathbf{x}_i}{dt^2} = - \sum_{j=1; j \neq i}^N \frac{G m_j (\mathbf{x}_i - \mathbf{x}_j)}{|\mathbf{x}_i - \mathbf{x}_j|^3} \quad (2.7)$$

where  $\mathbf{x}_k$  denotes a particle’s position,  $m_k$  its mass and  $G$  is the gravitational constant. When  $N > 2$ , there exists no analytic solution to Equation 2.7, which is a non-linear second order differential equation: the equations of motions for a system of  $N$  particles must thus be solved numerically. The most exact methods can only be used for systems with few (i.e.  $N \leq 10$ ) particles, due to their large computational cost. Reasonably accurate methods can nonetheless be used for the type of system we are interested in, with a few  $10^3$  bodies. We present an overview of the relevant techniques below.

Furthermore, the very accurate methods required to resolve the orbits of tight binaries are computationally expensive, as the gravitational attraction between two arbitrarily close bodies becomes arbitrarily large (Bodenheimer et al. 2006, §3). The star clusters with a large fraction of binaries we are interested in have both a fairly large number of particles (a few  $10^3$ ) and a fairly large number of binaries (a few  $10^2$ ). We thus use a different scheme to handle close binaries.

TORCH handles the long-range dynamical interactions between the stars with PH4 (McMillan et al. 2012), a direct N-body code which uses a fourth-order Hermite predictor-corrector scheme (Makino & Aarseth 1992). PH4 is designed for systems with  $\lesssim 10^5$  particles (Portegies Zwart & McMillan 2019, §2), which is appropriate for our simulations. The relevant equations are outlined below (Portegies Zwart et al. *in prep.*). The scheme calculates, for each star, the acceleration  $\mathbf{a}$  and jerk  $\mathbf{j}$  (second derivative of the velocity) and uses them to predict the position  $\mathbf{x}$  and velocity  $\mathbf{v}$  after a time interval  $\Delta t$ ,

$$\tilde{\mathbf{v}}(t + \Delta t) = \mathbf{v}(t) + \mathbf{a}(t)\Delta t + \frac{1}{2}\mathbf{j}(t)(\Delta t)^2 \quad (2.8a)$$

$$\tilde{\mathbf{x}}(t + \Delta t) = \mathbf{x}(t) + \mathbf{v}(t)\Delta t + \frac{1}{2}\mathbf{a}(t)(\Delta t)^2 + \frac{1}{6}\mathbf{j}(t)(\Delta t)^3. \quad (2.8b)$$

where  $\tilde{\mathbf{x}}$  and  $\tilde{\mathbf{v}}$  respectively denote the predicted position and velocity. A predicted acceleration  $\tilde{\mathbf{a}}$  and a predicted jerk  $\tilde{\mathbf{j}}$  are then calculated from the old and predicted position and velocity, for each star. The scheme then corrects the new position and velocity using the predicted acceleration and jerk,

$$\mathbf{v}(t + \Delta t) = \mathbf{v}(t) + \frac{1}{2}\left(\mathbf{a}(t) + \tilde{\mathbf{a}}(t + \Delta t)\right)\Delta t + \frac{1}{12}\left(\mathbf{j}(t) - \tilde{\mathbf{j}}(t + \Delta t)\right)(\Delta t)^2 \quad (2.9a)$$

$$\mathbf{x}(t + \Delta t) = \mathbf{x}(t) + \frac{1}{2}\left(\mathbf{v}(t) + \mathbf{v}(t + \Delta t)\right)\Delta t + \frac{1}{12}\left(\mathbf{a}(t) - \tilde{\mathbf{a}}(t + \Delta t)\right)(\Delta t)^2 \quad (2.9b)$$

Equations 2.8 and 2.9 have leading errors  $\mathcal{O}((\Delta t)^5)$ , making the full scheme fourth-order accurate (Portegies Zwart et al. *in prep.*).

The AMUSE module MULTIPLES (Portegies Zwart & McMillan 2019)<sup>1</sup> handles stable binaries and higher order systems, resonant encounters and scattering (hereafter *multiples* and *encounters*). It makes use of the SMALLN (Hut et al. 1995; McMillan & Hut 1996) and KEPLER codes, both originally developed as part of STARLAB (Portegies Zwart et al. 1999; Hut et al. 2010). MULTIPLES identifies close encounters between stars (or stable multiples) and follows them to completion using its internal N-body solver, SMALLN. To be removed from the N-body code and picked up by MULTIPLES, pairs of stars or stable multiples undergoing an encounter must satisfy the following conditions (Wall et al. 2019):

1. The stars or multiples must be approaching.
2. The stars or multiples must be located within twice the sum of their dynamical radii, set to 100 AU for stars and twice the semi-major axis for binaries in TORCH.
3. The system comprised of the two stars or multiples must be unperturbed by nearby stars. The system is considered unperturbed if, for a primary mass  $M_1$ , a companion mass  $M_2$  and a semi-major axis  $a$ , no neighbour with mass  $M_p$  and distance  $d$  to the system's centre of mass has

$$\frac{4a^2}{M_1 M_2} \left| \frac{M_1 M_p}{(d-a)^2} - \frac{M_2 M_p}{(d+a)^2} \right| > 0.05. \quad (2.10)$$

If any of the above conditions is not satisfied, the encounter is left to handle by the main N-body code, PH4, until all three conditions are satisfied. If the encounter is handled by MULTIPLES, it is evolved as an isolated scattering experiment until the encounter is resolved or a limiting timescale or size is exceeded. Those limits are implemented to avoid the spurious formation of triple systems. Aside from these conditions, there are

---

<sup>1</sup><https://github.com/amusecode/amuse/blob/python2/src/amuse/couple/multiples.py>  
commit dc69d0e9c3fe04ae9d67a782909f35a48f8a99cd

two possible outcomes to an encounter. If it does not result in a bound system, the stars or systems are returned to PH4. If the encounter results in a bound system, the stars are retained by MULTIPLES as a stable multiple and the centre of mass of the system is returned to the main N-body code. An additional criterion, aside from boundedness, is applied to the systems retained by MULTIPLES: the distance between the system’s centre of mass and the point on the orbit furthest from the centre of mass (i.e. the apocentre, as calculated by KEPLER) is less than 100 AU and either the perturbation criterion outlined in Equation 2.10 gives a value of at most 0.08 or the same pair of objects has been picked up by MULTIPLES for the 10<sup>th</sup> time. If a wide binary is not retained by MULTIPLES, it will be placed back in the N-body code at pericentre (i.e. closest approach). As long as a stable multiple is retained by MULTIPLES, its orbital motion does not influence the global timestep of the N-body code; in other words, the orbits of stable, unperturbed close binaries are considered frozen until a perturbation occurs. The treatment of multiples and encounters in TORCH thus follows the traditional Monte-Carlo approach: multiples are treated as unperturbed until they undergo a strong encounter with another star or multiple system. Portegies Zwart & McMillan (2019) argue that this approach is as accurate as the more computationally expensive approach to perturbations often adopted in N-body codes.

## **2.4 Early stellar feedback: winds & radiation**

As discussed in Section 1.2, numerous feedback channels participate in the regulation of star formation in embedded clusters, on different time and cluster mass scales. The suites of simulations presented in this work include a total initial gas mass of  $\sim 10^4 M_{\odot}$  and a final stellar mass of  $\sim 10^3 M_{\odot}$ , with clusters of radius  $\sim 1$  pc. In this regime, the most important feedback mechanisms are stellar winds, ionizing radiation and supernovae, all of which are implemented in TORCH. The details of their implementation are

presented in Wall et al. (2020). Protostellar jets and outflows may have a stronger impact on the small subclusters forming from individual sink particles, before they merge. A model for protostellar jets for TORCH is currently under construction (Appel et al., *in prep.*). TORCH (Wall et al. 2020) also includes a prescription for core-collapse supernovae, however none of our simulations have yet progressed far enough in time for a supernova.

*Far ultraviolet* (FUV, between 5.6 eV and 13.6 eV) and *ionizing* (above 13.6 eV) radiation is emitted by the star particles with masses above  $7 M_{\odot}$  (hereafter *massive stars*) in our simulations. The radiative feedback is implemented within FLASH as a modified (Wall et al. 2020) version of the adaptive ray-tracing module FERVENT (Baczynski et al. 2015). Ionizing radiation heats and ionizes the hydrogen gas. The photon counts and average energies, as well as the cross-sections and ionization fractions, are calculated for each star from the surface temperature and mass as evolved with SEBA (Portegies Zwart & Verbunt 1996). FUV radiation also heats the gas and injects momentum in the form of radiation pressure, which is an important contribution to the feedback from intermediate mass stars (e.g.  $7M_{\odot} \leq M_* \leq 13M_{\odot}$ , Wall et al. 2020). The injected momentum is calculated from the energy of the photons absorbed in each cell, divided by the speed of light. The details of the radiative feedback implemented in TORCH are presented in Wall et al. (2020).

All massive stars in our simulations also provide feedback in the form of momentum-driven winds. Numerous wind models have been used in the literature in simulations of star cluster formation. Winds can be folded into a generalized momentum feedback prescription alongside protostellar outflows and radiation (e.g. Li et al. 2019), as well as injected directly on the grid in the form of thermal energy (e.g. Rogers & Pittard 2013) or momentum (e.g. Haid et al. 2018). We use the momentum-conserving wind scheme developed by Wall et al. (2020), which is implemented directly in FLASH and allows for

mass injection on the grid. As shown in Wall et al. (2020), this model reproduces well the analytic solution for the expansion of a wind bubble in a uniform medium presented by Weaver et al. (1977). The mathematical expressions governing the changes in density and velocity in each cell within the injection volume of a wind-blowing star are outlined below, in Equation 2.11,

$$\rho = \rho_0 + \Delta\rho \quad (2.11a)$$

$$\vec{p} = \vec{v}_{inj}\Delta\rho + \vec{v}_0\rho_0 \quad (2.11b)$$

$$\vec{v} = \frac{\vec{p}}{\rho} = \frac{\vec{v}_{inj}\Delta\rho + \vec{v}_0\rho_0}{\rho_0 + \Delta\rho} \quad (2.11c)$$

where  $\rho_0$ ,  $\rho$  and  $\Delta\rho$  denote respectively the initial, final and injected densities;  $\vec{v}_0$ ,  $\vec{v}$  and  $\vec{v}_{inj}$  denote the initial, final and wind velocities, and  $\vec{p}$  denotes the final momentum. In Equation 2.11a, the injected density  $\Delta\rho$  is calculated from

$$\Delta\rho = \frac{\dot{M}\Delta t}{V_{inj}} \quad (2.12)$$

where  $\dot{M}$  is the star’s mass loss rate from Vink et al. (2000),  $\Delta t$  is the simulation’s timestep and  $V_{inj}$  is the cell volume overlapped by the star’s wind injection radius. The injection radius for each star is set by the numerical resolution.

The wind scheme described above was developed and implemented originally for single massive stars, however most massive, wind-blowing stars are in close binaries, which should dominate their evolution (Sana et al. 2012). We thus verify that our wind scheme properly reproduces the large-scale behaviour of colliding winds from massive stars. We present examples for an equal-mass system in Figure 2.1 and for a system with a mass ratio of  $\sim 1/3$  in Figure 2.2. Winds from different stars acting on the same cell are applied sequentially, which adequately reproduces the required vector addition. The equal-mass system gives rise to a shock at the symmetry interface. At the stagnation

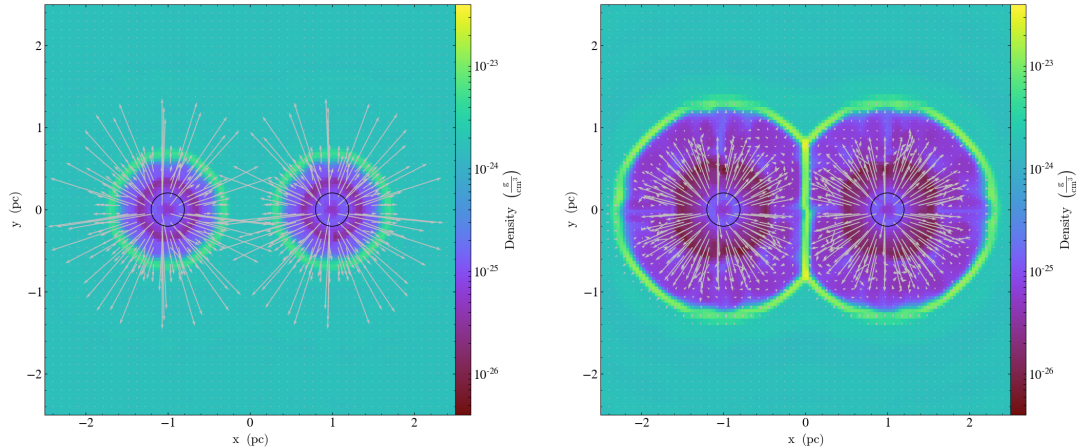


FIGURE 2.1: Density slices of the time evolution of the wind bubbles for two  $25 M_{\odot}$  stars formed at the same time, 5 kyr (left) and 15 kyr (right) after their formation, with overlaid velocity vectors. The black circles denote the wind injection radii. A shock forms at the interface between the two wind bubbles and the structure is symmetric about the shock front.

point (halfway between the stars), there is no net flow and the velocity is 0 (Stevens & Pollock 1994). The non-equal mass system is dominated by the most massive star, with a mass of  $70 M_{\odot}$ . This system shows indications of radiative braking (Gayley et al. 1997): the wind from the most massive star will be inhibited by the wind from the least massive  $25 M_{\odot}$  star. Although a detailed comparison between simulations of colliding-wind binaries and the behaviour of the O-star binaries in our simulations is beyond the scope of this thesis, we note that our wind model adequately handles winds from close pairs of massive stars.

It is less straightforward to compare our wind model to theoretical expectations in a non-uniform medium – and embedded clusters, with their dense and cold star-forming filaments and their sparse and hot HII regions, are highly non-uniform. We can nonetheless compare the wind model implemented in TORCH to recent models and simulations of stellar winds in star forming regions. Our simulations reproduce the general results from Lancaster et al. (2021a, 2021b): the wind bubbles develop highly asymmetrical

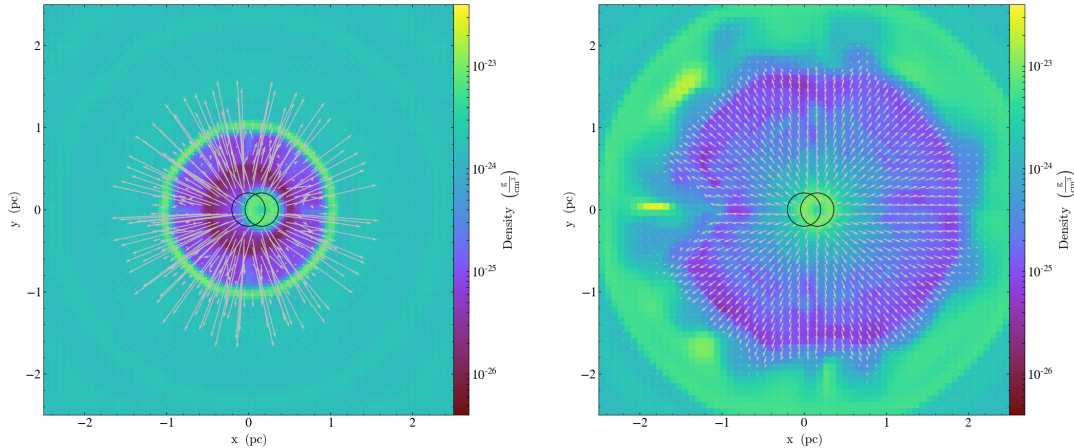


FIGURE 2.2: Density slices of the time evolution of the wind bubbles for a  $25 M_{\odot}$  and a  $70 M_{\odot}$  star formed with a time delay of 10 kyr before the formation of the most massive star, at the time of formation of the most massive star (left) and 10 kyr after (right). Velocity vectors are overlaid and the wind injection radii are denoted by black circles. After its formation, the most massive star dominates the evolution of the system. The presence of the other star results in a non-symmetric structure for the wind bubble.

geometry, which promotes effective radiative cooling at the bubble interface by increasing its area. Some caveats of our wind model are worth highlighting; combined, they suggest that the contribution of massive stars to momentum feedback in our simulations should be treated as an upper limit. First, the mass loss rates implemented by Wall et al. are those of Vink et al. (2000); more recent work (Smith 2014) suggest that these are overestimated by a factor of  $\sim 3$  because they do not take into account the clumpy nature of stellar winds. Second, the contributions of less massive stars to the feedback budget, in the form of protostellar jets and outflows, are ignored. Finally, mass transfer in binary systems is ignored, while binary interactions should dominate the evolution of the most massive stars in our simulations (Sana et al. 2012).

## 2.5 Multi-physics simulations and their challenges

State-of-the-art simulations of star cluster formation must include numerous physical processes, which we can break down here into four main categories, as discussed above: (1) hydrodynamics, (2) star and binary formation, (3) stellar dynamics and (4) stellar feedback. Hydrodynamics must be followed properly to account for the formation of filaments and the collapse of the gas, in order to accurately localize the regions in which star formation must take place. Modelling concurrently star formation and cluster-scale hydrodynamics is not feasible numerically, due to the many ( $\gtrsim 10$ ) orders of magnitude difference in scale between stars and GMCs. There is a wide variety of models for sub-grid star formation; we are interested in the ones that still allow the stars to form at locations consistent with the large-scale hydrodynamic behaviour of the forming cluster. These models generally do not include binaries. Many simulations of binaries in star-forming regions altogether ignore the presence of gas, while more complex and realistic simulations of cluster formation tend to ignore the presence of primordial binaries. Modelling both hydrodynamics and binary dynamics concurrently also has a large computational cost. We stress that no previous work has thus simultaneously included the four elements above – hydrodynamics, star and binary formation, stellar dynamics, stellar evolution – in a self-consistent way. Simulations of star-forming regions including feedback and simulations coupling hydrodynamics and stellar dynamics have nevertheless become more common in the last decade. We summarize here recent numerical work relevant to the interplay between binary and cluster formation.

Effective coupling of stellar dynamics and hydrodynamics, often also with stellar evolution, is possible within the AMUSE (Astrophysical MUlti-purpose Software Environment, Portegies Zwart & McMillan 2019) framework. In particular, the use of a gravity bridge (Fujii et al. 2007) allows the gas and stars to evolve in parallel, with different timesteps, while accurately modelling the gravitational attraction of one on

the other. Pelupessy & Portegies Zwart (2012) have conducted simulations of embedded clusters with 1000 stars, a few  $10^2 - 10^3 M_{\odot}$  of gas (modelled with *smoothed particles hydrodynamics*, SPH) and mechanical stellar feedback accounting for stellar winds and supernovae as predicted by stellar evolution schemes. Sills et al. (2018) use a similar scheme (albeit without stellar evolution) to model the dynamical evolution of embedded clusters initialized from initial conditions taken from observations. Neither of these simulations explicitly address star formation, however both use state-of-the-art N-body integrators. Gavagnin et al. (2017) use an AMR code coupled with star formation via sink particles, stellar dynamics and photoionizing feedback to investigate star cluster formation. Each sink particle formed in their simulation is treated as a star; stellar dynamics are handled by a second-order leapfrog scheme, less accurate than the fourth-order predictor-corrector scheme used in TORCH. Their simulations do not include momentum feedback, radiation pressure or any prescription for primordial binaries. Gavagnin et al. (2017) however track the dynamical formation of binaries and higher order systems, and find that the fraction of stable binaries tends to decrease with increasing stellar density, in line with observations (Milone et al. 2016; Duchêne et al. 2018).

Ballone et al. (2021) and Torniamenti et al. (2021) adopt a different approach to model gas and stars during cluster formation. They first consider pure hydrodynamical simulations, in which sink particles are allowed to form; after 3 Myr, they remove all the gas and rearrange the mass between sink particles by splitting and joining the sink particles, to sample a Chabrier (2003) IMF. They use the instantaneous removal of the gas as a proxy for supernova feedback, but include no radiative or momentum feedback. Torniamenti et al. (2021), in work published after the publication of Chapter 3 of this thesis, modified the joining–splitting algorithm described above to include a prescription for primordial binaries based on the field binary properties and similar to the ansatz we adopt here for our binary generation algorithm.

More complex feedback prescriptions are included in simulations of hierarchical star cluster formations within GMCs. Howard et al. (2016, 2017, 2018, 2019) show, in a seminal series of papers, that YMC (and GC) formation and the rise of multiple stellar populations within them is the natural extension of normal star cluster formation within the most massive GMCs. Their simulations include hydrodynamics handled by FLASH, active formation of subgrid stellar populations via sink particles and radiative feedback, in the form of direct radiation pressure and ionizing radiation. Li et al. (2019) conduct simulations of star cluster formation within GMCs including hydrodynamics, active formation of subgrid stellar populations via non-accreting star particles, and momentum stellar feedback as a proxy for stellar winds. They find that the SFR in their simulations increases linearly until it is halted by stellar feedback, leading to a superlinear growth of the stellar mass, consistent with observed dynamic SFRs in GMCs (Lee et al. 2016a). In a follow-up paper, Chen et al. (2021) find that GMCs with shallow density profiles give rise to hierarchical cluster assembly, in agreement with Howard et al. (2018), but that a single massive cluster is formed directly in GMCs with steep density profiles. Both suites of simulations include heating and cooling, and do not resolve stellar dynamics; they nonetheless provide very good models for radiative (Howard et al. 2018) and momentum (Li et al. 2019) feedback, that result in highly valuable insights into the process of cluster formation.

The first code to simultaneously resolve hydrodynamics, active star formation (albeit without primordial binaries), stellar dynamics and the effects of stellar evolution onto the surrounding gas via stellar feedback, is TORCH (Wall et al. 2019, 2020). TORCH uses FLASH to handle hydrodynamics (with magnetic fields), with radiative heating and cooling. Feedback prescriptions from stellar evolution models are also included, in the form of stellar winds, supernovae, direct radiation pressure and ionizing radiation. Stellar dynamics are handled by an accurate fourth-order predictor-corrector Hermite scheme, with an additional module to handle binary formation and disruption. Star

formation takes place via sink particles, from which stars are decoupled upon formation. Simulations conducted with TORCH give rise to gas behaviour as seen in state-of-the-art hydrodynamical simulations, in GMCs with masses  $10^3 - 10^5 M_{\odot}$  (e.g. formation of dense gas shells due to the effects of feedback, hierarchical cluster growth via motions along filaments, Wall et al. 2020) while also giving rise to stellar dynamics behaviour as seen in pure or direct N-body simulations (e.g. increase of binary fraction with mass, Wall et al. 2019).

Another multi-physics star cluster formation code has been developed in the wake of TORCH. STARFORGE (Guszejnov et al. 2021; Grudić et al. 2021) is also a magneto-hydrodynamics code including the same feedback mechanisms as TORCH, with the addition of protostellar outflows. Additionally, stars are formed from individual sink particles. The N-body integrator used in STARFORGE is however less accurate than that used in TORCH and, at this time, no prescription for primordial binaries is included in STARFORGE.

## CHAPTER 3

# IMPLEMENTING PRIMORDIAL BINARIES IN SIMULATIONS OF STAR CLUSTER FORMATION WITH A HYBRID MHD AND DIRECT N-BODY METHOD

### **Abstract**

The fraction of stars in binary systems within star clusters is important for their evolution, but what proportion of binaries form by dynamical processes after initial stellar accretion remains unknown. In previous work, we showed that dynamical interactions alone produced too few low-mass binaries compared to observations. We therefore implement an initial population of binaries in the coupled MHD and direct N-body star cluster formation code TORCH. We compare simulations with, and without, initial binary populations and follow the dynamical evolution of the binary population in both sets of simulations, finding that both dynamical formation and destruction of binaries take place. Even in the first few million years of star formation, we find that an initial population of binaries is needed at all masses to reproduce observed binary fractions for

binaries with mass ratios above the  $q \geq 0.1$  detection limit. Our simulations also indicate that dynamical interactions in the presence of gas during cluster formation modify the initial distributions towards binaries with smaller primary masses, larger mass ratios, smaller semi-major axes and larger eccentricities. Systems formed dynamically do not have the same properties as the initial systems, and systems formed dynamically in the presence of an initial population of binaries differ from those formed in simulations with single stars only. Dynamical interactions during the earliest stages of star cluster formation are important for determining the properties of binary star systems.

### **3.1 Introduction**

A complete picture of star cluster formation must account simultaneously for stars forming on the sub-AU scale, stellar dynamics taking place on the cluster's scale and gas flows at the scale of the surrounding giant molecular cloud. Even when star formation is resolved by a sub-grid model, as is most often the case in simulations, close dynamical encounters between stars must be resolved at the same time as star-gas interactions and large scale stellar dynamics. Effective numerical modelling of cluster formation must therefore be highly multi-scale. Despite these challenges, it is essential to address the problem of star cluster formation, as most stars are formed in a clustered environment (Lada & Lada 2003; Portegies Zwart et al. 2010).

Recent reviews of stellar multiplicity in the Galactic field (Duchêne & Kraus 2013; Moe & Di Stefano 2017) and of protostars embedded in gas (Reipurth et al. 2014) show that most stars, at all evolutionary stages, live in binaries or higher order systems. Surveys of low mass stars (e.g. Fischer & Marcy 1992; Reid & Gizis 1997; Delfosse et al. 2004; Winters et al. 2019), solar-type stars (e.g. Abt & Levy 1976; Duquennoy & Mayor 1991; Raghavan et al. 2010) and intermediate and high mass stars (e.g. Sana & Evans 2011; Sana et al. 2012; Chini et al. 2012) also reveal a correlation between multiplicity

and stellar mass. Both the fraction of stars in multiple systems and the average number of companions per primary increase with increasing primary mass: about 27% of low mass stars are in multiple systems (Delfosse et al. 2004; Winters et al. 2019), while multiplicity fraction is about 45% for solar-type (Raghavan et al. 2010) and A-type (De Rosa et al. 2014) stars, and is larger than 90% for high mass stars (Moe & Di Stefano 2017, and references therein).

Despite the ubiquity of binary systems, simulations of star cluster formation and dynamical evolution often use simplistic prescriptions for primordial binaries (i.e. binaries formed during star formation, e.g. Kroupa 1995; Sills & Bailyn 1999; Portegies Zwart et al. 2001; Leigh et al. 2013; Rastello et al. 2020) or ignore them altogether (e.g. Portegies Zwart et al. 1999; Pelupessy & Portegies Zwart 2012; Sills et al. 2018; Wall et al. 2019), primarily because primordial binaries remain poorly understood via either observations or simulations. Most observations of binaries in star forming regions (e.g. Kouwenhoven et al. 2005; Reipurth et al. 2007; King et al. 2012) are of visual binaries, with intermediate separation; binaries with smaller or larger separations are hard to observe. Nonetheless, a significant proportion of stars in star forming regions and in clusters are found in binary systems. Observations of stellar multiplicity in proto-stars indicate that binary fraction decreases with age, which is attributed to dynamical interactions between the stars (Tobin et al. 2016b).

Multiplicity is also influenced by environment. Binarity in globular clusters is anti-correlated with cluster luminosity (Milone et al. 2016), and binarity in open clusters is anti-correlated with cluster density (Duchêne et al. 1999). Young clusters have field-like binary fractions (Duchêne et al. 1999; Duchêne et al. 2018; Sana & Evans 2011), and there is no clear difference between the distributions of periods, mass ratios and eccentricities in the field and in young clusters for massive stars (Sana & Evans 2011). Conversely, loose stellar associations have binary fractions higher than in the field (Duchêne et al.

1999; Duchêne et al. 2018). The presence of binary systems in star clusters influences their dynamical evolution, for example by facilitating evaporation. Binaries with low binding energy are disrupted, while energetic binaries become more tightly bound and transfer kinetic energy to the cluster, thus accelerating its dissolution (e.g. Heggie 1975; Hills 1975). Appropriate choices of sub-grid model for binary formation and binary parameters – such as the separation or mass ratio of the generated systems – are therefore also required for realistic star cluster formation simulations.

The fact that binary systems can be both formed (e.g. Kouwenhoven et al. 2010; Parker & Meyer 2014) and destroyed (e.g. Parker et al. 2009; Parker & Goodwin 2012) by the evolution of young clusters further complicates the problem. Although a reasonable assumption would be that some separations (and hence some periods) are associated with primordial formation and others with dynamical formation, it is not so simple. Simulations (e.g. Offner et al. 2010; Sigalotti et al. 2018) and observations (e.g. Tobin et al. 2016a; Lee et al. 2017) show that turbulent core fragmentation and disk fragmentation are viable mechanisms to form binaries during star formation, with separations up to  $\sim 1000$  AU. Simulations have also shown that binaries with semi-major axes between 1000 AU and 0.1 pc can be formed during the dissolution of young star clusters (Kouwenhoven et al. 2010). Tokovinin (2017) argues that binaries with such separations are more prevalent than what would be predicted by dynamical interactions alone, and proposes that stars forming in adjacent cores could be bound as primordial binaries. Conversely, dynamical interactions in a young cluster can also form binaries with separations well below 1000 AU (e.g. Parker & Meyer 2014; Wall et al. 2019).

We develop a new binary generation algorithm consistent with observations of mass dependent binary fraction and distributions of orbital periods, mass ratios and eccentricities. As an ansatz, we use the observed distribution of zero-age main sequence binary systems in the Galactic field to generate our population. Our choice is motivated by

the quality of the observations for this population and by the simulations conducted by Parker & Meyer (2014): with pure N-body simulations of star forming regions, they find that using the distributions of binary fraction, mass ratio and period in the field as initial conditions can reproduce the field distribution after dynamical evolution. Our distributions can however be readily modified to investigate different primordial binary distributions. We use the star cluster formation code TORCH (Wall et al. 2019) to demonstrate the impacts of our new binary generation algorithm on the earliest stages of star cluster formation, up to the formation of the first massive stars.

In Section 3.2, we describe our simulation environment and our binary generation algorithm. In Section 3.3, we present our suite of simulations. In Section 3.4, we compare the properties of binary systems in the simulations including primordial binaries and in those starting with only single stars. We summarize our results and discuss their implications in Section 3.5.

## **3.2 Methods**

### **3.2.1 Simulating cluster formation with Torch**

TORCH<sup>1</sup> uses the AMUSE framework (Portegies Zwart & McMillan 2019) to couple self-gravitating, magnetized gas modelled by the magnetohydrodynamics (MHD) adaptive mesh refinement (AMR) code FLASH (Fryxell et al. 2000) with the N-body code ph4 (McMillan et al. 2012) and the stellar evolution code SEBA (Portegies Zwart & Verbunt 1996). We use FLASH with a Harten–Lax–van Leer Riemann solver resolving discontinuities (HLLD, Miyoshi & Kusano 2005) and an unsplit MHD solver (Lee 2013) with third order piecewise parabolic method (PPM) reconstruction (Colella & Woodward 1984) for gas dynamics, and a multigrid solver for gravity (Ricker 2008). We handle the gravitational effects of the gas and the stars on one another by a leapfrog integration

---

<sup>1</sup><https://bitbucket.org/torch-sf/torch/branch/binaries>  
commit 28a27574f667e8a580fe964f5ff185d4fb63f1e7

between the two systems (see Wall et al. 2019). Similar gravity bridges have been used previously to couple direct N-body codes with smoothed particle hydrodynamics (SPH) codes (e.g. Pelupessy & Portegies Zwart 2012; Sills et al. 2018) and with the AMR code RAMSES (Gavagnin et al. 2017).

TORCH is also optimized to deal with multiple stellar systems. Resolving repeated close encounters between the members of a stable, unperturbed system (e.g. a binary or a hierarchical triple) with the N-body integrator prohibitively shortens the timestep. For each binary or higher order system deemed stable by the Mardling criterion (Mardling 2008, by which triples can have at most one orbital resonance to avoid instability due to large energy exchanges between the orbits), we use MULTIPLES (Portegies Zwart & McMillan 2019), which replaces the stars by the systems' centres of mass in PH4. The internal configuration of the system is saved, and the positions of the stars within the system are only computed if the system is perturbed. The encounter between the system and the perturbing star is then resolved with the few-body solver SMALLN (Hut et al. 1995; McMillan & Hut 1996).

Star formation is handled by a sub-grid model via sink particles, which are formed in regions of high local gas density and converging flows, following Jeans' criterion and the additional conditions detailed in Federrath et al. (2010). When a sink forms, we use Poisson sampling to generate a list of stars it will form by drawing stellar masses from a Kroupa 2001 initial mass function (IMF, Sormani et al. 2017; Wall et al. 2019), with a minimum sampling mass of  $0.08 M_{\odot}$  and a maximum sampling mass of  $150 M_{\odot}$ . We randomize the list of stars; each star is then formed in order when the sink has accreted sufficient mass. Once it is formed, the sink follows the location of the centre of mass of the local stars and gas, and continues accreting gas.

TORCH also includes stellar feedback, heating and cooling, which are handled via sub-grid models. The amount and location of the feedback depends on the evolution

(via SEBA) of the specific stars formed in the simulation. It uses the FLASH module FERVENT (Baczynski et al. 2015) for photoionization, direct ultra-violet (UV) radiation pressure from massive stars and photoelectric heating from far-UV radiation. It uses the method of Wall et al. (2020) for stellar winds, and does not include either indirect radiation pressure or protostellar outflows.

### **3.2.2 Binary generation algorithm**

We want to generate a final stellar population that is consistent with the observed IMF, and that also ultimately reproduces the observed binary properties after cluster interactions. However, the effects of the cluster interactions on the primordial binary population are still poorly understood, and observations are not sufficient to have a complete and accurate picture of the properties of binary systems at birth. Nonetheless, observations (e.g. Sana & Evans 2011) and simulations (e.g. Parker & Meyer 2014) suggest that the multiplicity fraction and period, mass ratio and eccentricity distributions in young clusters are consistent with the field population. Volume-limited observations of binary systems in the galactic field, for systems with mass ratios  $M_2/M_1 \geq 0.1$ , are complete for a very large range of orbital periods (Moe & Di Stefano 2017; Winters et al. 2019). They are also obtained from much larger samples than observations of young clusters. We therefore adopt for our first suite of simulations a population of primordial binaries with mass-dependent binary fraction and properties consistent with observations of zero-age main sequence stars in binary systems in the Galactic field. Our framework can also be adapted to explore other primordial binary populations.

#### **Mass-dependent binary fraction**

For simplicity, and following previous studies of binary population synthesis (e.g. Kroupa 2001; Kouwenhoven et al. 2009; Parker & Meyer 2014), we do not form any triple or quadruple systems primordially. These are known to be ubiquitous for B and O-type

primaries (e.g. Sana et al. 2012; Moe & Di Stefano 2015), but represent only 3% of systems for M-dwarfs (Winters et al. 2019) and 10% of systems for solar-type stars (Moe & Di Stefano 2017), which account together for  $> 90\%$  of main-sequence stars (Kroupa 2001). We treat the mass dependent multiplicity fraction as a mass dependent binary fraction, in order to include all systems included in studies of stellar multiplicity. Since it is hard to determine observationally if there are any unresolved components to a system, most reviews of stellar multiplicity make no distinction among binaries, triples and higher order systems in their distributions of multiplicity fraction, period, mass ratio and eccentricity. We hence implement a mass dependent binary fraction, which reflects observed distributions of multiplicity fraction.

For each list of stellar masses obtained at the formation of a sink, we treat each star as a potential primary, and use the primary mass dependent binary fraction to determine if the star is in a binary system. Single stars and primaries are therefore drawn directly from the IMF, while companions are drawn from mass ratio distributions. For each potential primary, we use a random number generator to obtain a number between 0 and 1; the star is found to be in a binary system if the random number is below the mass dependent multiplicity fraction. After a large number of draws, the binary fraction approaches the prescribed multiplicity fraction.

For low-mass stars, we use the observed multiplicity fraction of M-dwarfs in the solar neighbourhood, for primary masses in the mass bins  $0.08 - 0.15 M_{\odot}$ ,  $0.15 - 0.30 M_{\odot}$  and  $0.30 - 0.60 M_{\odot}$  (Winters et al. 2019). For solar-type stars and above, we use the observed multiplicity fractions for primary masses  $0.8 - 1.2 M_{\odot}$ ,  $2 - 5 M_{\odot}$ ,  $5 - 9 M_{\odot}$ ,  $9 - 16 M_{\odot}$  and above  $16 M_{\odot}$  (Moe & Di Stefano 2017). Between  $0.6 M_{\odot}$  and  $0.8 M_{\odot}$ , and between  $1.2 M_{\odot}$  and  $2 M_{\odot}$ , we interpolate linearly between the observed multiplicity fractions. We summarize the multiplicity fractions in Tables 3.1 and 3.2.

TABLE 3.1: Multiplicity properties from Winters et al. (2019).  $M_1$  is the primary mass,  $\mathcal{F}$  is the binary fraction,  $\mu_a$  is the mean projected separation around which the lognormal probability distribution is centered,  $\mu_P$  (days) is the corresponding period in days (assuming a circular orbit) and  $\log \sigma_P$  is the standard deviation of the lognormal distribution. With the exception of the binary fraction and the period, all the other properties for systems with  $M_1 \leq 0.60 M_\odot$  are obtained from the same distributions as systems with  $M_1 \sim 1 M_\odot$  (see Table 3.2, top row).

$M_1$	$\mathcal{F}$	$\mu_a$ (AU)	$\mu_P$ (days)	$\log \sigma_P$
0.08 – 0.15 $M_\odot$	0.16	7	$10^{3.83}$	4.12
0.15 – 0.30 $M_\odot$	0.21	11	$10^{4.12}$	4.37
0.30 – 0.60 $M_\odot$	0.28	49	$10^{5.10}$	4.78

TABLE 3.2: Multiplicity properties from Moe & Di Stefano (2017).  $M_1$  is the primary mass,  $\mathcal{F}$  is the binary fraction,  $P$  is the period range,  $\mathcal{F}_P$  is the relative probability for a system to have a period in a given range;  $\gamma_{\geq 0.3}$  is the power-law exponent of the mass ratio distribution for  $q \geq 0.3$  and  $\gamma_{< 0.3}$  is the power-law exponent of the mass ratio distribution for  $q < 0.3$ .

$M_1$	$\mathcal{F}$	$P$ (days)	$\mathcal{F}_P$	$\gamma_{\geq 0.3}$	$\gamma_{< 0.3}$
0.8 – 1.2 $M_\odot$	0.40	$10^{0.5-1.5}$	0.06	-0.5	0.3
		$10^{2.5-3.5}$	0.13	-0.5	0.3
		$10^{4.5-5.5}$	0.22	-0.5	0.3
		$10^{6.5-7.5}$	0.17	-1.1	0.3
2 – 5 $M_\odot$	0.59	$10^{0.5-1.5}$	0.10	-0.5	0.2
		$10^{2.5-3.5}$	0.16	-0.9	0.1
		$10^{4.5-5.5}$	0.18	-1.4	-0.5
		$10^{6.5-7.5}$	0.12	-2.0	-1.0
5 – 9 $M_\odot$	0.76	$10^{0.5-1.5}$	0.11	-0.5	0.1
		$10^{2.5-3.5}$	0.18	-1.7	-0.2
		$10^{4.5-5.5}$	0.16	-2.0	-1.2
		$10^{6.5-7.5}$	0.09	-2.0	-1.5
9 – 16 $M_\odot$	0.84	$10^{0.5-1.5}$	0.13	-0.5	0.1
		$10^{2.5-3.5}$	0.17	-1.7	-0.2
		$10^{4.5-5.5}$	0.15	-2.0	-1.2
		$10^{6.5-7.5}$	0.09	-2.0	-2.0
$\geq 16 M_\odot$	0.94	$10^{0.5-1.5}$	0.14	-0.5	0.1
		$10^{2.5-3.5}$	0.16	-1.7	-0.2
		$10^{4.5-5.5}$	0.15	-2.0	-1.2
		$10^{6.5-7.5}$	0.09	-2.0	-2.0

### **Period distribution**

Periods also depend on primary mass. For each primary, we obtain the orbital period by drawing it from the chosen probability distribution for the corresponding mass range, sampled with the rejection method (Von Neumann 1951). For each primary, we pick a pair of random numbers – here, a period between  $10^{0.5}$  and  $10^{7.5}$  days and a number between 0 and the maximum value of our probability distribution surface – and accept the pair if the point it defines in parameter space lies below our probability distribution. If it lies above our probability distribution, we reject the pair and repeat the algorithm until a pair is accepted (following the algorithm from Press et al. 2007, §7.3.6). For primary masses below  $0.60 M_{\odot}$ , we use the lognormal distributions from Winters et al. (2019), which are given for each of the primary mass bins discussed above. For each primary mass range, Moe & Di Stefano (2017) give probabilities at different period values; we extend each given value over one order of magnitude in period (in days), then linearly interpolate between two different period ranges. We use the same mass bins as defined above, but extend the  $0.8 - 1.2 M_{\odot}$  range down to  $0.6 M_{\odot}$  and up to  $1.6 M_{\odot}$ , while we extend the  $2 - 5 M_{\odot}$  range down to  $1.6 M_{\odot}$ . We therefore have a probability distribution depending on both primary mass and period.

### **Companion mass distribution**

We obtain the companion masses from distributions of mass ratios  $q = M_2/M_1$ , where  $M_1$  is the primary mass,  $M_2$  is the companion mass and  $q \leq 1$  by definition. Kouwenhoven et al. (2009), in a review of binary pairing functions, summarize as follows the different possible ways to assemble a binary system:

1. *Random pairing* Two stars are independently drawn from the IMF; the most massive is labelled as the primary. Random pairing of stars from the Kroupa IMF results in a uniform distribution of system masses (Kroupa 2001), which Kouwenhoven et al. (2009) find to result in mass ratios inconsistent with observations.

2. *Primary-constrained random pairing* The primary is drawn randomly from the IMF; the companion is then also drawn from the IMF, but with the constraint that it must be less massive than the primary. This pairing function does not reproduce observed mass ratios either (Kouwenhoven et al. 2009).
3. *Primary-constrained pairing* The primary is drawn randomly from the IMF; the companion is then drawn from the mass ratio probability distribution. This technique is meant to be used with a stellar IMF (e.g. Kroupa 2001). It is compatible with observations, and allows for the use of a primary mass dependent mass ratio distribution, which is observed in nature.
4. *Split-core pairing* The system mass is drawn randomly from a distribution of system or core masses, then fragmented as a mass ratio is drawn from an observed probability distribution. This technique is meant to be used with a system initial mass function (e.g. Chabrier 2003). It is also compatible with observations.

Both primary-constrained pairing (iii) and split-core pairing (iv) can reproduce observations of stellar masses and mass ratios concurrently, as well as of a mass dependent binary fraction. They require different pieces of information to implement. Primary-constrained pairing requires a distribution of stellar masses, and primary mass dependent binary properties; split-core pairing requires a distribution of system masses, and can be implemented with primary mass dependent binary properties. We choose to assemble the binary systems with primary-constrained pairing, by drawing primary masses from a Kroupa (2001) IMF then obtaining the companion masses from the observed primary mass and period-dependent mass ratio distributions. TORCH uses by default the Kroupa (2001) initial mass function, and it is the initial mass function that was used in the original suite of simulations (Wall et al. 2019; Wall et al. 2020). We use the same initial mass function for ease of comparison and consistency.

We use the probability distributions from Moe & Di Stefano (2017), which we extend to lower masses. The mass ratio probability distributions are modelled as power laws,

$$p_q \propto q^\gamma \tag{3.1}$$

where the exponent  $\gamma$  is a function of the mass ratio range, the primary mass and the orbital period. We consider three primary mass ranges,  $0.08 - 2 M_\odot$ ,  $2 - 5 M_\odot$  and above  $5 M_\odot$ ; the first mass range is extended from the  $0.8 - 1.2 M_\odot$  range provided by Moe & Di Stefano (2017) since Winters et al. (2019) admit that their results are likely incomplete at low companion masses. For each of these mass ranges, we consider a broken power law, with  $\gamma$  defined for mass ratios between 0.1 and 0.3, and above 0.3. Finally, the probability is given at different values of the period, between which we interpolate with the same technique as for the period probability distribution. From there, we use the rejection method to obtain a mass ratio.

We reject mass ratios that would result in substellar companions. We also note that observations are unreliable below  $q \leq 0.1$  (Duchêne & Kraus 2013; Moe & Di Stefano 2017; Winters et al. 2019). Price-Whelan et al. (2020), in their analysis of 20,000 close binary systems, acknowledge that their observations are incomplete at low mass ratios. At the high mass end, the problem is most prevalent for spectroscopic searches at intermediate separations (Kobulnicky et al. 2014). In open clusters, Sana & Evans (2011) are only confident in their observations for  $q \geq 0.2$  for massive binaries, while Deacon & Kraus (2020) are unable to detect companions with  $q \leq 0.1$  and estimate that they detect only  $\sim 50\%$  of systems with  $q = 0.3$  in their surveys of wide binaries in Alpha Per, the Pleiades and Praesepe. Following the completeness limit of Moe & Di Stefano (2017) and Winters et al. (2019), we therefore also reject mass ratios below  $q = 0.1$ .

### **Eccentricity distribution**

The eccentricity probability distribution is similarly modelled as a broken power law, as a function of primary mass and period,

$$p_e \propto e^\eta \tag{3.2}$$

where  $\eta = 1$  would result in a thermal distribution and  $\eta = 0$  would result in a uniform distribution. Following Moe & Di Stefano (2017), we define

$$\eta = 0.6 - \frac{0.7}{(\log(P/\text{days}) - 0.5)} \tag{3.3}$$

for primary masses up to  $5 M_\odot$ , while for primary masses above  $5 M_\odot$ , we define

$$\eta = 0.9 - \frac{0.2}{(\log(P/\text{days}) - 0.5)}. \tag{3.4}$$

We further define a period-dependent upper limit on the eccentricity, to avoid binary systems with filled Roche lobes. We use the analytic form of the maximum eccentricity from Moe & Di Stefano 2017,

$$e_{max}(P) = 1 - \left( \frac{P}{2 \text{ days}} \right)^{-2/3} \tag{3.5}$$

which is defined for orbital periods longer than 2 days; we assume all binary systems with shorter periods are circularized (Raghavan et al. 2010). We use the rejection method to obtain the eccentricities.

### **Algorithm test**

We test our algorithm by generating a list of stars starting from an initial mass function normalized to  $10,000 M_\odot$  and our ansatz of observed field binary properties. We then

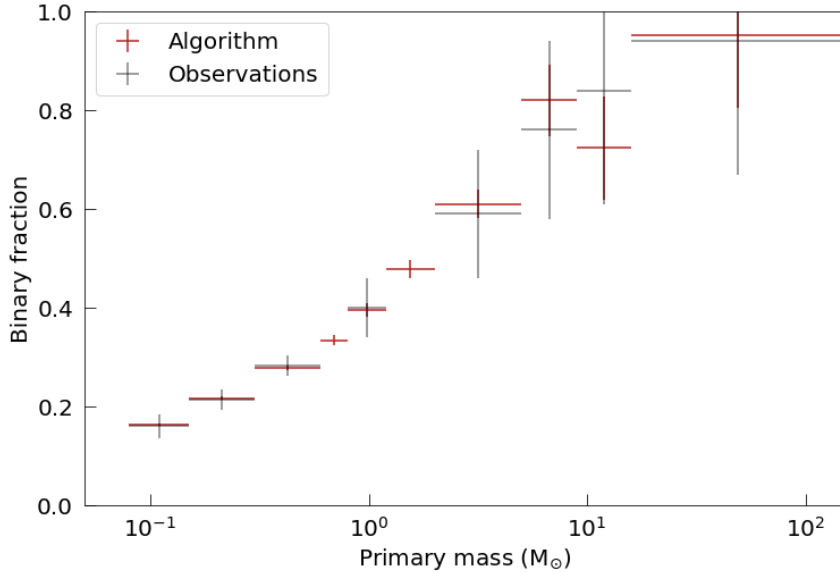


FIGURE 3.1: Mass dependent binary fraction, for main sequence stars in the solar neighbourhood (Moe & Di Stefano 2017; Winters et al. 2019) and for our binary generation algorithm. The errors in  $x$  correspond to the bin widths; the errors in  $y$  in the observations are from the observational uncertainties while the errors in  $y$  on the algorithm data are from the Poisson statistical error.

apply our algorithm to determine which stars are in binary systems; we obtain the period, companion mass and eccentricity for each binary system. We verify that our algorithm indeed reproduces the mass dependent binary fraction observed in the galactic field (Figure 3.1) and compare our full stellar mass distribution to the initial mass function (Figure 3.2). We also consider our distributions in the primary mass vs. mass ratio parameter space (Figure 3.3). We generate no systems with a mass ratio  $q < 0.1$  and form no stars with a mass below the hydrogen burning limit.

### 3.2.3 Implementing primordial binaries in Torch

To place a star within the simulation, it must be the next star in the list of stars to be formed by a sink particle, and the sink must have accreted a gas mass equal to or greater than the star’s mass. When a star is formed, its mass is subtracted from the

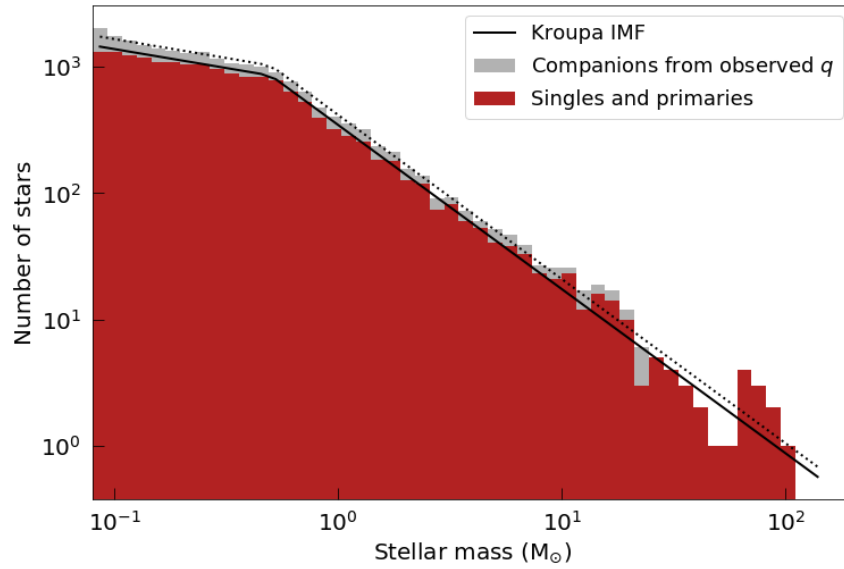


FIGURE 3.2: Distribution of stellar masses, for the single stars and primaries drawn from the Kroupa initial mass function (red) and the companions obtained from the mass ratio probability distribution (grey). The Kroupa initial mass function normalized to  $10,000 M_{\odot}$  (solid line) and to the total stellar mass (dotted line) is provided as a guide for the eye.

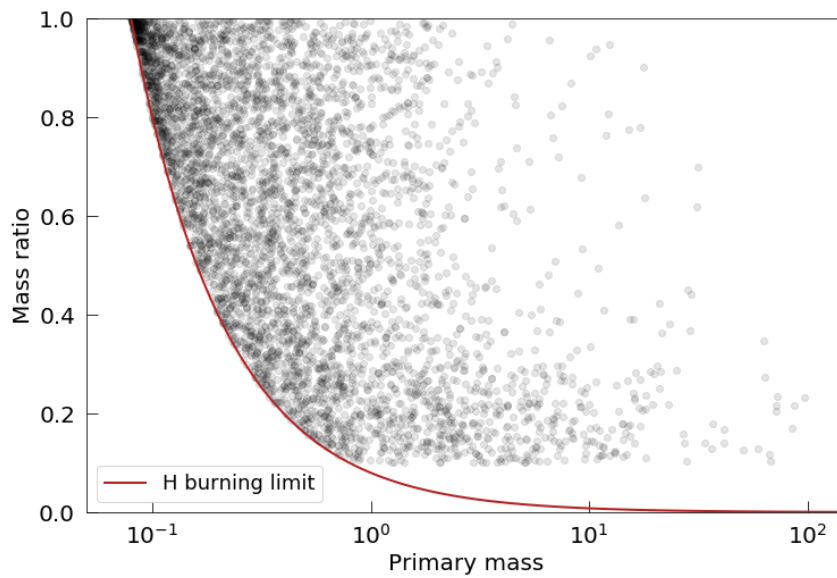


FIGURE 3.3: Distribution of mass ratios against primary masses. Our algorithm restricts mass ratios to be higher than 0.1, as observations are highly incomplete below this value. The red line denotes the companion mass corresponding to the hydrogen-burning limit; note that no substellar companions are generated.

sink mass. The star thus formed can be located within the sink’s accretion radius, but will be treated by the simulation as a particle distinct from the sink. The local gas temperature must be below 100 K at the time of star formation; if the gas temperature is higher, star formation is delayed. Assuming primordial binaries formed through disk or core fragmentation would become stars at the same time, we ensure that stars formed in a binary system are formed at the same time in the simulation. We therefore modify the condition for star formation to require that the mass of a system (whether a single star or a binary) must be accreted by the sink particle before either star is formed. This additional mechanism does not modify the routine to form single stars, but ensures that primaries and their companions are formed simultaneously in the simulation.

The binary systems we generate with our algorithm must be introduced in the simulation with positions and velocities consistent with their orbital properties. We randomize the orbit’s orientation by randomizing the inclination, longitude of the ascending node and argument of periapsis, and obtain the relative positions and velocities of the stars by picking a random time in the orbit. The locations of the binaries’ centres of mass are chosen in the same way as single stars’ positions in TORCH (Wall et al. 2019). The position of each star within the simulation domain is finally obtained by adding together the position of the sink in which it forms, the position vector of the centre of mass of the system relative to the sink, and the position vector of the star relative to its system’s centre of mass. For binaries with long periods or very eccentric orbits, a star can be formed outside the sink if required by their orbital parameters. Single stars inherit the velocity of the sink at the time of formation, plus a random fraction of the local sound speed (Wall et al. 2019). We adopt this prescription for the systems’ centres of mass. For stars in a binary system, their velocity is obtained from the addition of the sink’s velocity, the random component from the local sound speed, and the velocity with respect to the centre of mass velocity.

### 3.3 Simulations

Initial tests of TORCH (Wall et al. 2019; Wall et al. 2020) have shown that the time evolution of the star formation rate and the spatial distribution of star formation are highly stochastic, and depend strongly on the initial conditions. We therefore adopt a single set of initial conditions for our full suite of simulations, to investigate solely the impact that the presence or absence of primordial binaries has on the final distributions of binaries. We initialize all our simulations from the same spherical cloud of dense neutral gas with a mass of  $10^4 M_{\odot}$ , a virial parameter of 0.4, a radius of 7 pc and a Gaussian density profile with central density  $8.73 \times 10^{-22} \text{ g/cm}^3$ . The initial cloud has a central temperature of 20.64 K and sits in a medium of warm neutral gas with a temperature of  $6.11 \times 10^3 \text{ K}$  and a density of  $2.18 \times 10^{-22} \text{ g/cm}^3$ . Each simulation uses the same initial turbulent Kolmogorov velocity spectrum but a different random seed for the stellar masses. There is no initial magnetic field. The gas follows an adiabatic equation of state with  $\gamma = 5/3$ . The simulations include atomic, molecular and dust cooling, as well as ionization, following Wall et al. (2020).

Galactic effects are ignored, as the clusters are evolved for  $t \lesssim 3.2 \text{ Myr}$ . Tidal perturbations or disk crossing effects are unlikely to have an impact on the cluster's structure on such a timescale (e.g. Kruijssen et al. 2011; Miholics et al. 2017). The size of the simulation box ( $\sim 18 \text{ pc}$ ) is large enough to ensure the choice of boundary conditions does not have a strong impact on the outcome of the simulation: observed star clusters in nearby galaxies with the same stellar mass as our simulations have half-mass radii one order of magnitude smaller than the box size (Krumholz et al. 2019, and references therein). We use zero-gradient boundary conditions, which allow the gas and stars to leave the domain. The choice of spatial resolution ( $\sim 0.05 \text{ pc}$ ) is appropriate to model the gas dynamics in the cluster, excluding star formation which is treated by a sub-grid model. The resolution is approximately one order of magnitude smaller

than the average separation between stars in dense clusters (Krumholz et al. 2019, and references therein) and thus resolves well the behaviour of the gas between the stars.

We perform a total of 15 simulations, at two different maximum FLASH refinement levels. At our lowest refinement level, we perform five simulations with primordial binaries and five without primordial binaries; at our highest refinement level, we perform four simulations with primordial binaries and one simulation without primordial binaries. The least resolved regions in all our simulations are at refinement level 4 and have a gas spatial resolution of 0.136 pc. The spatial and mass resolutions of our simulations are presented in Table 3.3. In our analysis, we use the combined results of groups of simulations to ensure we have a large population of systems to analyze. We will use the variation between simulations to quantify the uncertainty in our results and the numerical effects of resolution. We denote our suites of simulations with primordial binaries at refinement levels 5 and 6 as respectively **M4r5b** and **M4r6b**, and our suite of simulations without primordial binaries at refinement level 5 as **M4r5s**. We refer to our full suites of simulations at refinement levels 5 and 6 as respectively **M4r5** and **M4r6**; similarly, we refer to our full suite of simulations with primordial binaries as **M4b** and to our full suite of simulations without primordial binaries as **M4s**. We perform our analysis with 9866 stars in **M4r5b**, 9016 stars in **M4r5s**, 6384 stars in **M4r6b** and 1517 stars in **M4r6s**. We plot the results from **M4r5**, as this suite of simulations has the most stars.

We summarize the time of onset of star formation, the time at which the simulation is ended, the maximum stellar mass, the number of stars and the total stellar mass for each of our simulations in Table 3.4. Since the only difference between the different simulations at the same resolution is in the stellar sampling, star formation starts at the same time and the first sink forms at the same location for all simulations at the same resolution. We present two examples of the time evolution of the star formation rate in Figure 3.4. In Figure 3.5, we present the projected density for nine simulations,

TABLE 3.3: Spatial and mass resolution, at maximum refinement level *ref*.  $\Delta x$  denotes the minimum zone size while  $\Delta m$  and  $\rho_c$  denote respectively the maximum mass and the maximum density in a grid cell to trigger sink formation, assuming a sound speed  $c_s = 1.9 \times 10^4 \text{ cm s}^{-1}$  (following Federrath et al. 2010)

<i>ref</i>	$\Delta x$ (pc)	<i>Sink diameter</i> (AU)	$\Delta m$ ( $M_\odot$ )	$\rho_c$ ( $\text{g cm}^{-3}$ )
5	$6.83 \times 10^{-2}$	$7.05 \times 10^4$	$1.80 \times 10^{-2}$	$3.82 \times 10^{-21}$
6	$3.42 \times 10^{-2}$	$3.53 \times 10^4$	$9.00 \times 10^{-3}$	$1.53 \times 10^{-20}$

a minimum of  $\sim 1.5$  Myr after the onset of star formation. We note that the general structure of the gas and the sink locations are very similar in all simulations, as expected since all the simulations start from the same initial gas conditions. Nevertheless, the number of stars and their locations, as well as the total stellar mass, differ among the simulations. At similar times, there are spreads of 18% in number of stars and 24% in stellar mass. Our simulations end at 1.5 – 2 Myr after the start of star formation, at the time when feedback from massive stars starts to have a significant impact on the gas properties. Therefore, our simulations probe the earliest stages of star cluster formation, when the dominant physical effects are gas collapse and star formation, combined with dynamical interactions between stars, binary systems, and their natal gas.

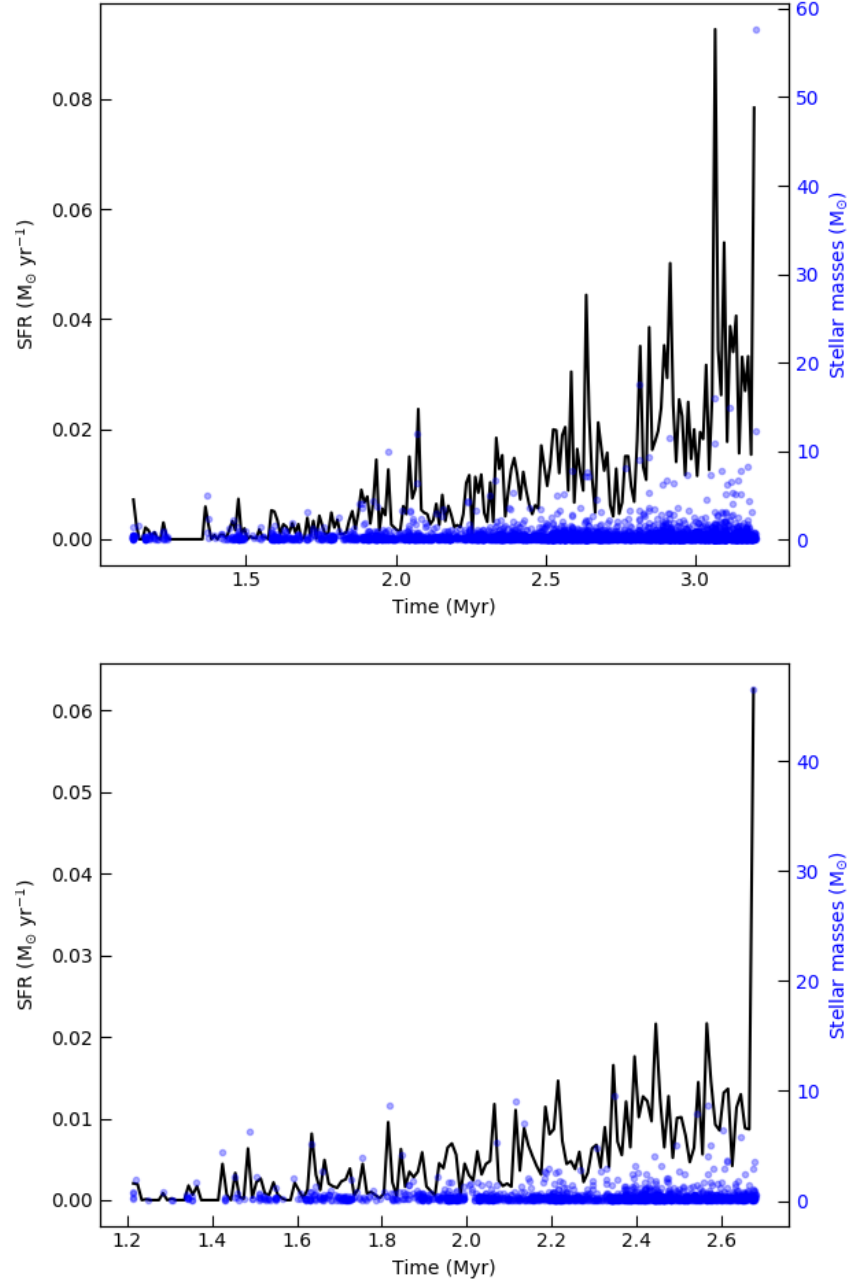


FIGURE 3.4: Star formation rates for M4r5b-4 (top) and M4r6s (bottom). The solid black line shows the rate smoothed over 1 kyr (left axis) and the blue points shows the masses of the individual stars formed in the simulation (right axis). The total stellar masses are respectively  $2.14 \times 10^3 M_{\odot}$  and  $7.60 \times 10^2 M_{\odot}$  for M4r5b-4 and M4r6s. Peaks in star formation rate coincide with the formation of massive stars, and there is an overall increase of the star formation rate as the simulation progresses.

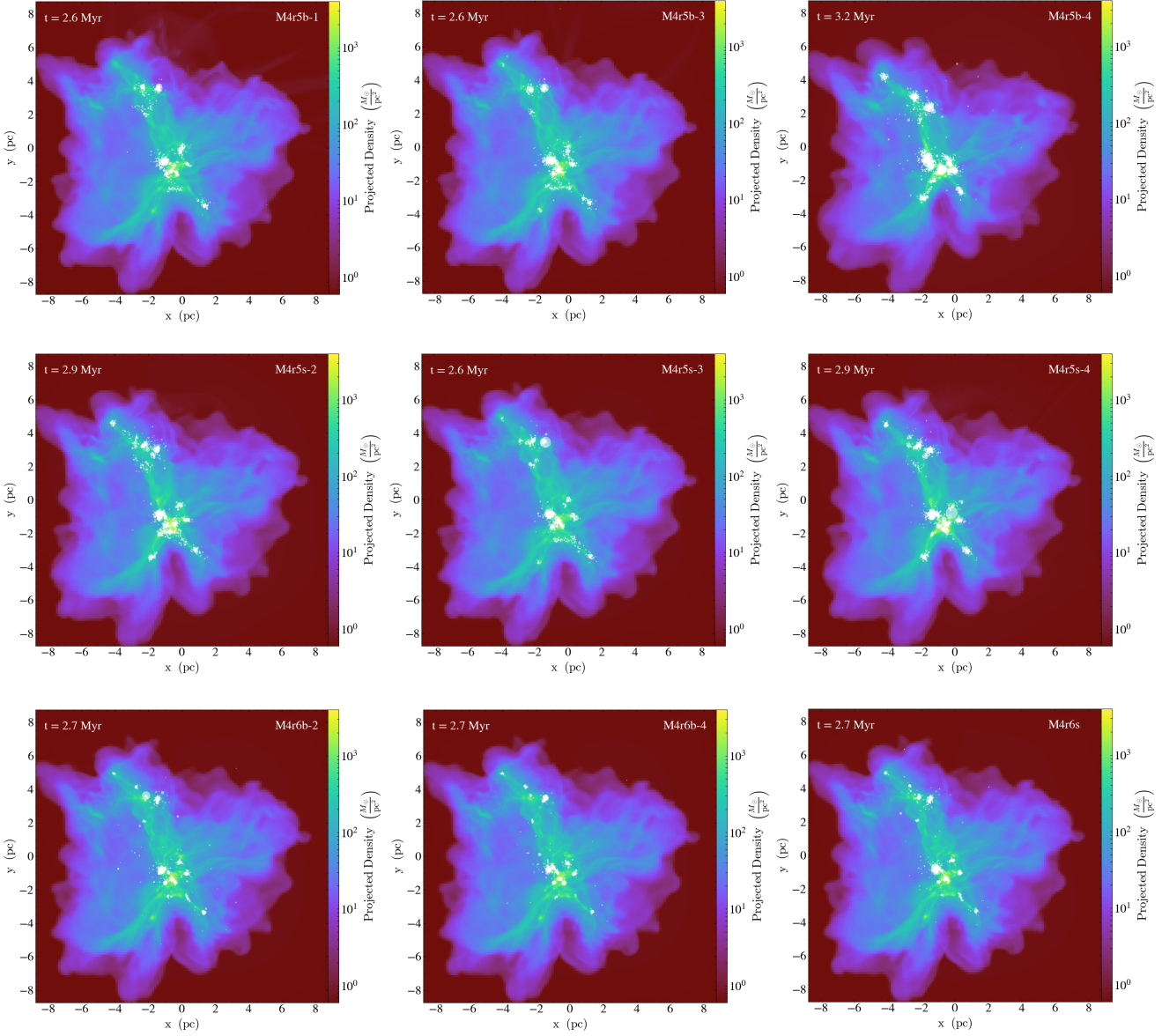


FIGURE 3.5: Final projected density distribution in the simulations (from top left to bottom right) M4r5b-1, M4r5b-3, M4r5b-4, M4r5s-2, M4r5s-3, M4r5s-4, M4r6b-2, M4r6b-4 and M4r6s. The white circles are the full sample of stars in the simulations; the radius of the circle is proportional to the stellar mass. All simulations use the same initial conditions, which is reflected by the very similar gas configurations. We note however differences in the locations and masses of the stars, and expect to see these differences reflected in the gas configuration once feedback becomes more important. The total stellar mass and number of stars for each simulation can be found in Table 3.4.

TABLE 3.4: Simulations. All simulations have a total gas mass  $10^4 M_{\odot}$  and a minimum refinement of 4. The number after **r** denotes the maximum refinement level and the last letter indicates if the simulation includes primordial binaries (**b**) or single stars only (**s**).  $t_*$  denotes the time of the onset of star formation and  $t$  denotes the time at which the simulation has ended;  $M_m$  denotes the mass of the most massive star,  $N_*$  is the number of stars in the simulation, and  $M_*$  is the total stellar mass.

<i>Name</i>	$t_*$ (Myr)	$t$ (Myr)	$M_m$ ( $M_{\odot}$ )	$N_*$	$M_*$ ( $M_{\odot}$ )
M4r5b-1	1.12	2.61	17.61	1575	706
M4r5b-2	1.12	2.43	67.13	976	490
M4r5b-3	1.12	2.64	40.25	1661	774
M4r5b-4	1.12	3.20	57.65	4704	2143
M4r5b-5	1.12	2.36	32.83	950	417
M4r5s-1	1.12	2.43	59.25	877	473
M4r5s-2	1.12	2.91	22.87	2487	1204
M4r5s-3	1.12	2.65	68.49	1493	806
M4r5s-4	1.12	2.94	78.84	2719	1400
M4r5s-5	1.12	2.64	68.49	1440	774
M4r6b-1	1.21	2.65	10.92	1749	685
M4r6b-2	1.21	2.68	38.85	1650	734
M4r6b-3	1.21	2.60	16.42	1531	610
M4r6b-4	1.21	2.66	20.23	1454	659
M4r6s	1.21	2.68	46.57	1517	760

### 3.4 Binary properties

As discussed in Section 3.2.2, observations of binary stars in the galactic field and in open clusters are only complete for mass ratios  $q \geq 0.1$ ; consequently, our algorithm only generates primordial binaries with such mass ratios. Our work differs from previous studies of dynamical binary formation in clusters (e.g. Wall et al. 2019) or of evolution of a population of primordial binaries in clusters (e.g. Parker & Meyer 2014) by taking into account this observational limit, and comparing directly our population of binary systems with  $q \geq 0.1$  to the observed field population. We emphasize that any system with mass ratio  $q < 0.1$  would not have been included in the surveys on which our work is based. Where applicable, we therefore present two different sets of comparison: the comparison between our full simulation results and the field population (for consistency and ease of comparison with earlier literature), and the comparison between our simulation results with  $q \geq 0.1$  (hereafter, observable simulation results) and the field population.

To consider stars to be members of a binary, we require the stars to be gravitationally bound and perturbations by the other cluster stars must be comparatively small. Following Wall et al. (2019), we consider a system with primary mass  $M_1$ , companion mass  $M_2$  and semi-major axis  $a$  to be perturbed if there is a star with mass  $M_p$  and within a distance  $d$  of the system’s centre of mass such that

$$\frac{4a^2}{M_1M_2} \left| \frac{M_1M_p}{(d-a)^2} - \frac{M_2M_p}{(d+a)^2} \right| > 3. \quad (3.6)$$

To avoid considering stable triple systems as perturbed binaries, we add a condition that the system will not be considered perturbed if the third star is gravitationally bound to either the primary or the companion. Our conclusions are robust to the addition of this condition. To account for possible triple or higher order systems, we calculate the binary fraction as a function of primary mass as the fraction of stars in each mass range that are primaries (i.e. the most massive star in a stable system) but include each

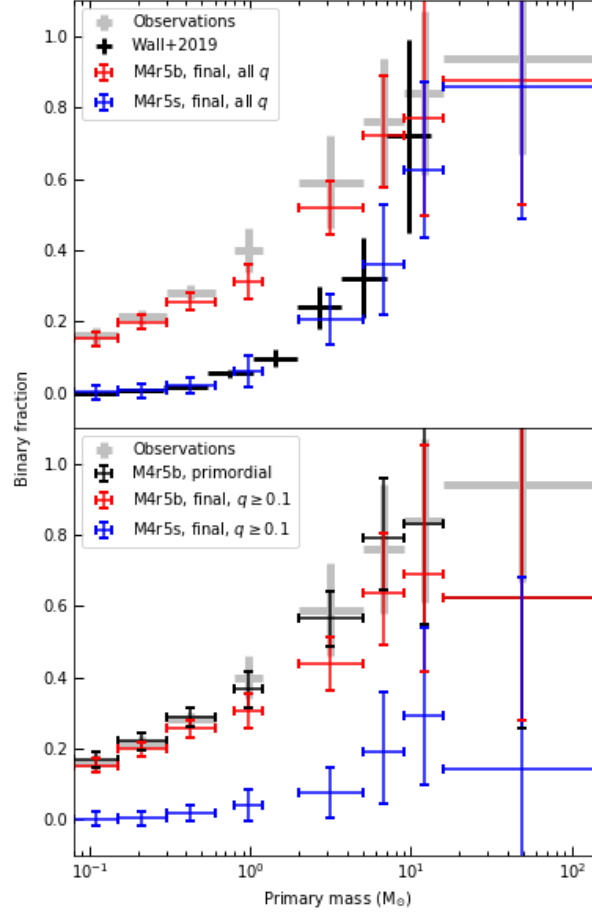


FIGURE 3.6: Binary fraction as a function of primary mass in M4r5, for the full binary population (top) and for observable systems (bottom). The primordial binaries formed in M4r5b, the binaries present at the end of M4r5b and those present at the end of M4r5s are denoted respectively by the black, red and blue thin crosses. The primordial and final binary fractions are exactly equal for the highest mass bin in the bottom panel. Observations from main sequence stars in the solar neighbourhood (Moe & Di Stefano 2017; Winters et al. 2019), with mass ratios  $\geq 0.1$ , are provided for comparison as the solid grey crosses. Binaries from the simulations of Wall et al. (2019), which do not include primordial binaries, are denoted by the thick black crosses. All the errors in  $x$  correspond to the bin widths and the errors in  $y$  in the observations are from the observational uncertainties. The  $y$  errors on the simulation data from Wall et al. are  $1/\sqrt{N}$  (see Wall et al. 2019). The  $y$  errors on our simulation data are from the Poisson statistical errors:  $1/\sqrt{N}$  for  $N > 100$  and the tabulated  $1 \sigma$  confidence interval for  $N \leq 100$  (Gehrels 1986; Hughes & Hase 2010).

primary-companion pair in our analysis of binary properties.

### 3.4.1 Binary fractions

We compare the binary fraction from observations of main sequence field stars (Moe & Di Stefano 2017; Winters et al. 2019), the fraction of stars we form in primordial binaries, and the fraction of stars in unperturbed binary systems at the end of M4b and M4s. We plot the binary fraction as a function of primary mass for our full binary population (all  $q$ 's) and for observable systems ( $q \geq 0.1$ ) in M4r5 in Figure 3.6.

We first consider our observable simulation results, which only include binary systems with  $q \geq 0.1$ . As expected, primordial binaries generated with our algorithm result in field-like binary fractions at all masses (see Figure 3.1). The final distribution in M4b is consistent within uncertainties with observations and primordial fractions at all primary masses; we nevertheless note that the final fraction tends to be lower than either the observations or the primordial fraction. This trend is present at both resolutions; in M4r6b, the observable binary fraction between 0.30 and 0.60  $M_{\odot}$  is lower than what would be predicted by observations of main sequence field stars. This indicates that some primordial binaries are destroyed by dynamical interactions during cluster formation. The final distribution in M4s is not consistent within uncertainties with observations, at any primary mass. It is however consistent within uncertainties with the primordial and final distributions in M4b for the two highest mass bins, where uncertainties are very large.

For the full population of binary systems, we reproduce the results from Wall et al. (2019) and find that, at high primary masses, pure dynamical formation results in binary fractions consistent with observations of main sequence field stars. We also find that with our field-like prescription for primordial binaries, our full binary population is consistent with observed binary fractions at all primary masses. We emphasize that

these results should be used for comparison with previous literature, but do not reflect what we can observe due to the  $q \geq 0.1$  detection limit in solar-neighbourhood surveys.

Although pure dynamical formation leads to observable binary fractions consistent within uncertainties with observations at high primary masses, we argue that this is due only to the large uncertainties arising from the very small number of stars in the highest mass bins. In contrast with Wall et al. (2019), we find that we need primordial binaries at all primary masses in order to be consistent with observations of main sequence field stars, due to the additional constraint that our systems must have large enough mass ratios to be seen in observations.

### **3.4.2 Final binary properties**

We compare the final distributions of primary masses, mass ratios, semi-major axes and eccentricities in our simulations, and test the null hypothesis that they are drawn from the same distribution with the Mann-Whitney-Wilcoxon  $U$ -test (Wilcoxon 1945; Mann & Whitney 1947), which is similar to the Kolmogorov-Smirnov test but more suitable for larger numbers of data points. We consider the primordial distributions, and the full and observable final distributions in M4b and M4s. Where relevant, we quote the lowest confidence level we have between M4r5 and M4r6. The qualitative conclusions are always the same at both resolutions for observable systems. When comparing the primordial and final distributions, we find that our conclusions hold for each individual simulation.

We present the plot of the cumulative primary mass distributions for M4r5 in Figure 3.7. We do not reject the null hypothesis that the primordial and full final distributions of primary masses in M4b are drawn from the same underlying distribution. If we consider only observable systems, however, we find that the systems detected at the end of M4b have lower primary masses than the systems formed primordially in these simulations (93.5% confidence). Furthermore, primary masses at the end of M4s are higher

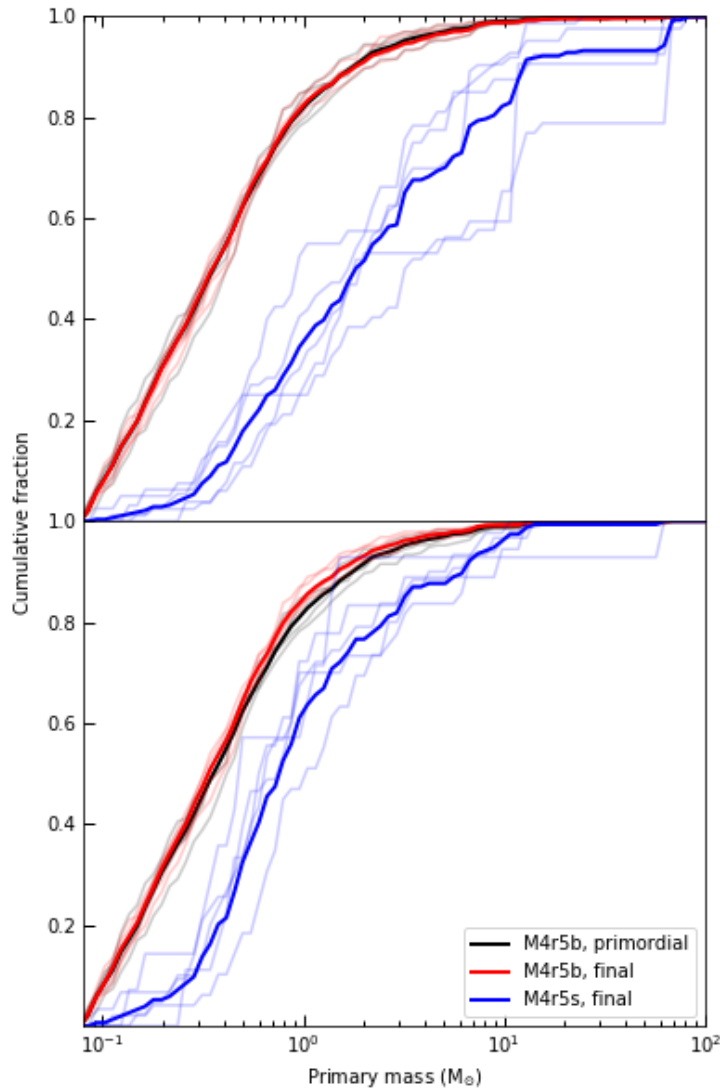


FIGURE 3.7: Cumulative distribution of primary masses in **M4r5**, for the full binary population (top) and observable systems (bottom). The solid black line denotes the primordial primary mass distribution in **M4r5b**, the solid red line denotes the final distribution in **M4r5b** and the solid blue line denotes the final distribution in **M4r5s**. The fainter lines denote the corresponding primary mass distribution in individual simulations. Pure dynamical formation results in systems with higher primary masses, while the dynamical evolution of the cluster with primordial binaries favours lower-mass primaries.

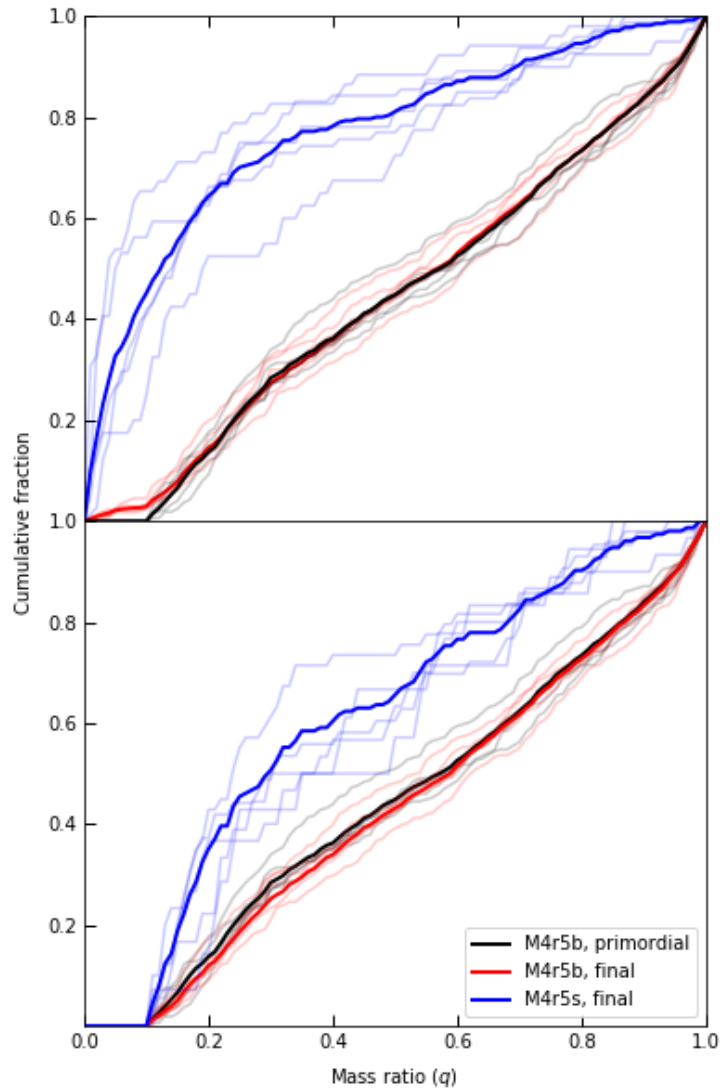


FIGURE 3.8: Cumulative distribution of mass ratios in M4r5, for the full binary population (top) and observable systems (bottom). The solid black line denotes the primordial mass ratio distribution in M4r5b, the solid red line denotes the final distribution in M4r5b and the solid blue line denotes the final distribution in M4r5s. The fainter lines denote the corresponding mass ratio distribution in individual simulations. Dynamical formation in both M4r5b and M4r5s favours systems with smaller mass ratios: up to 50% of the systems formed in M4r5s have mass ratios below the detection limit.

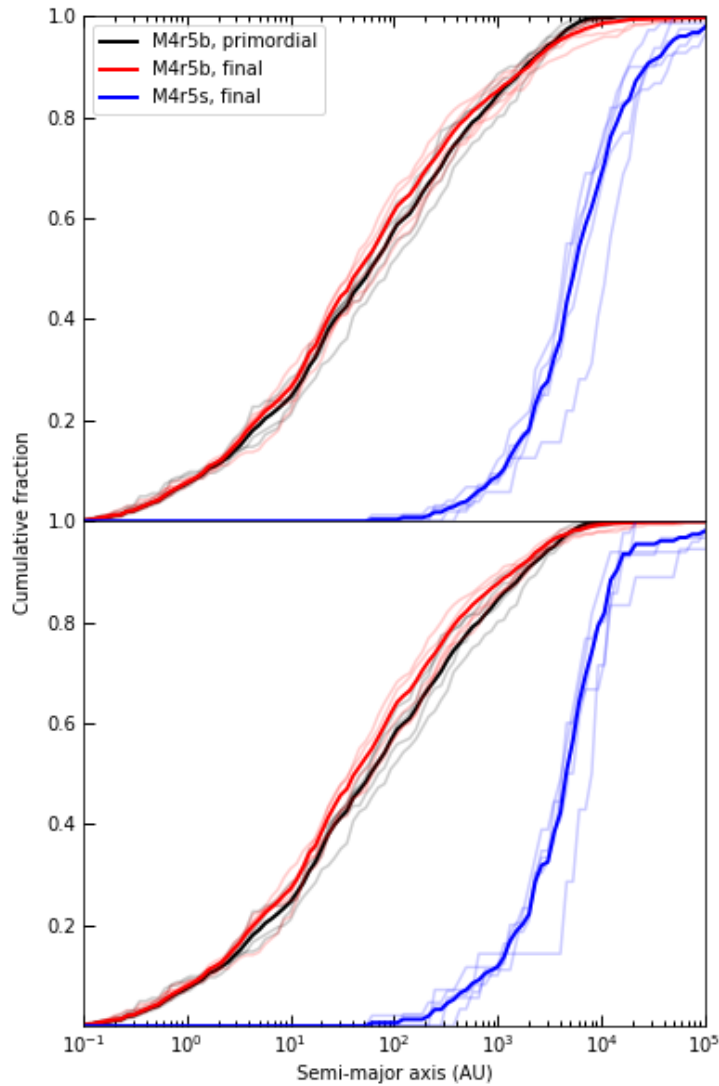


FIGURE 3.9: Cumulative distribution of semi-major axes in **M4r5**, for the full binary population (top) and observable systems (bottom). The solid black line denotes the primordial semi-major axis distribution in **M4r5b**, the solid red line denotes the final distribution in **M4r5b** and the solid blue line denotes the final distribution in **M4r5s**. The fainter lines denote the corresponding semi-major axis distribution in individual simulations. Pure dynamical formation results in systems with much larger semi-major axes; conversely, dynamical evolution during cluster formation results in smaller semi-major axes.

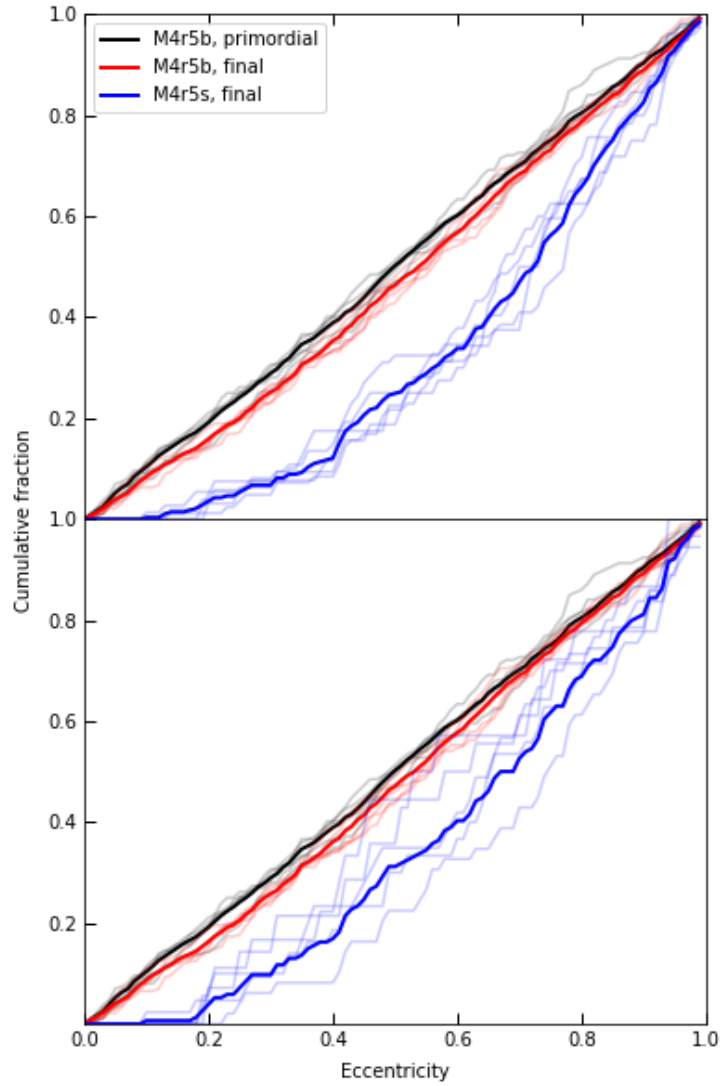


FIGURE 3.10: Cumulative distribution of eccentricities in M4r5, for the full binary population (top) and observable systems (bottom). The solid black line denotes the primordial eccentricity distribution in M4r5b, the solid red line denotes the final distribution in M4r5b and the solid blue line denotes the final distribution in M4r5s. The fainter lines denote the corresponding eccentricity distribution in individual simulations. Pure dynamical formation results in systems with much larger eccentricities.

than in **M4b**, both at the beginning and end of the simulations ( $> 99.9\%$  confidence).

We plot the cumulative mass ratio distributions for **M4r5** in Figure 3.8. The mass ratios for the full binary distributions at the end of **M4b** are consistent with having been drawn from the same distribution as the primordial mass ratios. This result is in agreement with previous studies of binaries in clusters (e.g. Parker & Reggiani 2013). Mass ratios of observable systems, however, are larger than primordial mass ratios (91.6% confidence). This alteration of the mass ratio distribution is in agreement with the results from simulations of young (e.g. Parker & Goodwin 2012) and globular (e.g. Sollima 2008) clusters. Mass ratios in **M4s** are smaller than those in **M4b**, either at the time of star formation or at the end of the simulation ( $> 99.9\%$  confidence).

The cumulative semi-major axis distributions for **M4r5** are shown in Figure 3.9. We find that the semi-major axes of systems detected at the end of **M4b** are smaller than those of the primordial systems. We are confident at respectively 96.9% and  $> 99.9\%$  that it is the case for our full sample of systems, and our sub-sample of observable systems. Conversely, the systems in **M4s** have larger semi-major axes than those formed primordially or those detected at the end of **M4b** ( $> 99.9\%$  confidence). This suggests that systems with large semi-major axes are preferentially formed dynamically.

We also plot the cumulative distribution of eccentricities in **M4r5** in Figure 3.10. The systems detected at the end of **M4b** are more eccentric than the primordial systems formed in the simulation for either our full sample (99.6% confidence) or just the observable systems (98.3%). This result is consistent with what we would expect of long-term dynamical evolution of binary systems in clusters, where repeated dynamical encounters increase eccentricities (e.g. Hills 1975; Heggie & Rasio 1996; Ivanova et al. 2006). Similarly, we are also confident at  $> 99.9\%$  that systems in **M4s** have larger eccentricities than either those formed primordially or those detected at the end of **M4b**. We argue that dynamical interactions form eccentric systems preferentially, causing the

larger eccentricities in **M4b** and especially **M4s**.

All the changes we detect in the distributions are small but statistically significant. They suggest that very early during cluster formation, while there is still a significant amount of gas and active star formation, dynamical interactions between the stars already modify binary systems in a non-random way. This highlights the need for the concurrent inclusion of gas and binaries in star cluster formation and early evolution simulations.

### **3.4.3 Modification of primordial binaries**

We investigate the fate of the systems formed primordially in our simulations. We present the cumulative distributions of semi-major axes and eccentricities for surviving systems (i.e. systems that have the same companion at the time of formation and at the end of the simulation) in **M4r5** in Figure 3.11. For **M4r5b** and **M4r6b**, we are confident at respectively 96.2% and 85.2% that the primordial and final semi-major axes are drawn from the same distribution. We are also confident at 83.1% and 89.7% that the surviving systems are more eccentric at the end of the simulation than when they form. This change in eccentricity of the surviving systems is consistent with our earlier result that systems at the end of **M4b** tend to have larger eccentricities than the primordial systems. Despite this result, the changes in the eccentricity distribution are very small, and are unlikely to be dynamically significant. We would expect long term evolution to cause an increase in eccentricity of hard binaries through dynamical interactions (Hills 1975; Heggie & Rasio 1996; Ivanova et al. 2006); we may see here the beginnings of this phenomenon.

We also compare the properties of the surviving subset of primordial systems to those of the full primordial population. The relevant primary masses, mass ratios, semi-major axes and eccentricities are plotted in Figure 3.12. We quote our lowest confidence

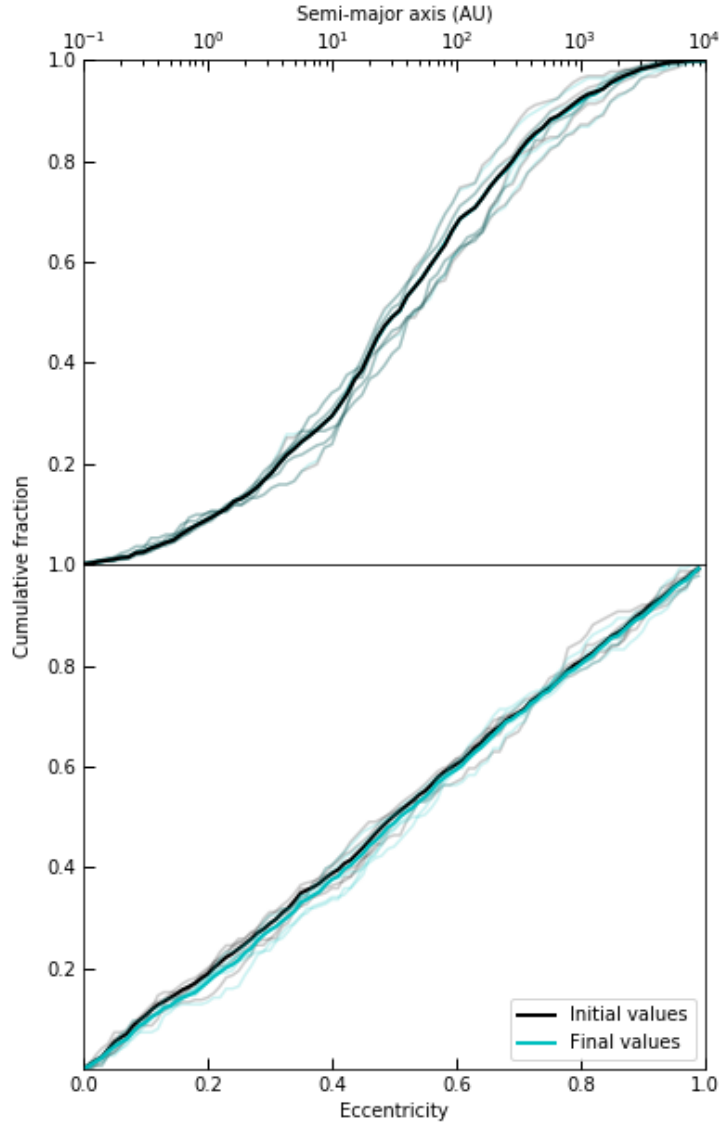


FIGURE 3.11: Cumulative distributions of semi-major axes (top) and eccentricities (bottom) for the primordial systems in **M4r5b** surviving to the end of our simulations. The solid grey lines represent the initial properties of the surviving systems, while the solid cyan lines represent their final properties. The fainter lines denote the corresponding distributions in individual simulations. Out of the 1274 binary systems we detect in **M4r5b**, 1077 systems are surviving systems. The distribution of the semi-major axes of the surviving systems at the end of the simulations is consistent with their distribution at the time of star formation (96.2% confidence). The final values of eccentricity are systematically larger (83.1% confidence). By definition, the primary masses and mass ratios of these systems are unchanged.

level between M4r5b and M4r6b, and verify that our conclusions hold for the surviving primordial binaries in any individual simulation. We are confident at 99.6% that the primordial systems surviving to the end of the simulation have smaller primary masses than the full primordial population. We are also confident at 98.5% that surviving primordial systems have larger mass ratios than the full population of primordial systems. This suggests that systems with high primary masses and small mass ratios are the most likely to either be dynamically destroyed or change companion due to three-body interactions.

We are confident at  $> 99.9\%$  that surviving primordial systems have smaller semi-major axes than the full primordial distribution. As the semi-major axes of surviving systems are not modified, we attribute this to the preferred dynamical destruction or modification of systems with large semi-major axes, as expected from the Heggie-Hills Law (Heggie 1975; Hills 1975). Finally, we are confident at 67.9% that surviving primordial systems have larger eccentricities than the full sample of primordial systems. On its own, this result does not indicate that systems with smaller eccentricities are preferentially destroyed, as it appears that the eccentricities of surviving systems increase during the simulation. Our results indicate that primordial binaries are destroyed within our simulations, and that systems may be more likely to be destroyed if they have certain properties. They also suggest that the orbital properties of primordial systems may already be modified in the earliest stages of cluster formation.

#### **3.4.4 Dynamical binary formation**

We also investigate whether the properties of the binaries formed dynamically in M4b and M4s are the same. We present plots of the primary masses, mass ratios, semi-major axes and eccentricities for binaries formed dynamically in M4r5 in Figure 3.13. In M4b, we consider that a binary is formed dynamically if the primary changed companion or the primary was not previously in a binary system.

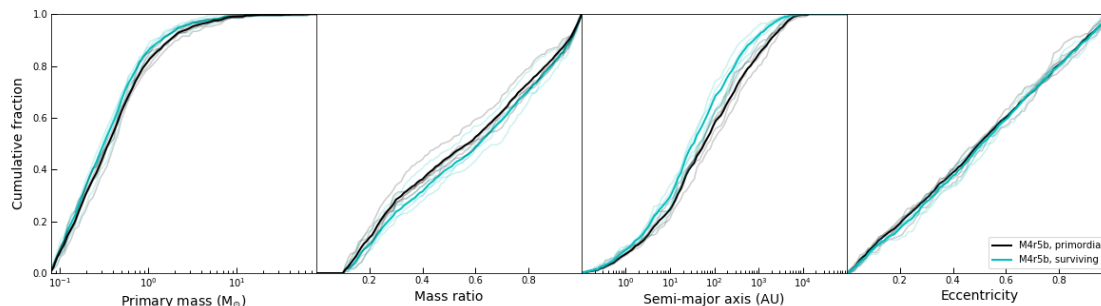


FIGURE 3.12: Cumulative distributions of primary masses, mass ratios, semi-major axes and eccentricities for the primordial systems in **M4r5b**. The black solid lines represent all the primordial systems formed in our simulations and the solid cyan lines represent the primordial systems that survive until the end of simulations. The fainter lines denote the corresponding distributions in individual simulations. Out of 1789 primordial systems, 260 were fully destroyed and 66 changed companions; 1463 systems survived to the end of our simulations. The distributions of primary masses, mass ratios and semi-major axes are different for the full primordial population and the subset of surviving systems; it is ambiguous whether the eccentricity distribution changed.

We find, with confidence  $> 99.9\%$ , that the properties of binaries formed dynamically in simulations including primordial binaries are different from either the properties of primordial binaries or the properties of binaries formed dynamically in a simulation without primordial binaries. Furthermore, we find that the cumulative distributions of properties of binaries formed dynamically in **M4b** always lie between the cumulative distributions for primordial binaries and for **M4s**. Binaries formed dynamically in the presence of primordial binaries tend to have smaller primary masses than those arising from pure dynamical formation, but larger primary masses than primordial binaries. Conversely, they tend to have mass ratios smaller than the systems formed by pure dynamical interactions, but larger than the primordial systems. In **M4b**, dynamical binaries form with semi-major axes and eccentricities larger than the primordial systems, but smaller than they do in **M4s**.

These early results are consistent with our expectations of dynamical formation of binaries. In the case where binaries are formed primarily through single-single interactions,

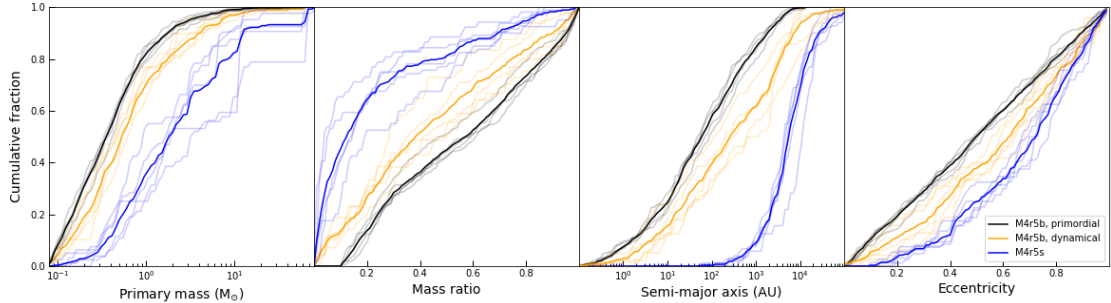


FIGURE 3.13: Cumulative distributions of primary masses, mass ratios, semi-major axes and eccentricities for binary systems formed dynamically in M4r5, and primordial binaries in M4r5b. The solid blue lines represent the 281 systems detected in M4r5s, the solid orange lines represent the 66 systems where the primary changed companions and the 341 systems formed dynamically with new primaries in M4r5b, and the solid black lines represent the primordial binaries in M4r5b. The fainter lines denote the corresponding distributions in individual simulations. The distributions are different for all four parameters; we note that the cumulative distributions for dynamical binaries in M4r5b always lie between the cumulative distributions for primordial binaries and M4r5s.

the resultant systems are more likely to have large primary masses, wide separations, small mass ratios, and large eccentricities as seen in Figure 3.13. When binaries can be formed through single-binary or higher order interactions, more complicated outcomes occur. High-mass primaries are still favoured, but systems with lower primary masses and high total mass (i.e. high mass ratio) are also likely to be involved in a dynamical encounter. During higher-order encounters, the rule of thumb is that the lowest-mass object involved in the encounter is ejected and replaced with a higher-mass object (Sigurdsson & Phinney 1993). Therefore, we might expect that dynamical encounters would tend to shift the mass ratio distribution towards larger values: the ejection of the lowest-mass object would result in an increase of a system’s mass ratio following each higher-order encounter. What we see in our simulations is that the systems which lose their original companion and later gain another one are typically high mass systems with comparatively very small companions at large semi-major axes, as shown in Figure 3.14. These systems tend to replace their original companion by a lower-mass one, which goes

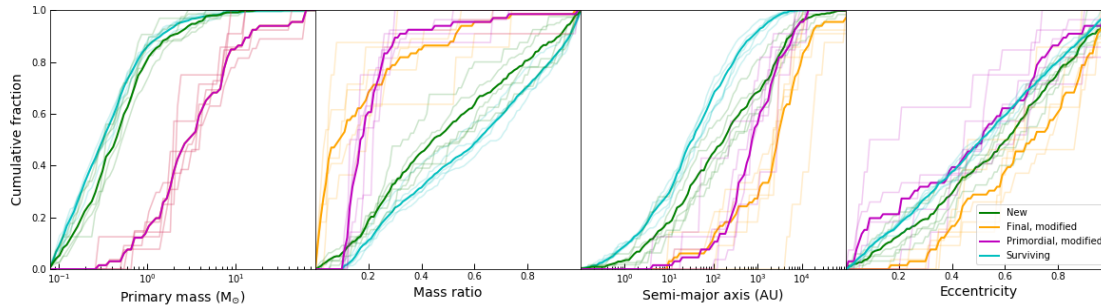


FIGURE 3.14: Cumulative distributions of primary masses, mass ratios, semi-major axes and eccentricities for surviving, modified and new binary systems in M4r5b. The solid green lines represent the 341 systems formed dynamically with new primaries in M4r5b, the solid magenta and orange lines represent the 66 systems where the primary changed companions respectively when they are formed and at the end of M4r5b, and the solid cyan lines represent the surviving systems in M4r5b. The fainter lines denote the corresponding distributions in individual simulations. The distributions are all different except for the primary mass distribution, which is by definition the same for the modified systems when they are formed and at the end of the simulation.

against our expectations for higher-order encounters. However, we see evidence that some of these weakly-bound binaries are broken up very soon after formation: some primaries lose their original companion within the first 0.1 Myr after they are formed. The massive primary then essentially acts like a single star, capturing low-mass single stars on wide eccentric orbits, or exchanging into a lower-mass binary system.

We also create new binaries from primaries which were originally single stars. Those primaries also have slightly higher masses than the underlying population, and become binaries by capturing a lower-mass single star or exchanging into a binary system. Tighter binary systems with smaller semi-major axes can be created through these exchange encounters than in the single-single case, and the extreme eccentricities that come from the near-parabolic encounters are not necessary when one of the original systems is already a binary.

## **3.5 Summary and discussion**

### **3.5.1 Summary**

We implement primordial binaries in the coupled MHD and direct N-body code TORCH (Wall et al. 2019), which couples FLASH (Fryxell et al. 2000) with the N-body code PH4 (McMillan et al. 2012) and the stellar evolution code SEBA (Portegies Zwart & Verbunt 1996) via the AMUSE framework (Portegies Zwart & McMillan 2019). We develop an algorithm to generate a population of binaries with mass-dependent binary fractions, periods, mass ratios and eccentricities. We also modify the star formation routine in TORCH to force the concurrent formation of the stars in a binary system. As an ansatz, we use the field distribution as our initial population of binaries. We perform 15 simulations; after the initial onset of star formation in each simulation, we see continuous and increasing star formation. Nine of our simulations include a population of primordial binaries, introduced following an extensive set of prescriptions. We follow the dynamical evolution of the binary population, and characterize it at the end of the simulations, 1.2–2 Myr after the onset of star formation. These first results suggest that concurrently modelling gas, stellar dynamics and binary systems during the earliest stages of star cluster formation is important, as binary systems are already being modified.

We investigate the impact of dynamical interactions during cluster formation on the primordial population of binaries. Our results indicate that dynamical interactions cause small but statistically significant changes in the distributions of binaries' primary masses, mass ratios, semi-major axes and eccentricities for systems above the  $q \geq 0.1$  detection limit. We note that if we consider the full binary population (i.e. if we also consider systems with mass ratios  $q < 0.1$ ), the differences in the distributions of primary masses and mass ratios are not obvious. We also find that primordial binaries are needed at all primary masses to reproduce the observed binary fraction above the  $q \geq 0.1$  detection limit. We argue that the distinction between the full binary population and the subset

of observable systems is important, as observations are incomplete for  $q < 0.1$  and considering only the systems with  $q \geq 0.1$  significantly affects our conclusions. We find that all our conclusions are robust to a change in spatial resolution by a factor of 2.

We observe both dynamical formation and destruction of binary systems in M4b, which includes an initial population of binaries. In these simulations, we see that systems formed dynamically do not have the same properties as primordial systems, and more importantly, that systems formed dynamically in M4b do not have the same properties as those formed in M4s, which includes only single stars initially. The cumulative distributions of primary masses, mass ratios, semi-major axes and eccentricities formed dynamically in M4b lie between the primordial distribution and the distribution resulting from pure dynamical formation in M4s. The presence of an initial population of binary stars has a significant impact on the subsequent binary properties in the star cluster. We find that systems with higher primary masses, lower mass ratios, larger semi-major axes and larger eccentricities are preferentially formed dynamically. We also find that systems with higher primary masses, smaller mass ratios and larger semi-major axes are preferentially destroyed or modified by dynamical interactions. Globally, dynamical evolution of a field-like primordial population favours systems with smaller primary masses, larger mass ratios, smaller semi-major axes and larger eccentricities. Most importantly, our results demonstrate that even in the earliest stages of cluster formation, when there is still a significant amount of gas and active star formation, dynamical interactions modify the binary population.

### **3.5.2 Discussion**

These simulations indicate that dynamical interactions in embedded clusters modify the properties of the primordial distribution of binaries by forming and destroying systems, but do not modify the mass-dependent binary fraction. We emphasize that our simulations model the earliest stages of star cluster formation, and thus that we are probing

those dynamical interactions that act on the binary systems on short timescales. Our analysis is conducted 1.2 – 2 Myr after the onset of star formation, while there is still active star formation and there has been very little feedback from the stars. Furthermore, protostellar outflows, which we do not include, play a role in regulating star formation efficiency in low-mass star forming regions (Matzner & McKee 2000). With protostellar outflows, fewer stars would be formed during the earliest stages of cluster formation, and thus dynamical interactions between these stars would likely have a smaller impact on the properties of the binary distribution. Magnetic fields, which are absent from our simulations, also participate in the regulation of star formation (Price & Bate 2008). Gas dynamical friction, which acts on scales smaller than our gas spatial resolution, may be a channel for the formation of short-period binaries with circular orbits (Gorti & Bhatt 1996; Stahler 2010). Its absence may play a part in driving the shift towards larger semi-major axes and eccentricities. Our simulations were also conducted with a single choice for the initial gas properties (total mass, initial size of the cloud, etc). Additional simulations are needed to determine whether the global gas properties play a significant role in modifying the population of binary stars.

The next steps are to investigate the impact of an initial magnetic field on the evolution of an initial population of binaries, as well as the impact of stellar winds. Massive stars will have a significant impact on the forming cluster: they interact gravitationally with other stars and deplete the supply of cold molecular gas available for star formation by heating it and ejecting it from the cluster.

In future work, we will alter our assumed primordial binary distribution to empirically determine what distribution leads to the field binary distribution observed after dynamical interactions in the embedded cluster. An important feature of the dynamical evolution appears to be the destruction of systems with massive primaries, or the replacement of the observable companion by a companion with  $q < 0.1$  in such systems.

Our altered distribution should therefore favour the retention of the original companion in systems with massive primaries, which could be done by assuming smaller semi-major axes. This would be expected for primordial binaries forming from the fragmentation of a single core. In addition, primordial binaries with mass ratios  $q < 0.1$  likely do form primordially and may have a dynamically interesting effect on the binary populations. Similarly, our primordial binary population is based on the full distributions of parameters for observed primary-companion pairs in the field: the distributions include mass ratios and semi-major axes from the outer components of triples and higher order systems. Such systems are ubiquitous at high masses but the outer components are likely to have small mass ratios and large semi-major axes. An avenue to explore for our altered distribution would be to use distributions derived exclusively from only binaries and the inner components of hierarchical systems. It is likely some of the systems detected in our simulations are dynamically formed stable triples or higher order systems, which we will also address in future work.

## **Acknowledgements**

We warmly thank Ralf Klessen for useful discussions. We also thank the referee, Douglas Heggie, for comments that improved the manuscript. We gratefully acknowledge the hospitality of the Centre for Computational Astrophysics, where this work was started during the first Torch users meeting in 2019. M-MML, SLWM, and AT are partly supported by US NSF grant AST18-15461. CCC and AS are supported by the Natural Sciences and Engineering Research Council of Canada. The simulations in this work were conducted on Cartesius; we acknowledge the Dutch National Supercomputing Center SURFSara grant 15520.

## CHAPTER 4

### DISCUSSION & FUTURE WORK

The formation of star clusters within GMCs is governed by the interplay among hydrodynamics, stellar dynamics, radiative transfer and stellar evolution. In recent years, multi-physics simulations including these processes, as well as active star formation, have become possible, with in particular the advent of TORCH (Wall et al. 2019; Wall et al. 2020) and STARFORGE (Guszejnov et al. 2021; Grudić et al. 2021). An important limitation of these suites of simulations lies in their subgrid star formation recipe, which does not allow, in its original form, the formation of binary star systems as a direct result of star formation. Primordial binaries are however required for any comprehensive treatment of cluster formation: most stars are formed in binaries (Reipurth et al. 2014) and massive stars are almost always formed with a close companion (Sana et al. 2012). These massive binaries likely shape the dynamical evolution of star clusters, and their feedback is predicted to have a very strong influence on the surrounding GMC.

In this thesis, we have presented the implementation of a recipe for primordial binary formation in TORCH. We enforced a distribution of primordial binaries with properties

drawn from field-like distributions, based on the analytic probability distributions found by Moe & Di Stefano (2017), supplemented by the results from Winters et al. (2019) at low masses. We obtained a first series of results, demonstrating that an initial population of binaries is modified during the earliest stages of star cluster formation, before the evolution of the cluster becomes dominated by stellar feedback. At this date, our simulations are still ongoing, as is a new suite of simulations with variations in the gas initial virial parameter  $\alpha$  and random turbulent velocity pattern. We stress that the work presented in this thesis is the first numerical study to include concurrent modelling of hydrodynamics, active star formation and stellar dynamics with an initial population of binaries, combined with radiative and momentum stellar feedback.

We summarize the key results from our published paper and their implications in Section 4.1. In Section 4.2, we present the evolution of our simulations since the publication of Chapter 3. In Section 4.3, we discuss our most recent work on the influence on the gas initial conditions. In Section 4.4, we conclude with an overview of possible directions for further investigation.

## **4.1 Key results and their implications**

We conducted a suite of 15 simulations, 9 of which included primordial binaries. All of our simulations were initialized from the same collapsing turbulent sphere of cold gas with mass  $\sim 10^4 M_{\odot}$ . We compared the distributions of primordial binaries formed in our simulations to the distributions of binaries found 1.2–2 Myr after the onset of star formation, when feedback from massive stars start to dominate the simulations. We also investigated the effects of dynamical binary formation and destruction. The main results and their implications are outlined below.

We compare the mass-dependent binary fraction for binaries formed in our simulations without primordial binaries to observations of the mass-dependent binary fraction

in the Galactic field. With a mass ratio threshold of  $q \geq 0.1$ , we find that *primordial binaries are necessary at all masses to reproduce the binary fraction observed in the Galactic field*. This result contrasts with the conclusions from Wall et al. (2019), who use TORCH without a prescription for primordial binaries: they find that dynamical interactions suffice in obtaining field-like multiplicity fractions at large primary masses. Similarly, Torniamenti et al. (2021), in their N-body simulations with binaries, find that dynamical interactions reproduce the trend of monotonically increasing multiplicity with primary mass. Despite the apparent tension between our results, the three suites of simulations are in fact in agreement: when all binary systems are considered, dynamical interactions alone reproduce the increase of multiplicity with mass and lead to field-like binary fractions at high masses. When considering only the subset of binaries with  $q \geq 0.1$ , however, this trend does not arise naturally from pure dynamical interactions. Any attempt at reproducing the observed binary fraction in clusters or in the field should thus include a primordial binary population at all masses.

We also investigate the possibility of preferential formation or destruction of binary systems via dynamical interactions in the embedded cluster. We verify the presence of preferential destruction by comparing the primordial systems formed in our simulations to the subset of primordial systems surviving to the end of the simulation. We verify the presence of preferential formation by comparing the systems formed dynamically in our simulations with binaries to the primordial systems formed in these simulations. We find that *dynamical interactions result in a combination of preferential formation and preferential destruction of binary systems*. Systems with lower mass ratios and larger semi-major axes tend to be both formed and destroyed more frequently. Systems with smaller primary masses are more likely to be destroyed or modified; systems with larger primary masses and larger eccentricities are more likely to be formed. *The net effect of dynamical interactions modifies the initial distribution of binary properties: primary masses and semi-major axes tend to decrease, while mass ratios and eccentricities tend*

to increase. This informs what primordial distribution of binaries should be adopted in order to recover the field – or young cluster – population after dynamical interactions. In particular, the mass distribution of primaries with companions above the  $q \geq 0.1$  threshold is shifted to smaller values; the primordial distribution should thus include an excess of intermediate and high mass binaries compared to the field distribution. Such a change would also address the slight decrease in the fraction of observable systems.

The key result from our first published suite of simulations could thus be summarized as follows: *dynamical interactions during the earliest stages of star cluster formation, when the cluster is still fully embedded in gas, are important for determining the properties of binary star systems.* This suggests that even observations of binaries in star forming regions (e.g. Kouwenhoven et al. 2005; Duchêne et al. 2018) already carry an imprint from dynamical interactions, and are thus not fully representative of the primordial population. Observations of protostars embedded in gas, made easier in recent years with the *Atacama Large Millimeter/submillimeter Array* (ALMA) may provide better constraints on the primordial population from the observational side. ALMA observations have already revealed evidence of both disk and core fragmentation (Tobin et al. 2016b; Lee et al. 2017), however mass estimates and the observation of orbital parameters are less straightforward for protostars. Multi-physics simulations of embedded clusters therefore emerge as a likely source of insights in constraining the primordial binary population. The inclusion of gas in our simulations, and thus the possibility to model gas-mediated interactions, appear important: Wall et al. (2019), using TORCH, argue that gas-mediated interactions modified some of their dynamically-formed binaries. Furthermore, Parker & Meyer (2014), using a similar prescription for primordial binaries but without modelling hydrodynamics, find that there is no net effect from the dynamical interactions on the population of binaries. Another relevant feature of our simulations is the hierarchical assembly of our clusters, from the motion of subclusters along dense filaments. Dynamically, merging subclusters are more complicated than

spherical cluster models often used in N-body simulations. This indicates that the current modelling of gas and stars, along with active star formation and stellar feedback, is a key ingredient in determining what dynamical modifications take place and thus, what is the primordial population of binaries.

## 4.2 Current state of our simulations

Most of the simulations presented in Chapter 3 are still ongoing, with the aim to reach gas expulsion. Since we found the results to be qualitatively unaffected by an increase in spatial resolution by a factor of 2, we continue only the simulations at maximum refinement 5, corresponding to a spatial resolution of  $6.8 \times 10^{-2}$  pc. The work discussed here consists of preliminary results for a paper in preparation, exploring the variations in the binary distributions driven by differences in the stellar populations and their feedback, the boundedness of the initial cloud and its turbulent velocity pattern. We present the current properties of our simulations – such as number of stars on the grid, formed stellar mass and mass of the most massive star – in Table 4.1. All the simulations have progressed a minimum of 1.6 Myr since the onset of star formation, and each simulation includes at least one massive O-star. For the analysis, we limit ourselves to the subset of binaries with  $q \geq 0.1$ , which is the completeness limit of the observational surveys used to generate our primordial binaries.

In particular, we are interested in the variations between the simulations. In Figure 4.1, we present our two simulations most advanced in time, **M4b4** (**M4r5b-4** in Chapter 3) and **M4s4** (**M4r5s-4**), having reached respectively 3.26 Myr and 3.11 Myr. In contrast with the analysis presented in Chapter 3, the effects of feedback from massive stars now influence the evolution of the gas structures (and thus of the star formation) in the simulations. Winds and radiation from the very massive  $78.8 M_{\odot}$  star formed 0.2 Myr ago in **M4s4** have carved out a cavity in the gas, most obvious in the  $y$ -projection

TABLE 4.1: Current properties of our simulations. All simulations are initialized from the same turbulent sphere of gas, with  $\alpha = 0.4$ , a cloud mass of  $9108 M_{\odot}$  and a free-fall time of 1.57 Myr. The onset of star formation occurs at 1.12 Myr. The simulations labelled with **b** include primordial binaries; those labelled with **s** do not.  $t$  denotes the time since the beginning of the simulation;  $N_*$  denotes the number of stars on the grid;  $M_*$  denotes the formed stellar mass;  $M_s$  denotes the mass contained in the sinks;  $M_g$  denotes the gas mass on the grid;  $\epsilon_{ff}$  denotes the SFE per free-fall time (calculated from the formed stellar mass and the initial cloud mass);  $M_m$  denotes the mass of the most massive star and  $t_m$  the time at which it formed.

<i>Name</i>	$t$ (Myr)	$N_*$	$M_*$ ( $M_{\odot}$ )	$M_s$ ( $M_{\odot}$ )	$M_g$ ( $M_{\odot}$ )	$\epsilon_{ff}$	$M_m$ ( $M_{\odot}$ )	$t_m$ (Myr)
M4b1	2.83	2198	$9.97 \times 10^2$	104	$8.21 \times 10^3$	6.1%	29.7	2.69
M4b2	2.72	1521	$6.81 \times 10^2$	38.8	$8.59 \times 10^3$	4.3%	67.1	2.34
M4b3	2.77	2100	$1.01 \times 10^3$	81.3	$8.22 \times 10^3$	6.3%	40.2	2.63
M4b4	3.26	4991	$2.39 \times 10^3$	125	$6.83 \times 10^3$	12.6%	86.2	3.24
M4b5	2.76	1807	$8.67 \times 10^2$	63.9	$8.39 \times 10^3$	5.4%	32.8	2.22
M4s1	2.75	1427	$8.03 \times 10^2$	34.5	$8.46 \times 10^3$	5.0%	59.2	2.28
M4s2	3.06	3099	$1.76 \times 10^3$	42.9	$7.52 \times 10^3$	9.9%	78.8	2.91
M4s3	2.82	1881	$1.02 \times 10^3$	116	$8.17 \times 10^3$	6.2%	68.5	2.64
M4s4	3.11	3252	$1.86 \times 10^3$	57.8	$7.39 \times 10^3$	10.3%	78.8	2.91
M4s5	2.74	1845	$9.77 \times 10^2$	112	$8.22 \times 10^3$	6.1%	68.3	2.63

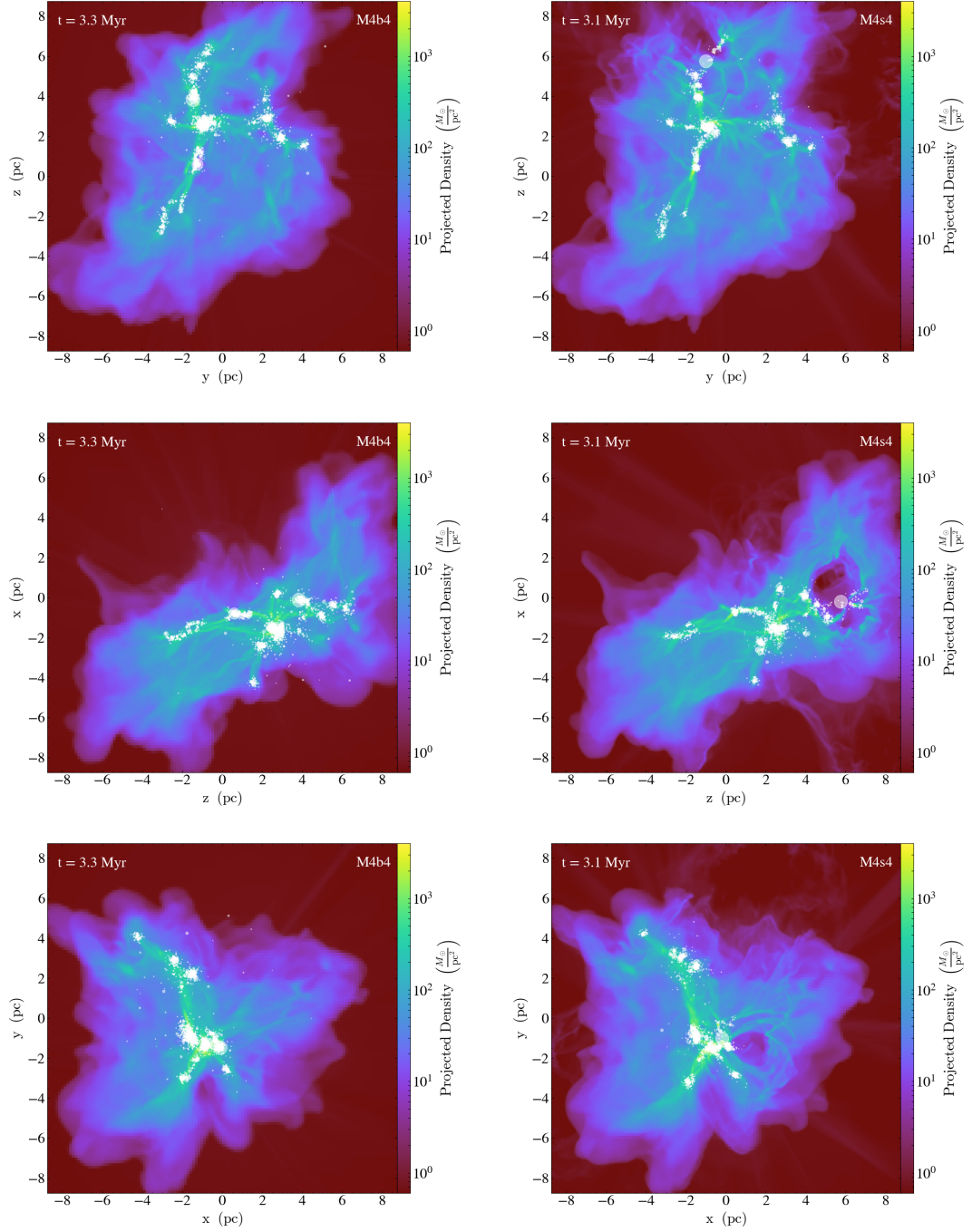


FIGURE 4.1: Projected gas densities for M4b4 (left) and M4s4 (right), respectively 3.26 Myr and 3.11 Myr after the beginning of the simulation. The massive  $78.8 M_{\odot}$  star in M4s4, formed 0.2 Myr ago, has blown away a cavity from its wind and radiation (see middle right panel).

in Figure 4.1. We expect the differences will increase with time: the  $78.8 M_{\odot}$  star in **M4s4** may blow out more gas while the  $86.2 M_{\odot}$  star in **M4b4** (formed 0.02 Myr ago) is expected to start carving away the nearby gas.

Our first point of comparison between our simulations is their star formation rate (SFR) as a function of time. If our simulations behave similarly to star-forming GMCs, we expect the SFR to increase monotonically with time until star formation is halted, and the scatter between the different simulations to span up to an order of magnitude (see e.g. Lee et al. 2016a, and references therein). We plot the evolution of the SFR as a function of time after the onset of star formation for our five simulations with primordial binaries and our five simulations without primordial binaries (hereafter, our fiducial suite of simulations), and present it in Figure 4.2. All simulations are initialized from the same initial turbulent sphere of gas; the only differences in the SFR are thus a direct consequence of which stars form and the influence they exert upon the gas. We find that the SFR generally increases exponentially for each simulation, although it may decrease momentarily while a sink is accreting material to form a massive star. We also note that, at any given time, the SFR may vary by almost an order of magnitude between simulations. There is however no systematic difference between the SFRs in different simulations: there is no simulation in which the SFR remains systematically higher or lower than in the others.

We are also interested in the spread of binary properties – i.e. mass ratios  $q$ , primary masses  $M_1$ , semi-major axes  $a$  and eccentricities  $e$  – at equal times. Our simulation that is the least advanced in time, **M4b2**, has now evolved for 1.6 Myr after the onset of star formation. We thus consider the distributions of binary properties for our five simulations with primordial binaries at this time. We plot the cumulative distributions of binary properties in Figure 4.3. With the Mann-Whitney-Wilcoxon  $U$ -test (Wilcoxon 1945; Mann & Whitney 1947), we verify if the distributions of binary properties are

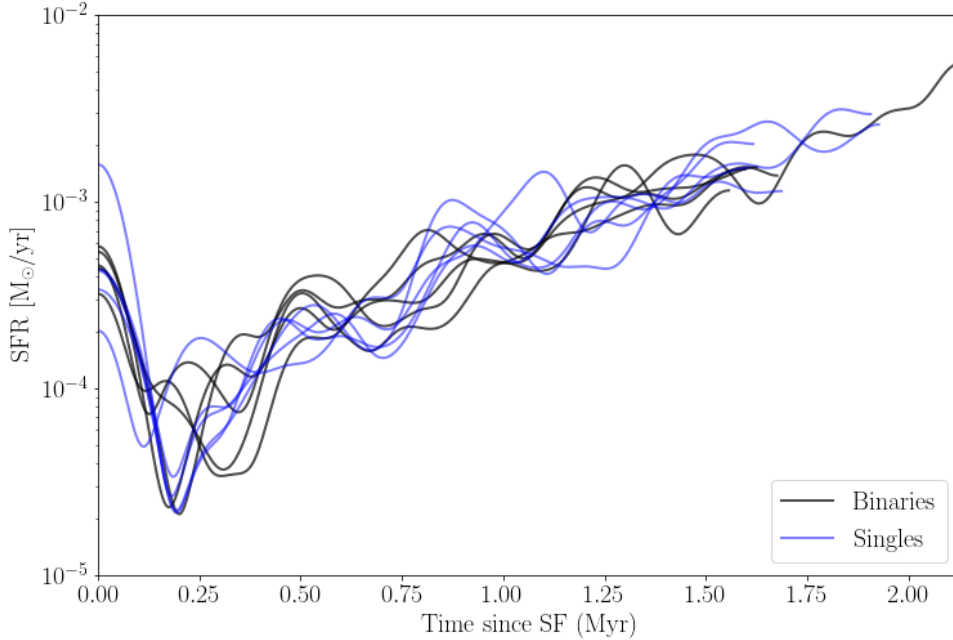


FIGURE 4.2: Star formation rate as a function of time after the onset of star formation. A Gaussian filter is applied to smooth the SFR over 50 kyr. The simulations with primordial binaries are shown in black; the simulations without primordial binaries are shown in blue. At equal times, SFRs vary by about half an order of magnitude.

			M4b1	M4b2	M4b3	M4b4	M4b5
$q$	smaller	M4b3	> 99%	99%	-	99%	96%
$e$	larger	M4b4	97%	97%	97%	-	98%

TABLE 4.2: Difference in binary properties, 1.6 Myr after the onset of star formation. The mass ratios  $q$  in M4b3 are smaller than in the other simulations; the eccentricities  $e$  are larger in M4b4 than in the other simulations.

pairwise consistent with having been drawn from the same underlying distribution. We find that no simulations are pairwise different for all properties, and that no simulation is an outlier for more than one property. Only two simulations are systematically different from the others, each for a single property; the confidences are listed in Table 4.2.

Some of our simulations have evolved for significantly longer than 1.6 Myr after the

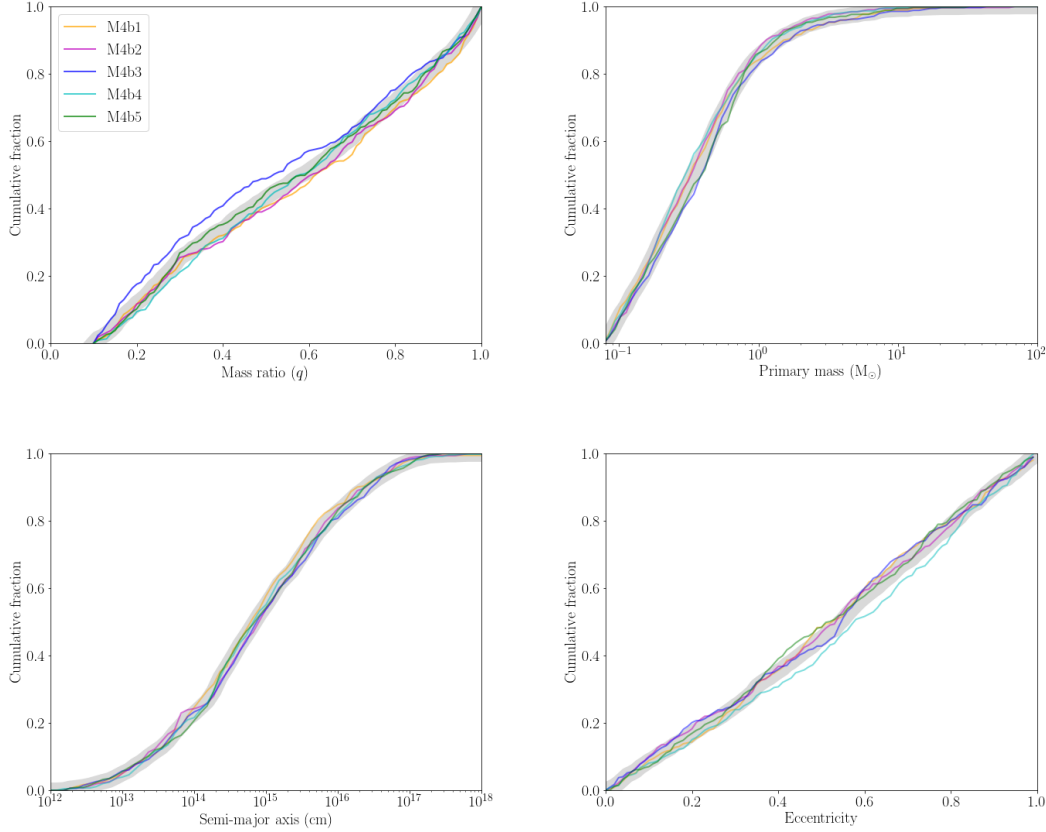


FIGURE 4.3: Cumulative distributions of mass ratios (top left), primary masses (top right), semi-major axes (bottom left) and eccentricities (bottom right) for our fiducial simulations with primordial binaries, 1.6 Myr after the onset of star formation. The thick grey line represents the cumulative distribution for the five simulations, while the colored lines represent the individual simulations.

onset of star formation; **M4b4**, in particular, has evolved for more than 2.1 Myr after the onset of star formation. For each of these simulations, we use the Mann-Whitney-Wilcoxon  $U$ -test to test for the changes found in Chapter 3. We present the confidence at which we detect these changes in Table 4.3. None of the simulations have undergone changes that are in contradiction with our previous results. For all simulations, we detect at least three of the four changes with confidence  $> 70\%$ . In **M4b4**, which is the simulation that has evolved for the longest – and thus presumably the one that carries the strongest

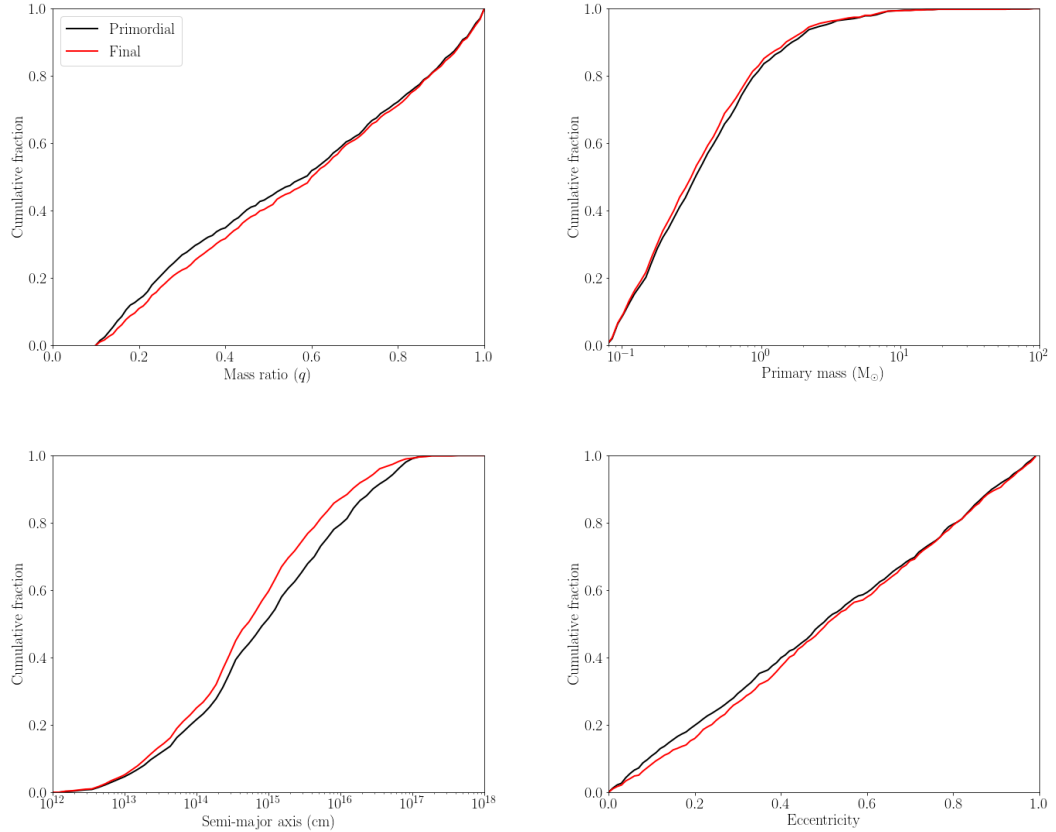


FIGURE 4.4: Cumulative distributions of mass ratios (top left), primary masses (top right), semi-major axes (bottom left) and eccentricities (bottom right), for M4b4, 2.14 Myr after the onset of star formation. The black lines represent the primordial binaries formed in the simulation and the red lines represent the binaries detected at the current time. All four distributions undergo statistically significant changes.

imprint from dynamical interactions – we detect all changes with confidence  $\geq 88\%$ . We plot the cumulative distributions of binary properties in Figure 4.4. In M4b1, which is the second most evolved simulation, changes in mass ratios, primary masses and semi-major axes are detected with confidence  $\geq 90\%$ .

The more recent results from our fiducial suite of simulations thus confirm the conclusions from Chapter 3. We note that there is some spread in binary properties at

	Mass ratio Increase	Primary mass Decrease	Semi-major axis Decrease	Eccentricity Increase
M4b1	92%	90%	97%	73%
M4b2	63%	70%	77%	93%
M4b3	82%	91%	96%	70%
M4b4	92%	90%	> 99%	88%
M4b5	70%	45%	72%	83%

TABLE 4.3: Confidence at which we detect changes in our distributions of binaries, for our five fiducial simulations with primordial binaries.

equal time between the different simulations, but that no simulation differs systematically from the others. We also note that the simulations that have undergone a larger amount of dynamical evolution show clearer trends for the increase of mass ratios and eccentricities, and the decrease of primary masses and semi-major axes.

### 4.3 The influence of initial conditions

Our fiducial suite of simulations uses a single set of initial conditions. However, we expect the amount and strength of the dynamical interactions to be influenced by the density of the stellar environment, which is in turn influenced by the conditions of the GMC in which star formation takes place. The SFR within a GMC, and thus the number of stars the GMC may form before it is dispersed by stellar feedback, is expected to decrease with increasing virial parameter (see e.g. Schrubba et al. 2019), defined here as

$$\alpha \equiv \frac{T}{|U|} \tag{4.1}$$

following Equation 1.3. Our fiducial simulations are conducted with a virial parameter  $\alpha = 0.4$ , which is at the low end of virial parameters derived from observations (e.g. Lee et al. 2016a). It was chosen originally to favour intense and abundant star formation, but the amount of change in binary properties obtained from this sub-virial cloud may be an upper limit. We thus conduct new simulations with and without a primordial population

TABLE 4.4: Current properties of our simulations with different initial conditions. All simulations except those labelled with **s** include primordial binaries. The free-fall times and initial cloud mass of **M4S3** and **M4S7** are within 1% of those for our fiducial simulations.  $t$  denotes the time since the beginning of the simulation;  $t_{SF}$  denotes the time since the onset of star formation;  $N_*$  denotes the number of stars on the grid;  $M_*$  denotes the formed stellar mass;  $M_S$  denotes the mass contained in the sinks;  $M_g$  denotes the gas mass on the grid;  $\epsilon_{ff}$  denotes the SFE per free-fall time;  $M_m$  denotes the mass of the most massive star and  $t_m$  the time at which it formed. Note that no O-star has formed in **V1-b**.

<i>Name</i>	$t$ (Myr)	$t_{SF}$ (Myr)	$N_*$	$M_*$ ( $M_\odot$ )	$M_s$ ( $M_\odot$ )	$M_g$ ( $M_\odot$ )	$\epsilon_{ff}$	$M_m$ ( $M_\odot$ )	$t_m$ (Myr)
<b>M4b4</b>	3.26	2.14	4991	$2.39 \times 10^3$	125	$6.83 \times 10^3$	12.6%	86.2	3.24
<b>M4s4</b>	3.11	1.99	3252	$1.86 \times 10^3$	57.8	$7.39 \times 10^3$	10.3%	78.8	2.91
<b>V1-b</b>	2.92	1.88	1294	$5.46 \times 10^2$	88.6	$7.62 \times 10^3$	3.2%	–	–
<b>V1-s</b>	3.25	2.21	1782	$8.15 \times 10^2$	53.2	$7.23 \times 10^3$	4.3%	31.5	3.17
<b>V2-b</b>	3.17	2.30	525	$2.38 \times 10^2$	21.3	$5.42 \times 10^3$	1.3%	20.4	3.06
<b>V2-s</b>	2.77	1.90	209	$1.71 \times 10^2$	11.4	$5.95 \times 10^3$	1.1%	64.1	2.50
<b>M4S3</b>	2.06	0.82	1987	$9.68 \times 10^2$	104	$8.34 \times 10^3$	8.1%	21.2	1.86
<b>M4S7</b>	2.05	0.97	2872	$1.41 \times 10^3$	75.9	$7.93 \times 10^3$	11.9%	64.4	2.02

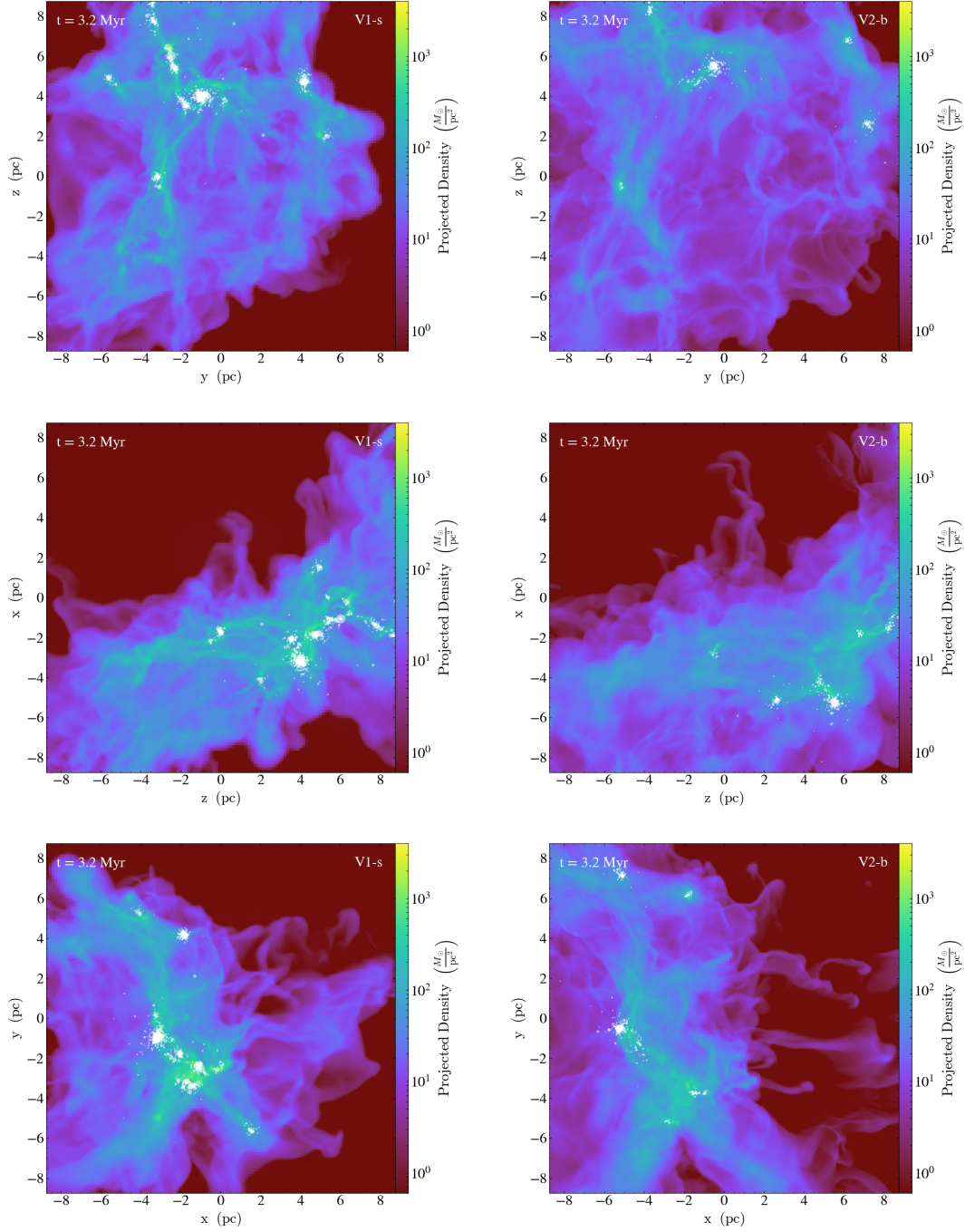


FIGURE 4.5: Projected gas density for V1-s (left) and V2-b (right). Some elements of the gas structure – e.g. the horizontal trend in the  $y$  projection, the inverted Y in the  $z$  projection – are similar (also see Figure 4.1 for  $\alpha = 0.4$ ) but become more diffuse with increasing  $\alpha$ .

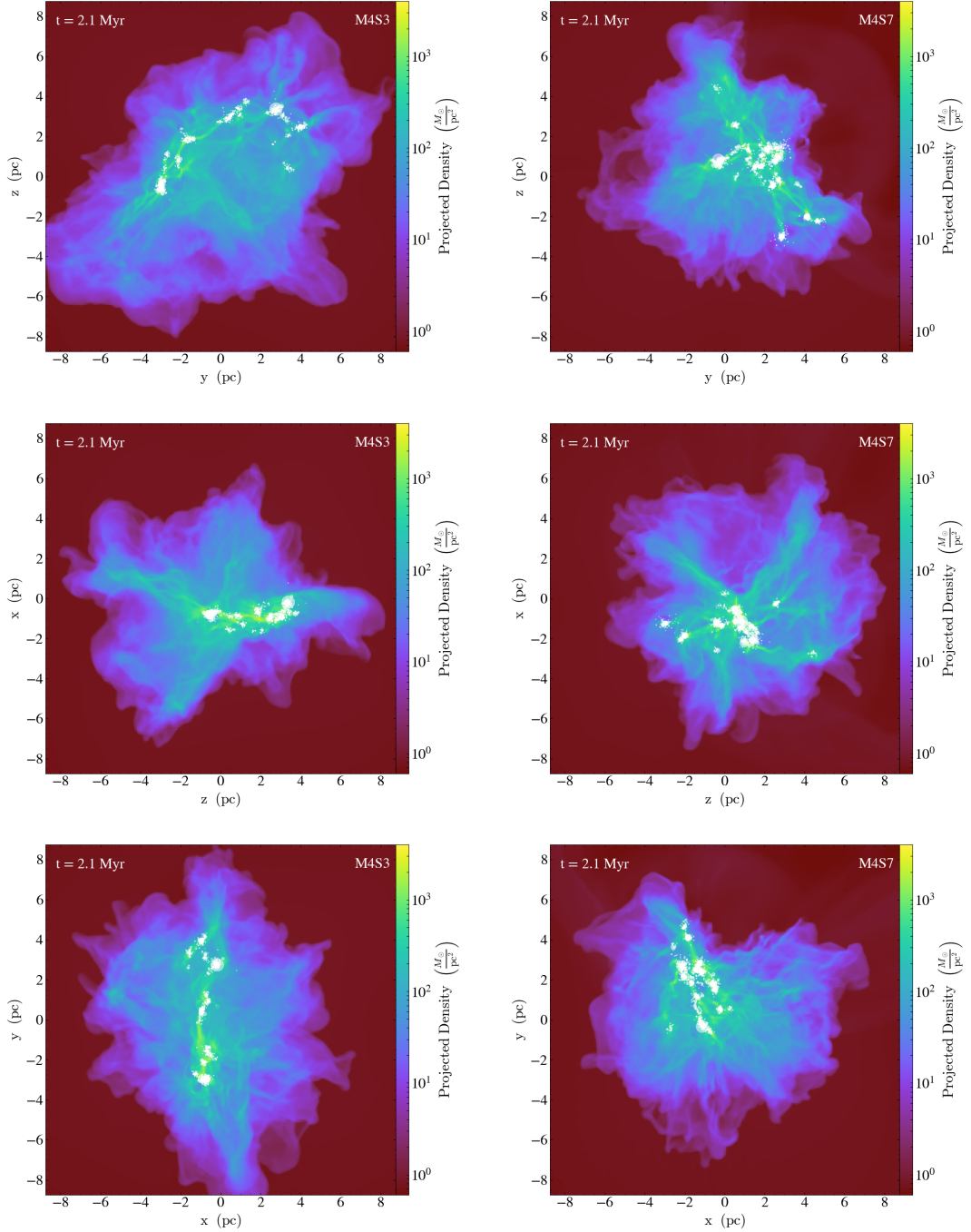


FIGURE 4.6: Projected gas density for M4S3 (left) and M3S7 (right). Due to the different random velocity pattern of the initial turbulent spheres, the gas structures in the two simulations are very different, and are also different from the gas structure in the fiducial simulations. Nonetheless, they display similar filamentary structures, within which star formation takes place.

of binaries, from a marginally bound ( $\alpha = 1.0$ , labelled **V1-b** and **V1-s**) and an unbound ( $\alpha = 2.0$ , labelled **V2-b** and **V2-s**) cloud. Those virial parameters match median values for nearby galaxies (Sun et al. 2018; Schruba et al. 2019). We obtain these new initial conditions by scaling up the velocity of the gas from our fiducial initial conditions; the only difference is the virial parameter, but the velocity structure is fixed. Observations also suggest that the virial parameter alone is not enough to explain the scatter in SFE in GMCs (Lee et al. 2016a). We thus also generate two sets of initial conditions with  $\alpha = 0.4$  and the same total mass  $\sim 10^4 M_{\odot}$ , but with a different velocity pattern for the gas. We perform one simulation with primordial binaries for each, labelled respectively **M4S3** and **M4S7**. The current properties of our six new simulations are presented in Table 4.4; the current properties of **M4b4** and **M4s4** are repeated there for ease of comparison. The star formation efficiency per free-fall time  $\epsilon_{ff}$  is notably lower in the simulations with larger virial parameters  $\alpha$ , and a larger amount of gas leaves the computational domain without forming stars, as demonstrated by the smaller gas mass on the grid coupled with the lower stellar mass. Examples of the gas structure for different virial parameters and different random velocity patterns are shown respectively in Figures 4.5 and 4.6.

The star formation rate as a function of time since the onset of star formation for the simulations with different virial parameters is plotted in Figure 4.7. Star formation starts earlier in the simulations with more turbulence: the first star forms after 1.04 Myr in the simulations with  $\alpha = 1.0$  and after 0.87 Myr in the simulations with  $\alpha = 2.0$ , while it forms after 1.12 Myr in the simulations with  $\alpha = 0.4$ . The SFRs are higher in the simulations with lower virial parameters. This is consistent with our expectations: turbulence both promotes and prevents star formation (Ballesteros-Paredes et al. 2007). At equal times, we thus expect our fiducial simulations to be more dynamically evolved. We investigate whether it is the case by comparing the distributions of binary properties: we verify if the fiducial distribution is statistically different from the distribution from the simulation with the larger  $\alpha$ , in the same direction as what is expected from the

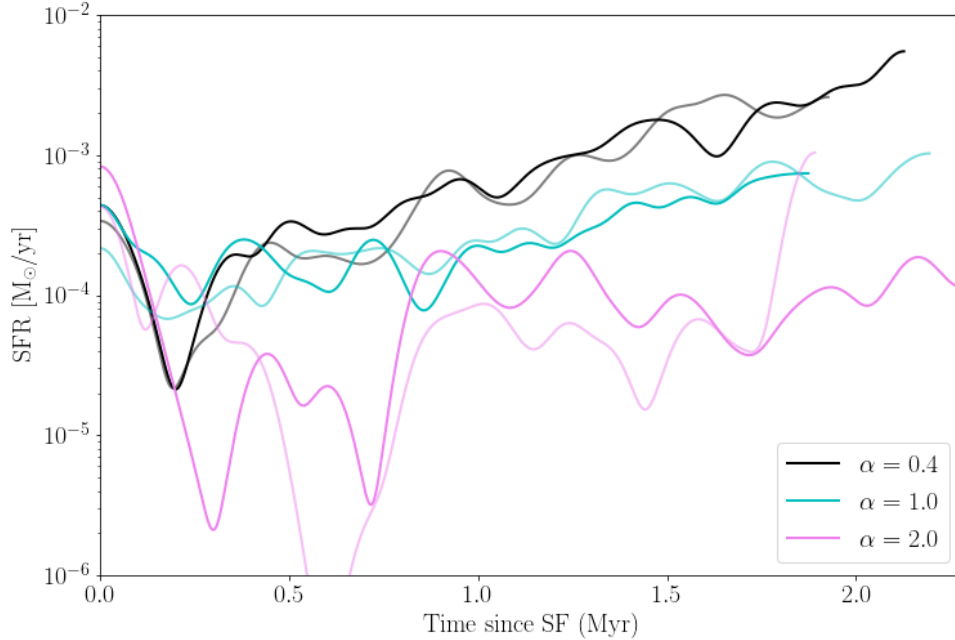


FIGURE 4.7: Star formation rate as a function of time after the onset of star formation, for the three different virial parameters. A Gaussian filter is applied to smooth the SFR over 50 kyr. The simulations with  $\alpha = 0.4$  (M4b4 and M4s4 are chosen as examples) are shown in black, those with  $\alpha = 1.0$  are shown in cyan and those with  $\alpha = 2.0$  are shown in magenta; the solid lines denote the simulations with primordial binaries and the shaded lines the ones without primordial binaries. The SFR is systematically lower in simulations with higher  $\alpha$ .

dynamical interactions discussed in Chapter 3 and above. 1.6 Myr after the onset of star formation, we are confident at  $\geq 80\%$  that the mass ratios and eccentricities in V2-b are smaller than those in the fiducial runs, and that the primary masses are larger. We also find that semi-major axes in V1-b are larger than those in the fiducial runs, with 75% confidence. This would suggest that the binaries in our runs with larger  $\alpha$  have been less influenced by dynamical interactions than those in our fiducial runs, at the same time after the onset of star formation. We can also investigate the difference between the primordial and current distributions of binaries in V1-b and V2-b. We summarize our confidence for the different expected changes in Table 4.5. For V1-b, we find a decrease

	Mass ratio Increase	Primary mass Decrease	Semi-major axis Decrease	Eccentricity Increase
V1-b	57%	69%	72%	70%
V2-b	91%	72%	95%	62%

TABLE 4.5: Confidence at which we detect changes in our distributions of binaries, for our simulations with primordial binaries and larger virial parameters, at the current time in the simulations.

in primary mass and semi-major axis, and an increase in eccentricity, with confidence  $\sim 70\%$ . This alone would not be enough to draw any conclusions about modifications to the primordial population, however it is reassuring to note that the opposite trend – e.g. an increase in semi-major axes – is not favoured. For V2-b, which is the simulation that has evolved for the longest after the onset of star formation (2.3 Myr), we find an increase in mass ratio and a decrease in semi-major axis with  $> 90\%$  confidence, and a decrease in primary mass with 72% confidence.

It is also possible to compare V1-b to our fiducial runs at equal stellar mass. We plot the distributions of binary properties when the formed stellar mass is  $\sim 550 M_{\odot}$  in Figure 4.8. We compare the distributions for V1-b to the spread in the fiducial simulations, and find that they generally fall within the range of values from the fiducial simulations. *The effects of dynamical interactions on the primordial population of binaries – increase in mass ratio and eccentricity, decrease in primary mass and semi-major axis – thus appear independent of the initial virial parameter of the cloud, although the observed trends are stronger when the system is more dynamically evolved.*

The next step is to investigate the effects of the random turbulent velocity pattern on the SFR, plotted in Figure 4.9. The two new sets of turbulent initial conditions are spheres with the same virial parameter, radius, density profile and temperature as our fiducial initial conditions; the turbulence follows the same power-law spectrum. The variations in total kinetic and potential energy, as well as in the sphere masses and free-fall times, are within 1%. The first star forms later in M4S3 than in the fiducial runs

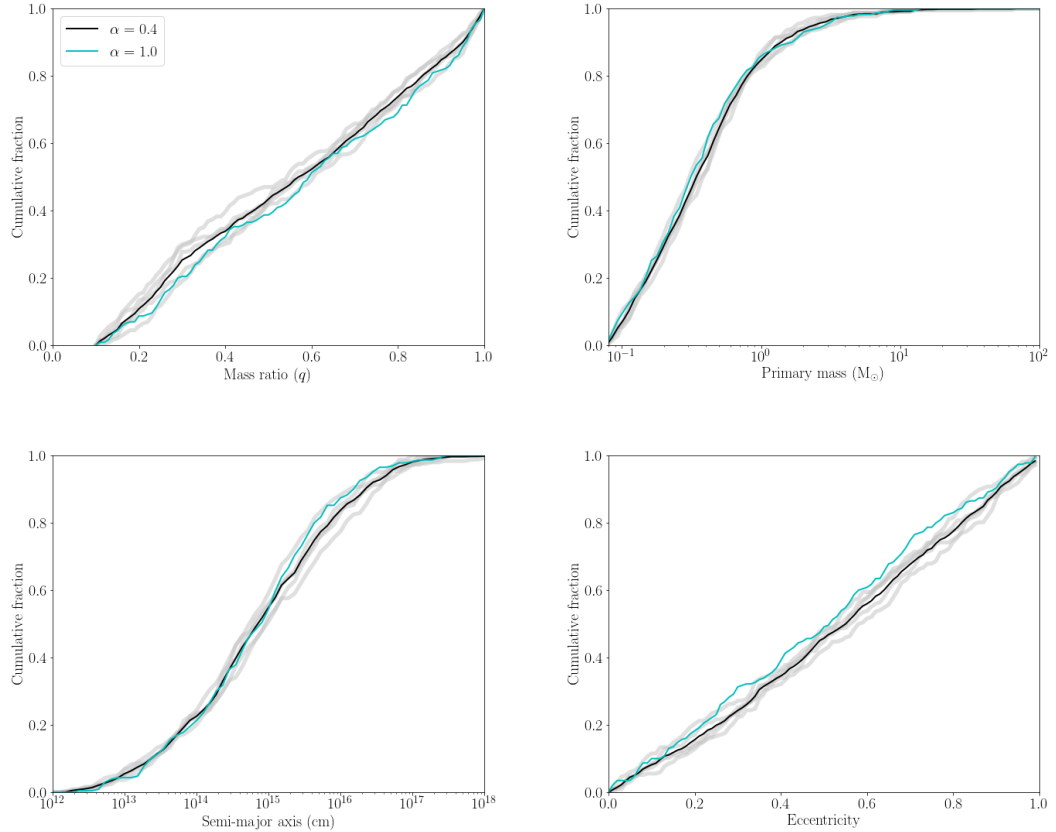


FIGURE 4.8: Cumulative distributions of mass ratios (top left), primary masses (top right), semi-major axes (bottom left) and eccentricities (top right) when the stellar mass in the simulation is  $\sim 550 M_{\odot}$ . The solid black lines denote the combined distributions for  $\alpha = 0.4$ , the grey lines denote the individual distributions for  $\alpha = 0.4$  and the cyan line denotes the distributions for  $\alpha = 1.0$

(after 1.24 Myr); it forms earlier in M4S7 (after 1.08 Myr). At equal virial parameter but different turbulent velocity pattern, there is a spread of 0.26 Myr in times for the onset of star formation; at different virial parameters but same turbulent velocity pattern, the spread is 0.25 Myr. The SFR as a function of time is also markedly different for the different random initial velocity patterns: M4S3 and M4S7 both have SFRs as high as one order of magnitude higher than the fiducial runs, 0.75–1.00 Myr after the onset of star formation. We also conduct a test with our improved refinement criteria, timestep

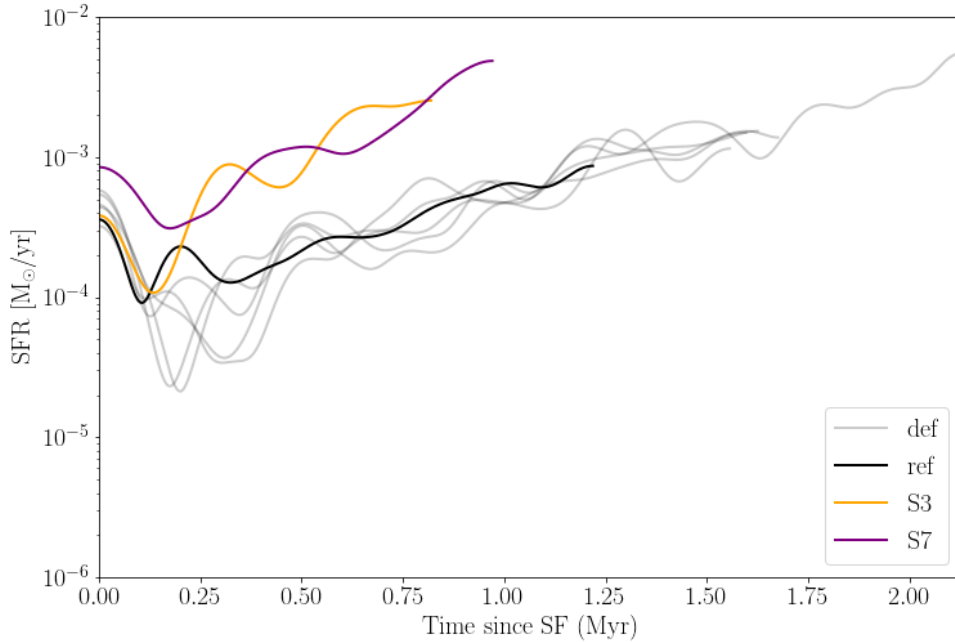


FIGURE 4.9: Star formation rate as a function of time since the onset of star formation, for three different sets of turbulent initial conditions. The grey lines are the fiducial simulations, the orange line is M4S3 and the violet line is M4S7. The black line represents a test of the fiducial initial conditions conducted with our most recent refinement criteria, also used for M4S3 and M4S7.

	Mass ratio Increase	Primary mass Decrease	Semi-major axis Decrease	Eccentricity Increase
M4S3	79%	76%	96%	88%
M3S7	82%	83%	96%	57%

TABLE 4.6: Confidence at which we detect changes in our distributions of binaries, for our simulations with primordial binaries and different turbulent initial conditions, at the current time in the simulations.

and solver (chosen for stability and speed), to verify that the discrepancy between the fiducial runs and M4S3 and M4S7 is not a product of our numerical methods. We find that this test run is consistent with the other SFRs obtained from our fiducial conditions. *This suggests that the virial parameter and the initial turbulent velocity pattern may have comparable importance in shaping star formation in a GMC.*

We can also compare the distributions of binary properties for the different turbulent initial conditions, at equal stellar mass. In Figure 4.10, we plot the cumulative distributions for M4b1, M4b3, M4b4, M4S3 and M4S7 at a stellar mass of  $\sim 880 M_{\odot}$ . We find that the distributions for M4S3 and M4S7 lie within the range of values for our fiducial simulations, despite the higher star formation rate. We also investigate how the primordial population of binaries is modified, in M4S3 and M4S7. We find the same trends as above, with confidence levels presented in Table 4.6. This would suggest that although the initial turbulent velocity pattern, like the initial virial parameter, influences the SFR, the trends for systems above the  $q \geq 0.1$  detection limit – increase in mass ratios and eccentricities, decrease in primary mass and semi-major axis – are robust to changes in the initial conditions.

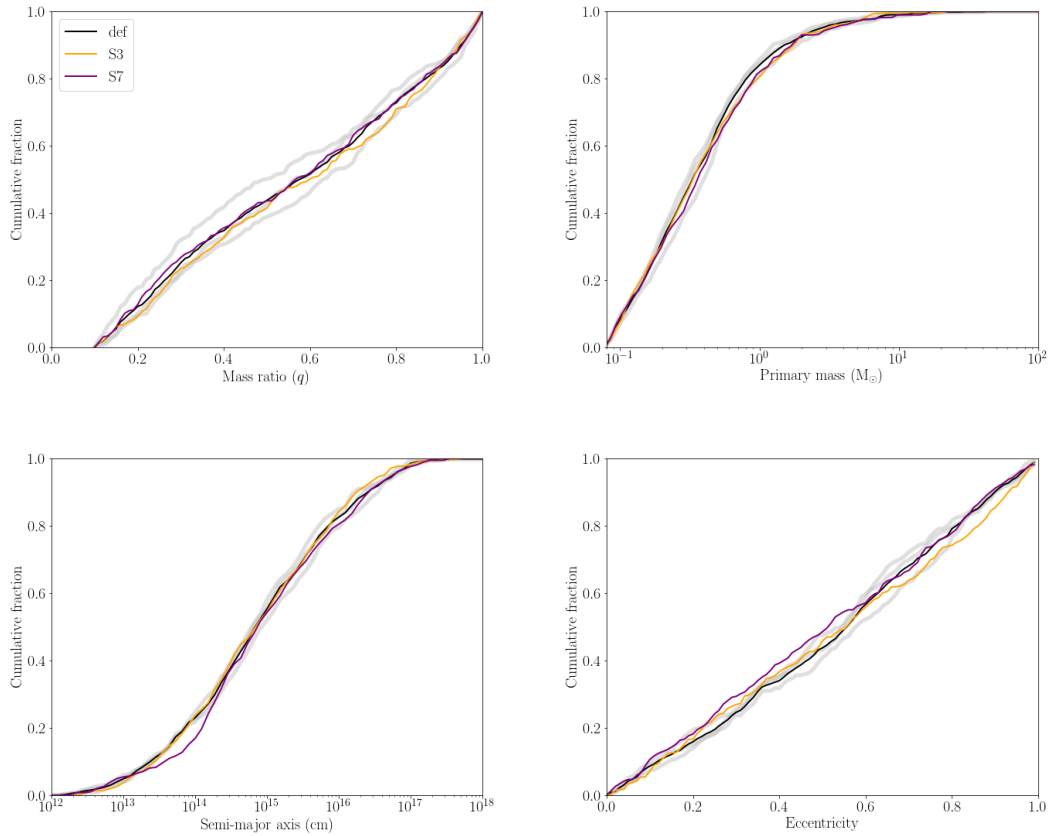


FIGURE 4.10: Cumulative distributions of mass ratios (top left), primary masses (top right), semi-major axes (bottom left) and eccentricities (bottom right) when the stellar mass in the simulation is  $\sim 880 M_{\odot}$ . The solid black lines denote the combined distributions with the fiducial initial conditions, the grey lines denote the individual distributions for the fiducial initial conditions, the orange lines denote the distributions for M4S3 and the violet lines denote the distributions for M4S7.

## 4.4 Directions for future work

The natural endpoint of multi-physics simulations of star cluster formation is gas expulsion. It is expected to happen on a timescale  $\lesssim 10$  Myr: most of the gas will be cleared out by a combination of winds and radiation, and any remaining gas will be removed by the first supernovae. The next logical step for our simulations is thus to extend them to gas expulsion. This is non-trivial numerically: feedback reduces the simulation timestep by creating zones with hot and fast gas while the increasing number of binaries drastically slows down the integration of binaries with MULTIPLES. The first issue is addressed by using a combination of more relaxed timestepping criteria and increasing stability by enforcing refinement in the regions affected by feedback. To tackle the second issue, our current plan is the migration to a new stellar dynamics code, PETAR (Wang et al. 2020a). PETAR is more efficient for systems with large numbers of particles, or systems with a few  $10^2$  binaries. It uses a Barnes-Hut tree (less computationally expensive than a pure or direct N-body code, Barnes & Hut 1986) for long-range interactions, a fourth-order Hermite scheme for short-range interactions and a slow-down algorithmic regularization scheme (SDAR, Wang et al. 2020b) for binaries and multiple systems. The SDAR scheme artificially slows down orbital motions and interactions in order to average any perturbation over many orbits; this improves numerical efficiency while conserving angular momentum due to the algorithmic regularization. Using PETAR should allow us to reach gas expulsion in our simulations in a manner of a few months, instead of years. After gas expulsion, our clusters could be compared to observations of open clusters. Following the expulsion of the gas would also allow us to compare the importance of the different feedback mechanisms we include – winds, direct radiation pressure, ionizing radiation and supernovae – which are rarely all included in a single simulation.

Another natural extension of the work we present in this thesis is to test different prescriptions for primordial binaries:

- A possible approach would be to modify our current prescription by adding an excess of the systems that are preferentially destroyed, to attempt to recover the field population after dynamical interactions.
- Another approach would be to use a prescription motivated directly by observations of embedded clusters or protostars.
- Extending the prescription to primordial systems below the detection threshold of  $q \geq 0.1$  may also be valuable, as the companions to a massive star could be reasonably massive (e.g.  $\sim 1 - 2 M_{\odot}$ ) and still be well below that detection limit. Stars with masses  $\gtrsim 8 M_{\odot}$  have, on average, as many companions with  $0.1 < q < 0.3$  as companions with  $q \geq 0.3$  (Moe & Di Stefano 2017); this suggests that they might have a significant number of companions with  $q < 0.1$ .
- The inclusion of triples and quadruples, at least for massive stars, could be important for cluster dynamics: for O-stars, binaries, triples and quadruples each account for  $\sim 30\%$  of systems.

Exploring different prescriptions for primordial binaries (and higher order systems) in our simulations and comparing the resulting clusters and multiple systems to observations may provide valuable insights on primordial multiplicity in embedded clusters.

Most massive stars are in interacting binaries (Sana et al. 2012), which influences the feedback coming from these stars: supernovae may be delayed by mass transfer, winds collide and interact, and stars stripped of their outer envelope emit more UV radiation. Binary interaction prescriptions already exist in SEBA (Portegies Zwart & Verbunt 1996), and they could be coupled to our binary dynamics code – either MULTIPLES or SDAR – within the AMUSE framework. Implementing a scheme for binary evolution in TORCH would provide a more accurate modelling of stellar feedback, which

may in turn influence star formation rates, termination of star formation and gas expulsion. The addition of pre-main sequence stellar evolution may also be relevant: it could influence the number and properties of the binaries in the cluster (see e.g. Wiersma et al. 2006).

Most globular clusters present star-to-star chemical abundance variations, with a population of stars enriched in He, N and Na, and depleted in C and O (hereafter *enriched population*, Bastian & Lardo 2018). The cause of these variations is still unknown, although numerous sources of enrichment have been proposed, including winds from asymptotic giant branch stars, supermassive stars and interacting binaries. De Mink et al. (2009) simulate an interacting binary with an orbital period of 12 days, a primary mass of  $20 M_{\odot}$  and a companion mass of  $15 M_{\odot}$ , and find that the ejected material is enriched in He, N and Na, and depleted in C and O. They propose that a combination of the ejecta from massive and intermediate mass binaries and an equal amount of pristine material leftover from star formation would allow for the formation of a second generation of stars. Howard et al. (2019) track the evolution of the He abundance (which they use as a proxy for the overall enrichment) in post-processing of their simulations of YMC assembly within GMCs, and find that cluster assembly via repeated mergers of subclusters reproduces well the spread in chemical abundance variations observed in GCs. Our simulations, which include both a large, realistic number of massive binaries and cluster assembly via merging of subclusters, are thus a natural playground to fully test the viability of interacting binaries as the source of the enriched population. The first step would be to extend De Mink et al.’s work to a larger range of primary masses, mass ratios and orbital periods. If the yields from these interactions, applied to a reasonable population of binaries, are still consistent with the expected enrichment, the next step would be to track the gas chemical abundances in our simulations, post-processing.

Other possible extensions of our work are towards larger or smaller physical scales.

More realistic initial conditions could be obtained from simulations of galaxy formation; zoom-in simulations of binary systems at higher spatial resolution for the gas would allow us to model the effects of gas dynamical friction (e.g. Stahler 2010). On the analysis side, future avenues for investigation could include detailed investigations of binary exchanges, and tracking the dynamical formation of higher order multiples in our simulations. The work presented in this thesis, in showing that dynamical interactions within embedded clusters modify the primordial populations of binaries, opens the floor to more investigations of the impact of binaries on star cluster formation.

---

## BIBLIOGRAPHY

- Abt, H. A. & Levy, S. G. 1976. *ApJS* 30, 273–306.
- Baczynski, C., Glover, S. C. O., & Klessen, R. S. 2015. *MNRAS* 454, 380–411.
- Ballesteros-Paredes, J., Klessen, R. S., Mac Low, M. -M., & Vazquez-Semadeni, E. 2007.  
In: *Protostars and Planets V*. Ed. by B. Reipurth, D. Jewitt, & K. Keil, 63.
- Ballone, A., Torniamenti, S., Mapelli, M., Di Carlo, U. N., Spera, M., Rastello, S.,  
Gaspari, N., & Iorio, G. 2021. *MNRAS* 501, 2920–2933.
- Barnes, J. & Hut, P. 1986. *Nature* 324, 446–449.
- Bastian, N. & Lardo, C. 2018. *ARA&A* 56, 83–136.
- Bate, M. R., Bonnell, I. A., & Price, N. M. 1995. *MNRAS* 277, 362–376.
- Bertoldi, F. & McKee, C. F. 1992. *ApJ* 395, 140.
- Bodenheimer, P., Laughlin, G. P., Rozyczka, M., & Yorke, H. W. 2006. *Numerical Methods in Astrophysics: An Introduction*. 1st. CRC Press.
- Boss, A. P. & Bodenheimer, P. 1979. *ApJ* 234, 289–295.
- Chabrier, G. 2003. *PASP* 115, 763–795.
- Chen, Y., Li, H., & Vogelsberger, M. 2021. *MNRAS* 502, 6157–6169.

## Bibliography

---

- Chevance, M., Kruijssen, J. M. D., Vazquez-Semadeni, E., Nakamura, F., Klessen, R., Ballesteros-Paredes, J., Inutsuka, S.-i., Adamo, A., & Hennebelle, P. 2020. *Space Sci. Rev.* 216 50, 50.
- Chini, R., Hoffmeister, V. H., Nasser, A., Stahl, O., & Zinnecker, H. 2012. *MNRAS* 424, 1925–1929.
- Colella, P. & Woodward, P. R. 1984. *J. Comput. Phys.* 54, 174–201.
- Crain, R. A. et al. 2015. *MNRAS* 450, 1937–1961.
- Dale, J. E., Ercolano, B., & Bonnell, I. A. 2012. *MNRAS* 424, 377–392.
- Dale, J. E., Ercolano, B., & Bonnell, I. A. 2013. *MNRAS* 431, 1062–1076.
- Dale, J. E., Ngoumou, J., Ercolano, B., & Bonnell, I. A. 2014. *MNRAS* 442, 694–712.
- Deacon, N. R. & Kraus, A. L. 2020. *MNRAS* 496, 5176–5200.
- Delfosse, X., Beuzit, J. -L., Marchal, L., Bonfils, X., Perrier, C., Ségransan, D., Udry, S., Mayor, M., & Forveille, T. 2004. In: *Spectroscopically and Spatially Resolving the Components of the Close Binary Stars*. Ed. by R. W. Hilditch, H. Hensberge, & K. Pavlovski. Vol. 318. ASP Conf. Ser. San Francisco: Astronomical Society of the Pacific, 166–174.
- Dobbs, C. L., Krumholz, M. R., Ballesteros-Paredes, J., Bolatto, A. D., Fukui, Y., Heyer, M., Low, M. -M. M., Ostriker, E. C., & Vázquez-Semadeni, E. 2014. In: *Protostars and Planets VI*. Ed. by H. Beuther, R. S. Klessen, C. P. Dullemond, & T. Henning, 3.
- Duchêne, G., Bouvier, J., Simon, T., Close, L., & Eislöffel, J. 1999. In: *Astronomy with adaptive optics : present results and future programs*. Ed. by D. Bonaccini. Vol. 56. ESO Conference and Workshop Proceedings. Garching: European Southern Observatory, 185.
- Duchêne, G., Lacour, S., Moraux, E., Goodwin, S., & Bouvier, J. 2018. *MNRAS* 478, 1825–1836.
- Duchêne, G. & Kraus, A. 2013. *ARA&A* 51, 269–310.
- Duquennoy, A. & Mayor, M. 1991. *A&A* 500, 337–376.

## Bibliography

---

- Federrath, C. 2015. *MNRAS* 450, 4035–4042.
- Federrath, C., Banerjee, R., Clark, P. C., & Klessen, R. S. 2010. *ApJ* 713, 269–290.
- Federrath, C., Klessen, R. S., Iapichino, L., & Beattie, J. R. 2021. *Nature Astronomy* 5, 365–371.
- Fischer, D. A. & Marcy, G. W. 1992. *ApJ* 396, 178.
- Fryxell, B., Olson, K., Ricker, P., Timmes, F. X., Zingale, M., Lamb, D. Q., MacNeice, P., Rosner, R., Truran, J. W., & Tufo, H. 2000. *ApJS* 131, 273–334.
- Fujii, M., Iwasawa, M., Funato, Y., & Makino, J. 2007. *PASJ* 59, 1095.
- Fukui, Y. & Kawamura, A. 2010. *ARA&A* 48, 547–580.
- Gavagnin, E., Bleuler, A., Rosdahl, J., & Teyssier, R. 2017. *MNRAS* 472, 4155–4172.
- Gayley, K. G., Owocki, S. P., & Cranmer, S. R. 1997. *ApJ* 475, 786–797.
- Geen, S., Hennebelle, P., Tremblin, P., & Rosdahl, J. 2016. *MNRAS* 463, 3129–3142.
- Gehrels, N. 1986. *ApJ* 303, 336.
- Gieles, M., Sana, H., & Portegies Zwart, S. F. 2010. *MNRAS* 402, 1750–1757.
- Glatt, K., Grebel, E. K., & Koch, A. 2010. *A&A* 517 A50, A50.
- Gorti, U. & Bhatt, H. C. 1996. *MNRAS* 283, 566–576.
- Götberg, Y., de Mink, S. E., Groh, J. H., Kupfer, T., Crowther, P. A., Zapartas, E., & Renzo, M. 2018. *A&A* 615 A78, A78.
- Grand, R. J. J., Gómez, F. A., Marinacci, F., Pakmor, R., Springel, V., Campbell, D. J. R., Frenk, C. S., Jenkins, A., & White, S. D. M. 2017. *MNRAS* 467, 179–207.
- Grellmann, R., Preibisch, T., Ratzka, T., Kraus, S., Helminiak, K. G., & Zinnecker, H. 2013. *A&A* 550 A82, A82.
- Gritschneider, M., Naab, T., Walch, S., Burkert, A., & Heitsch, F. 2009. *ApJ* 694, L26–L30.
- Grudić, M. Y., Guszejnov, D., Hopkins, P. F., Lamberts, A., Boylan-Kolchin, M., Murray, N., & Schmitz, D. 2018. *MNRAS* 481, 688–702.

## Bibliography

---

- Grudić, M. Y., Guszejnov, D., Hopkins, P. F., Offner, S. S. R., & Faucher-Giguère, C.-A. 2021. *MNRAS*.
- Guszejnov, D., Grudić, M. Y., Hopkins, P. F., Offner, S. S. R., & Faucher-Giguère, C.-A. 2020. *MNRAS* 496, 5072–5088.
- Guszejnov, D., Grudić, M. Y., Hopkins, P. F., Offner, S. S. R., & Faucher-Giguère, C.-A. 2021. *MNRAS* 502, 3646–3663.
- Guszejnov, D., Hopkins, P. F., & Krumholz, M. R. 2017. *MNRAS* 468, 4093–4106.
- Haid, S., Walch, S., Seifried, D., Wunsch, R., Dinnbier, F., & Naab, T. 2018. *MNRAS* 478, 4799–4815.
- Haugbølle, T., Padoan, P., & Nordlund, Å. 2018. *ApJ* 854 35, 35.
- Heggie, D. C. 1975. *MNRAS* 173, 729–787.
- Heggie, D. C. & Rasio, F. A. 1996. *MNRAS* 282, 1064–1084.
- Hénault-Brunet, V. et al. 2012. *A&A* 546 A73, A73.
- Heyer, M. & Dame, T. M. 2015. *ARA&A* 53, 583–629.
- Hillenbrand, L. A. & Hartmann, L. W. 1998. *ApJ* 492, 540–553.
- Hills, J. G. 1975. *AJ* 80, 809–825.
- Hopkins, P. F., Kereš, D., Oñorbe, J., Faucher-Giguère, C.-A., Quataert, E., Murray, N., & Bullock, J. S. 2014. *MNRAS* 445, 581–603.
- Howard, C. S., Pudritz, R. E., & Harris, W. E. 2016. *MNRAS* 461, 2953–2974.
- Howard, C. S., Pudritz, R. E., & Harris, W. E. 2017. *MNRAS* 470, 3346–3358.
- Howard, C. S., Pudritz, R. E., & Harris, W. E. 2018. *Nature Astronomy* 2, 725–730.
- Howard, C. S., Pudritz, R. E., Sills, A., & Harris, W. E. 2019. *MNRAS* 486, 1146–1155.
- Hoyle, F. 1953. *ApJ* 118, 513.
- Hughes, I. G. & Hase, T. P. 2010. *Measurements and their Uncertainties*. Oxford: Oxford University Press.
- Hugoniot, H. 1885. *Comptes Rendus des Séances de l'Académie des Sciences, Paris* 101, 794–796.

## Bibliography

---

- Hut, P., Makino, J., & McMillan, S. 1995. *ApJ* 443, L93.
- Hut, P., McMillan, S., Makino, J., & Portegies Zwart, S. 2010. *Starlab: A Software Environment for Collisional Stellar Dynamics*.
- Ivanova, N., Heinke, C. O., Rasio, F. A., Taam, R. E., Belczynski, K., & Fregeau, J. 2006. *MNRAS* 372, 1043–1059.
- De Jager, C., Nieuwenhuijzen, H., & van der Hucht, K. A. 1988. *A&AS* 72, 259–289.
- Jeans, J. H. 1928. *Astronomy and Cosmogony*. 1st. Cambridge: Cambridge University Press.
- Jeans, J. H. 1902. *Philosophical Transactions of the Royal Society of London Series A* 199, 1–53.
- King, R. R., Goodwin, S. P., Parker, R. J., & Patience, J. 2012. *MNRAS* 427, 2636–2646.
- Kobulnicky, H. A. et al. 2014. *ApJS* 213 34, 34.
- Körtgen, B., Seifried, D., Banerjee, R., Vázquez-Semadeni, E., & Zamora-Avilés, M. 2016. *MNRAS* 459, 3460–3474.
- Kouwenhoven, M. B. N., Brown, A. G. A., Goodwin, S. P., Portegies Zwart, S. F., & Kaper, L. 2009. *A&A* 493, 979–1016.
- Kouwenhoven, M. B. N., Brown, A. G. A., Zinnecker, H., Kaper, L., & Portegies Zwart, S. F. 2005. *A&A* 430, 137–154.
- Kouwenhoven, M. B. N., Goodwin, S. P., Parker, R. J., Davies, M. B., Malmberg, D., & Kroupa, P. 2010. *MNRAS* 404, 1835–1848.
- Kratter, K. M. 2011. In: *Evolution of Compact Binaries*. Ed. by L. Schmidtbreich, M. R. Schreiber, & C. Tappert. Vol. 447. Astronomical Society of the Pacific Conference Series, 47.
- Krause, M. G. H. et al. 2020. *Space Sci. Rev.* 216 64, 64.
- Kroupa, P. 1995. *MNRAS* 277, 1522.
- Kroupa, P. 2001. *MNRAS* 322, 231–246.
- Kruijssen, J. M. D. 2012. *MNRAS* 426, 3008–3040.

## Bibliography

---

- Kruijssen, J. M. D. 2015. *MNRAS* 454, 1658–1686.
- Kruijssen, J. M. D., Pelupessy, F. I., Lamers, H. J. G. L. M., Portegies Zwart, S. F., & Icke, V. 2011. *MNRAS* 414, 1339–1364.
- Krumholz, M. R. & Matzner, C. D. 2009. *ApJ* 703, 1352–1362.
- Krumholz, M. R., McKee, C. F., & Bland-Hawthorn, J. 2019. *ARA&A* 57, 227–303.
- Krumholz, M. R., McKee, C. F., & Klein, R. I. 2004. *ApJ* 611, 399–412.
- Lada, C. J. & Lada, E. A. 2003. *ARA&A* 41, 57–115.
- Lancaster, L., Ostriker, E. C., Kim, J.-G., & Kim, C.-G. 2021a. *ApJ* 914 89, 89.
- Lancaster, L., Ostriker, E. C., Kim, J.-G., & Kim, C.-G. 2021b. *ApJ* 914 90, 90.
- Larson, R. B. 1981. *MNRAS* 194, 809–826.
- Lee, D. 2013. *J. Comput. Phys.* 243, 269–292.
- Lee, E. J., Miville-Deschênes, M.-A., & Murray, N. W. 2016a. *ApJ* 833 229, 229.
- Lee, J.-E., Lee, S., Dunham, M. M., Tatematsu, K., Choi, M., Bergin, E. A., & Evans, N. J. 2017. *Nature Astronomy* 1 0172, 0172.
- Lee, K. I. et al. 2016b. *ApJ* 820 L2, L2.
- Leigh, N., Giersz, M., Webb, J. J., Hypki, A., De Marchi, G., Kroupa, P., & Sills, A. 2013. *MNRAS* 436, 3399–3412.
- Li, H., Vogelsberger, M., Marinacci, F., & Gnedin, O. Y. 2019. *MNRAS* 487, 364–380.
- Lohner, R. 1987. *Comput. Methods Appl. Mech. Eng.* 61, 323–338.
- MacNeice, P., Olson, K. M., Mobarrry, C., de Fainchtein, R., & Packer, C. 2000. *Comput. Phys. Commun.* 126, 330–354.
- Macquorn Rankine, W. J. 1870. *Philosophical Transactions of the Royal Society of London Series I* 160, 277–288.
- Makino, J. & Aarseth, S. J. 1992. *PASJ* 44, 141–151.
- Mann, H. B. & Whitney, D. R. 1947. *Annals of Mathematical Statistics* 18, 50–60.
- Mardling, R. A. 2008. In: *Proceedings IAU Symposium No. 246*. Ed. by E. Vesperini, M. Giersz, & A. Sills. Cambridge: Cambridge University Press, 199–208.

## Bibliography

---

- Matzner, C. D. & Jumper, P. H. 2015. *ApJ* 815 68, 68.
- Matzner, C. D. & McKee, C. F. 2000. *ApJ* 545, 364–378.
- McMillan, S., Portegies Zwart, S., van Elteren, A., & Whitehead, A. 2012. In: *Advances in Computational Astrophysics: Methods, Tools, and Outcome*. Ed. by R. Capuzzo-Dolcetta, M. Limongi, & A. Tornambè. Vol. 453. ASP Conf. Ser. San Francisco, 129.
- McMillan, S. L. W. & Hut, P. 1996. *ApJ* 467, 348.
- Miholics, M., Kruijssen, J. M. D., & Sills, A. 2017. *MNRAS* 470, 1421–1435.
- Milone, A. P., Marino, A. F., Bedin, L. R., Dotter, A., Jerjen, H., Kim, D., Nardiello, D., Piotto, G., & Cong, J. 2016. *MNRAS* 455, 3009–3019.
- De Mink, S. E., Pols, O. R., Langer, N., & Izzard, R. G. 2009. *A&A* 507, L1–L4.
- Miyoshi, T. & Kusano, K. 2005. *J. Comput. Phys.* 208, 315–344.
- Moe, M. & Di Stefano, R. 2015. *ApJ* 810 61, 61.
- Moe, M. & Di Stefano, R. 2017. *ApJS* 230 15, 15.
- Murray, N., Quataert, E., & Thompson, T. A. 2010. *ApJ* 709, 191–209.
- Von Neumann, J. & Richtmyer, R. D. 1950. *Journal of Applied Physics* 21, 232–237.
- Von Neumann, J. 1951. Various Techniques Used in Connection with Random Digits. In: *Monte Carlo Method*. Ed. by A. S. Householder, G. E. Forsythe, & H. H. Germond. Vol. 12. National Bureau of Standards Applied Mathematics Series. Washington, DC: US Government Printing Office. Chap. 13, 36–38.
- Offner, S. S. R. & Chaban, J. 2017. *ApJ* 847 104, 104.
- Offner, S. S. R., Kratter, K. M., Matzner, C. D., Krumholz, M. R., & Klein, R. I. 2010. *ApJ* 725, 1485–1494.
- Padoan, P., Federrath, C., Chabrier, G., Evans N. J., I., Johnstone, D., Jørgensen, J. K., McKee, C. F., & Nordlund, Å. 2014. In: *Protostars and Planets VI*. Ed. by H. Beuther, R. S. Klessen, C. P. Dullemond, & T. Henning, 77.
- Parker, R. J. & Goodwin, S. P. 2012. *MNRAS* 424, 272–281.

## Bibliography

---

- Parker, R. J., Goodwin, S. P., Kroupa, P., & Kouwenhoven, M. B. N. 2009. *MNRAS* 397, 1577–1586.
- Parker, R. J. & Meyer, M. R. 2014. *MNRAS* 442, 3722–3736.
- Parker, R. J. & Reggiani, M. M. 2013. *MNRAS* 432, 2378–2384.
- Pelupessy, F. I. & Portegies Zwart, S. 2012. *MNRAS* 420, 1503–1517.
- Plunkett, A. L., Arce, H. G., Corder, S. A., Dunham, M. M., Garay, G., & Mardones, D. 2015. *ApJ* 803 22, 22.
- Portegies Zwart, S. & McMillan, S. L. W. 2019. *Astrophysical Recipes: The Art of Amuse*. Bristol: Institute of Physics Publishing.
- Portegies Zwart, S. F., Makino, J., McMillan, S. L. W., & Hut, P. 1999. *A&A* 348, 117–126.
- Portegies Zwart, S. F. & Verbunt, F. 1996. *A&A* 309, 179–196.
- Portegies Zwart, S. F., McMillan, S. L. W., & Gieles, M. 2010. *ARA&A* 48, 431–493.
- Portegies Zwart, S. F., McMillan, S. L. W., Hut, P., & Makino, J. 2001. *MNRAS* 321, 199–226.
- Press, W. H., Teukolsky, S. A., Vetterling, W. T., & Flannery, B. P. 2007. *Numerical Recipes: The Art of Scientific Computing*. 3rd. Cambridge: Cambridge University Press.
- Price, D. J. & Bate, M. R. 2008. *MNRAS* 385, 1820–1834.
- Price-Whelan, A. M., Hogg, D. W., Rix, H.-W., Beaton, R. L., Lewis, H. M., Nidever, D. L., Almeida, A., Badenes, C., Barba, R., & Beers, T. C. 2020. *ApJ* 895, 2.
- Raghavan, D., McAlister, H. A., Henry, T. J., Latham, D. W., Marcy, G. W., Mason, B. D., Gies, D. R., White, R. J., & Ten Brummelaar, T. A. 2010. *ApJS* 190, 1–42.
- Rastello, S., Carraro, G., & Capuzzo-Dolcetta, R. 2020. *ApJ* 896 152, 152.
- Reid, I. N. & Gizis, J. E. 1997. *AJ* 113, 2246.
- Reipurth, B., Clarke, C. J., Boss, A. P., Goodwin, S. P., Rodríguez, L. F., Stassun, K. G., Tokovinin, A., & Zinnecker, H. 2014. Multiplicity in Early Stellar Evolution.

## Bibliography

---

- In: *Protostars and Planets VI*. Ed. by H. Beuther & et al. Tucson: University of Arizona, 267–290.
- Reipurth, B., Guimarães, M. M., Connelley, M. S., & Bally, J. 2007. *AJ* 134, 2272–2285.
- Ricker, P. M. 2008. *ApJS* 176, 293–300.
- Rogers, H. & Pittard, J. M. 2013. *MNRAS* 431, 1337–1351.
- De Rosa, R. J. et al. 2014. *MNRAS* 437, 1216–1240.
- Rybicki, G. B. & Lightman, A. P. 2004. *Radiative Processes in Astrophysics*. 2nd. Weinheim: Wiley-VCH.
- Sana, H., De Mink, S. E., De Koter, A., Langer, N., Evans, C. J., Gieles, M., Gosset, E., Izzard, R. G., Le Bouquin, J. -B., & Schneider, F. R. N. 2012. *Science* 337, 444.
- Sana, H. & Evans, C. J. 2011. In: *Active OB Stars: Structure, Evolution, Mass Loss, and Critical Limits*. Ed. by C. Neiner, G. Wade, G. Meynet, & G. Peters. Vol. 272. IAU Symposium. Cambridge: Cambridge University Press, 474–485.
- Schaye, J. et al. 2015. *MNRAS* 446, 521–554.
- Schruba, A., Kruijssen, J. M. D., & Leroy, A. K. 2019. *ApJ* 883 2, 2.
- Sigalotti, L. D. G., Cruz, F., Gabbasov, R., Klapp, J., & Ramirez-Velasquez, J. 2018. *ApJ* 857 40, 40.
- Sigurdsson, S. & Phinney, E. S. 1993. *ApJ* 415, 631.
- Sills, A. & Baily, C. D. 1999. *ApJ* 513, 428–441.
- Sills, A., Rieder, S., Scora, J., McCloskey, J., & Jaffa, S. 2018. *MNRAS* 477, 1903–1912.
- Smith, N. 2014. *ARA&A* 52, 487–528.
- Sollima, A. 2008. *MNRAS* 388, 307–322.
- Sormani, M. C., Treß, R. G., Klessen, R. S., & Glover, S. C. O. 2017. *MNRAS* 466, 407–412.
- Stahler, S. W. 2010. *MNRAS* 402, 1758–1766.
- Stevens, I. R. & Pollock, A. M. T. 1994. *MNRAS* 269, 226–234.
- Sun, J. et al. 2018. *ApJ* 860 172, 172.

## Bibliography

---

- Takahashi, S. Z., Tsukamoto, Y., & Inutsuka, S. 2016. *MNRAS* 458, 3597–3612.
- Tobin, J. J. et al. 2016a. *Nature* 538, 483–486.
- Tobin, J. J. et al. 2016b. *ApJ* 818 73, 73.
- Tokovinin, A. 2017. *MNRAS* 468, 3461–3467.
- Tokovinin, A. & Moe, M. 2020. *MNRAS* 491, 5158–5171.
- Toomre, A. 1964. *ApJ* 139, 1217–1238.
- Torniamenti, S., Ballone, A., Mapelli, M., Gaspari, N., Di Carlo, U. N., Rastello, S., Giacobbo, N., & Pasquato, M. 2021. *arXiv e-prints* arXiv:2104.12781, arXiv:2104.12781.
- Toro, E. F., Spruce, M., & Speares, W. 1994. *Shock Waves* 4, 25–34.
- Toro, E. F. 2009. *Riemann Solvers and Numerical Methods for Fluid Dynamics: A Practical Introduction*. 3rd. Berlin: Springer.
- Truelove, J. K., Klein, R. I., McKee, C. F., Holliman John H., I., Howell, L. H., & Greenough, J. A. 1997. *ApJ* 489, L179–L183.
- Vázquez-Semadeni, E., González-Samaniego, A., & Colín, P. 2017. *MNRAS* 467, 1313–1328.
- Vink, J. S., de Koter, A., & Lamers, H. J. G. L. M. 2000. *A&A* 362, 295–309.
- Wall, J. E., Mac Low, M.-M., McMillan, S. L. W., Klessen, R. S., Portegies Zwart, S., & Pellegrino, A. 2020. *ApJ*.
- Wall, J. E., McMillan, S. L. W., Mac Low, M.-M., Klessen, R. S., & Portegies Zwart, S. 2019. *ApJ* 887 62, 62.
- Wang, L., Iwasawa, M., Nitadori, K., & Makino, J. 2020a. *MNRAS* 497, 536–555.
- Wang, L., Nitadori, K., & Makino, J. 2020b. *MNRAS* 493, 3398–3411.
- Weaver, R., McCray, R., Castor, J., Shapiro, P., & Moore, R. 1977. *ApJ* 218, 377–395.
- Wiersma, R., Sills, A., & Portegies Zwart, S. 2006. *ApJ* 637, 838–849.
- Wilcoxon, F. 1945. *Biometrics Bulletin* 1, 80–83.
- Winters, J. G., Henry, T. J., Jao, W.-C., Subasavage, J. P., Chatelain, J. P., Slatten, K., Riedel, A. R., Silverstein, M. L., & Payne, M. J. 2019. *AJ* 157 216, 216.